Universita' degli Studi della Calabria

Dipartimento di Fisica

Tesi di Dottorato di Ricerca in Fisica
XXI ciclo

FIS/03

Electronic and morphological properties of nanometric systems

Supervisore
Prof. Antonino Oliva

Candidato
Marina Minniti

Coordinatore del corso di Dottorato
Prof. Giovanni Falcone

Anno Accademico 2008/2009

Dedicato a chi non si e' mai tirato indietro,
a chi non si e' mai dimenticato di me e a chi
non mi ha mai lasciato sola : i miei genitori

Index

Chapter 4 – Ripple and dot pattern formation on Ge surfaces

Chapter 5 – Helium atom diffraction from solid surfaces

Chapter 6 – A single graphene layer grown on Ru(0001)

Introduction

The work presented in this thesis is a study of nanometric systems by the use of different analysis techniques. Nowadays in many fields, from physics to biology as well as in chemistry and medicine, research has been focused on such a nanostructures and the analysis techniques are also developing in this sense.

This Ph.D. work has been developed in three parts, all having nanostructures as background. The first one regards a study of carbon nanotubes by means of X-ray photoelectron spectroscopy (XPS) and electron energy loss spectroscopy (EELS). It has been done at the University of Calabria, in the Department of Physics (laboratory IIS).

The second part is related to the dynamics of ripple and dot pattern formation on Ge surfaces under noble gas ion sputtering. Sputtered samples' morphologies have been investigated by atomic force microscopy (AFM). This work has been done in Dresden, at the Institute of Ion Beam Physics and Materials Research (Forschungszentrum Dresden-Rossendorf).

The third part is about a study of graphene grown on Ru(0001) by means of Helium atom scattering (HAS), done in Madrid at the University Autonoma, in the Department of Condensed Matter (laboratory LASUAM).

The thesis is divided into 6 chapters. In Chapter 1 an introduction about carbon nanotubes and their electronic and morphological properties is given. The focus is pointed on the possibility to tailor CNTs' electronic properties by incorporation of dopants. The best candidates for this aim are nitrogen and boron atoms since they have comparable atomic size and would fit into the carbon network without altering it. Theoretical predictions about using ion implantation as a tool to dope CNTs with nitrogen atoms are presented. In Chapter 2 theoretical predictions are compared to experimental results for 300 eV N_2^+ ions implanted in single walled carbon nanotubes. XPS data allow to determine the nitrogen concentration in carbon nanotubes and to get information about the nitrogen chemical bonding nature. By means of EELS the level of damage induced by ion sputtering during implantation can be checked.

In Chapter 3, after reviewing the basic principles of the theory of sputtering, a detailed description of the continuum models which account for ripple and dot pattern formation on surfaces under ion erosion is given. Among them, only one (the GCC model) is currently able to predict the appearance of some of the non-linear effects experimentally observed. In particular, the increase of the ripple wavelength in time is known as 'coarsening'. This non-linear effect has been observed many times in experiments but its origin has not been well understood yet. In Chapter 4 a

comparison between predictions of the GCC model and coarsening observed in experiments of Xe^+ ion sputtering of Ge(100) is reported.

Chapter 5 is a short introduction to the Helium Atom Scattering and the advantages of using such a technique in studying single crystalline solid surfaces. Indeed, because of the low energies used (between 10 and 300 meV) the incident atoms are able to probe the topmost layer of the substrate surface in an absolutely nondestructive manner. HAS has been used to study properties of a graphene overlayer grown on the Ru(0001) surface. In particular, from diffraction intensities it was possible to derive information about the geometrical corrugation of the graphene layer, which is currently still under discussion. According to DFT calculations graphene grown on Ru(0001) is highly corrugated; values higher than 1 Å are reported. Diffraction spectra and relative analysis of the corrugation amplitude are presented in Chapter 6. Finally, preliminarly results about He, Ne and Ar diffraction from Ru(0001) are shown. They confirm theoretical predictions about the Ru(0001) surface. This is an ideal system to investigate how different surface electron densities can be probed at different classical turning points by changing the scattering projectile.

Chapter 1

Doping of Carbon Nanotubes

1. About carbon nanotubes

Since their discovery in the early 1990s, carbon nanotubes (CNTs) have attracted a huge interest in the scientific community due to their incredible electronic and mechanical properties [1]. The geometric shape of a single-walled carbon nanotube (SWCNT) can be understood considering a graphene sheet which is rolled up into a cylindrical shape. Their diameters can vary from 0.7 to 10.0 nm; usually most of them show a diameter of about 2 nm or less. The length of such objects can reach up to several μm or even mm. For this reason carbon nanotubes are considered a good example of one dimensional systems. The terminations of the tubes are called ‘caps’ and are essentially hemispheres of a fullerene. Each cap is made up of six pentagons and a certain number of hexagons which allow the cap to fit perfectly to the cylindrical body. An important classification regarding the simmetry of carbon nanotubes distinguishes them according to their chirality. An achiral carbon nanotube is defined as a nanotube whose mirror image has an identical structure to the original one. There are only two classes: armchair and zigzag nanotubes, which are shown in fig.1. As it emerges from the pictures, these names come from the shape of the cross-sectional ring

at the edge of the nanotubes. On the contrary chiral nanotubes have a mirror image which can not be superposed on to the original one.

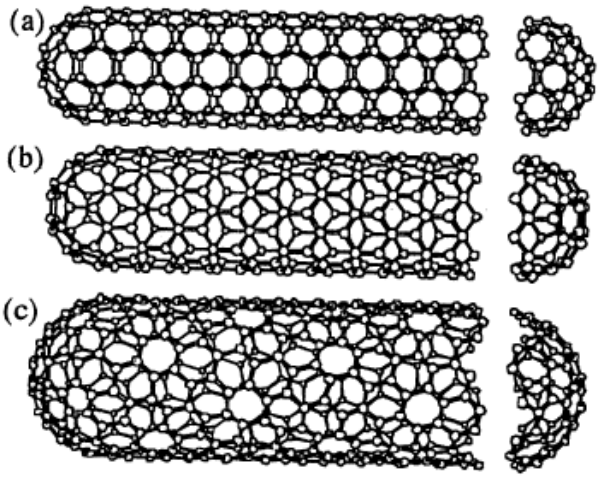

Fig.1 Classification of carbon nanotubes: (a) armchair, (b) zigzag, (c) chiral nanotubes.

The simmetry of carbon nanotubes is basically defined by two vectors in the plane of the unrolled graphene sheet. They are called 'translation vector' **T** and 'chiral vector' $\mathbf{C_h}$. The translation vector is parallel to the nanotube axis and is perpendicular to the chiral vector, which defines the section of the nanotube (see fig.2). Both vectors can be expressed in terms of the real space unit vectors $\mathbf{a_1}$ and $\mathbf{a_2}$ of the hexagonal lattice as follows:

$\mathbf{C_h} = n\mathbf{a_1} + m\mathbf{a_2}$ (n,m are integers, $0 \leq |m| \leq n$) $\quad \mathbf{T} = t_1\mathbf{a_1} + t_2\mathbf{a_2}$ (t_1 and t_2 are integers)

An armchair nanotube will always correspond to the case $n = m$, with $\mathbf{C_h} = (n,n)$, and a zigzag nanotube to $m = 0$ and $\mathbf{C_h} = (n,0)$. All other (n,m) vectors correspond to chiral nanotubes. In fig.2 four crystallographically equivalent sites O, A, B, B' are indicated. The vectors **OA** and **OB** in the plane are the chiral vector $\mathbf{C_h}$ and the translation vector **T** of the nanotube. The tube is formed when the honeycomb sheet is rolled so that point O coincides with point A and B with B'. The diameter of the carbon nanotube d is given by L/π, where L is the circumferential length of the tube:

$$d = L/\pi, \quad L = |\mathbf{C_h}| = a\sqrt{n^2 + m^2 + nm}$$

As it can be seen from the picture the vectors $\mathbf{a_1}$ and $\mathbf{a_2}$ are not orthogonal to each other, so their inner product gives:

$$\mathbf{a_1} \cdot \mathbf{a_1} = \mathbf{a_2} \cdot \mathbf{a_2} = a^2, \quad \mathbf{a_1} \cdot \mathbf{a_2} = a^2/2$$

where the lattice constant a is equal to 0.144nm x $\sqrt{3}$ = 0.249nm.

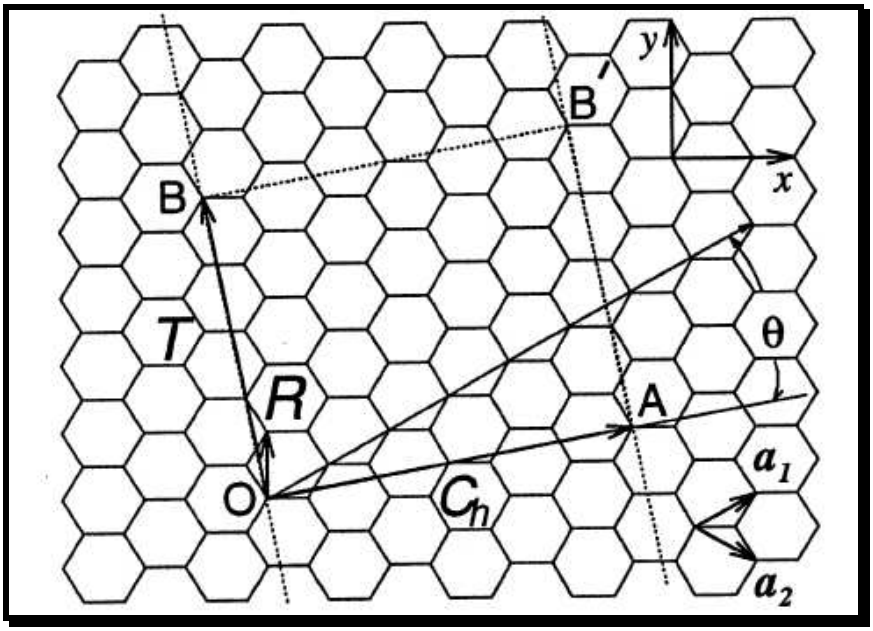

Fig.2 The unrolled honeycomb lattice of a nanotube.

The chiral angle ϑ is the angle between the vectors $\mathbf{C_h}$ and $\mathbf{a_1}$, with absolute value varing from 0° to 30° due to the hexagonal symmetry of the honeycomb lattice. The chiral angle indicates the orientation angle of the hexagons with respect to the direction of the nanotube axis and is defined as:

$$\cos\vartheta = \frac{2n+m}{2\sqrt{n^2+m^2+nm}}$$

Very interesting in carbon nanotubes is their electronic structure. Calculations demonstrate that a carbon nanotube can be either metallic or semiconducting depending on the values of (*n*,*m*) and therefore on its diameter and chirality. In a graphene sheet, the conduction and valence bands touch each other at the six corner points of the first Brillouin zone. These states are filled with electrons with Fermi's energy. For this reason a graphene sheet is semimetallic with a zero band gap. In a nanotube (assumed to be infinitely long) the electronic states are parallel lines in the k-space, continuous along the tube axis and descrete along the circumference. Looking at fig.3 it is possible to distinguish different cases [2]. For armchair tubes there are always states crossing the corner points of the first Brillouin zone (fig.3a) : they are all metallic. In case of $n - m \neq 3$ x integer the lines which represent the electronic states do not cross the corner points (fig.3c and d) : the tubes are semiconducting. The energy gap is proportional to the inverse of the diameter and is about 0.5

eV for SWCNTs with diameter of 1.4 nm. In fig.3b (which represents the case $n - m = 3$ x integer) some electronic states cross the hexagon corners : the carbon nanotubes should be semimetals but they become small gap semiconductors due to a curvature induced orbital rehybridization effect.

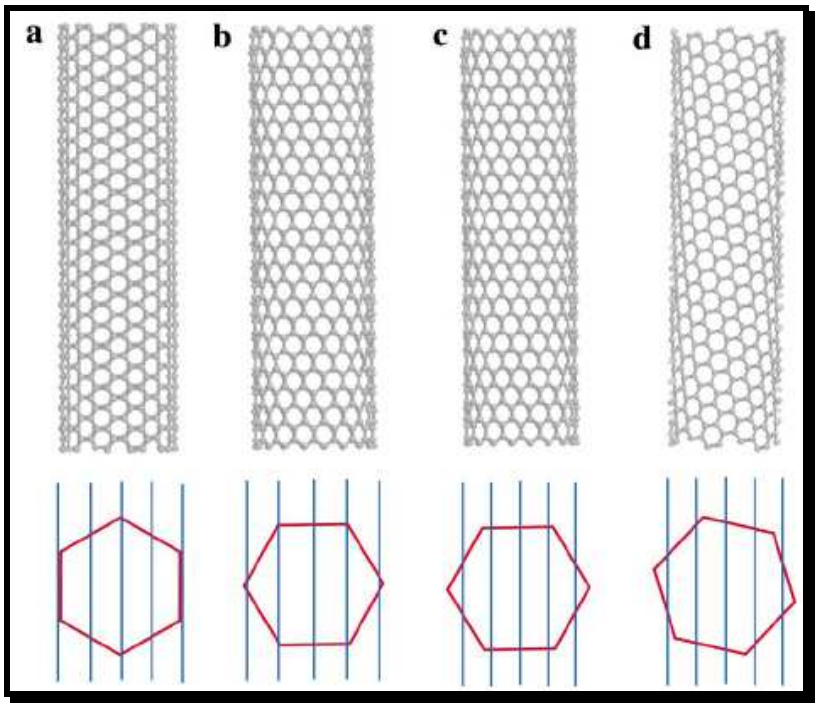

Fig.3 Schematic structures of SWNTs and how they determine the electronic properties of the nanotubes. (a) a (10,10) armchair tube is metallic, (b) a (12,0) zigzag tube can be semiconducting due to the curvature of the nanotube, (c) and (d) a (14,0) zigzag and a (7,16) tube are semiconducting.

Another fascinating aspect of carbon nanotubes is connected to their mechanical properties. Due to their extremely high value of Young's modulus (1.2 TPa), carbon nanotubes are among the strongest materials existing in nature. For example, their tensile strength is about hundred times higher than steel [2].

Due to their excellent properties, a huge effort has been accomplished so far in the production of these materials with desired characteristics and on a larger production scale. CNTs' potential in technological applications sounds really very promising. For example, ensembles of nanotubes have been used for field emission based flat-panel displays or incorporated in other materials to improve their mechanical properties. Single nanotubes have been used for field emission sources, tips for scanning probe microscopy, nanotweezers and chemical sensors. Moreover their nanometric size strongly suggests their employment in nano-scale electronic devices. Incorporation of hetero-dopant atoms into the carbon graphitic network would allow tailoring of CNTs' electronic properties in a

controllable fashion and without structural modification. Natural candidates for this aim result to be boron and nitrogen atoms, since they have comparable atomic size and would fit into the carbon network without altering it. Moreover they have acceptor and donor characters, respectively, which makes them perfect choices in the attempt to modulate nanotubes' electronic properties. Recently several calculations have shown that nitrogen doping can give a strong influence on the transport properties of semiconducting nanotubes [3-6]. In fig.4a the calculated band structures and corresponding densities of states of N-doped CNTs for a nitrogen concentration of 1% is shown [7]. For armchair tubes (metallic), the impurity introduces a peak at about 0.6 eV above the Fermi level, together with several other additional peaks. The impurity state is totally delocalized. More interesting is the case of a zigzag tube (semiconductor) since the extra band of the impurity falls near the bottom of the conduction band leading to a new flat level at about 0.2 eV below the bottom of the conduction band. This localized electronic state can lead the tube to become chemically active and to form covalent bonds with other tubes in case of impurities facing one another.

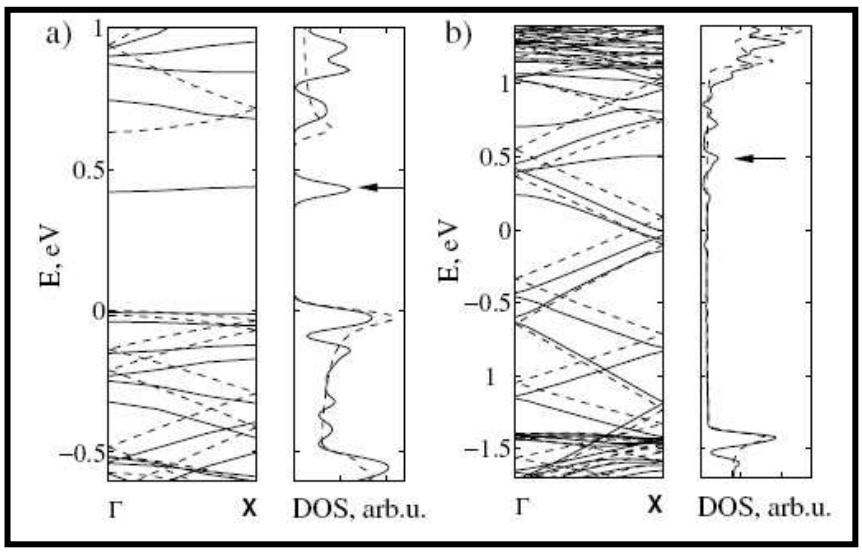

Fig.4a Band structures and corresponding densities of states for a N-doped carbon nanotube (1%) (solid line) versus the folded band structure of a pure nanotube (dashed line) in (a) (8,0) zigzag nanotube, (b) (5,5) armchair nanotube.

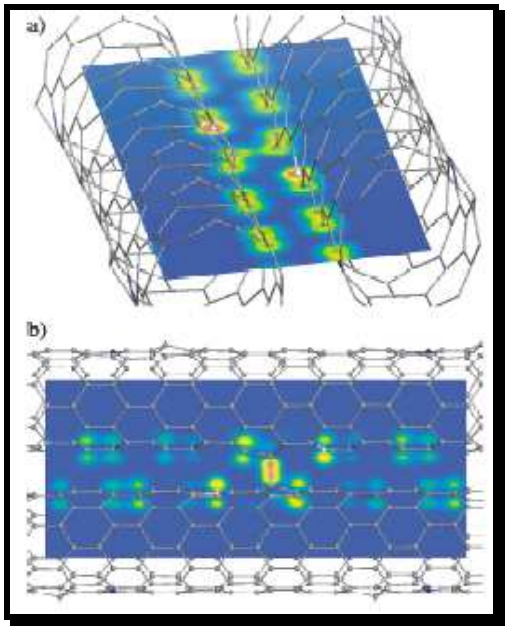

Fig.4b Two nitrogen-doped zigzag nanotubes facing each other.

This is very interesting and opens many possibilities from a device perspective. Indeed such intertube connection (better visualized in fig.4b) will probably change the tunneling properties between the tubes considerably. Moreover, if the density of intertube bonds is high enough, a well packed bundle of SWNTs can be formed and their mechanical properties significantly enhanced.

Many techniques have been employed up to now to synthesize nitrogen doped carbon nanotubes. Chemical vapor deposition [8-10], pyrolysis [11-13] and arc-discharge [14] resulted to be successful in the doping process, even though most of the CNTs produced are multi-walled with a typical bamboo-like morphology. As example, fig.5 shows TEM images of nitrogen-doped carbon nanotubes synthesized by chemical vapor deposition technique using Co-Mo catalysts [15]. The tubes are CN_x multi-walled nanotubes and present a bamboo-shaped structure. Many carbon nitride nanobells are linked together to form the tube. The typical diameter distribution ranges from 9 to 13 nm.

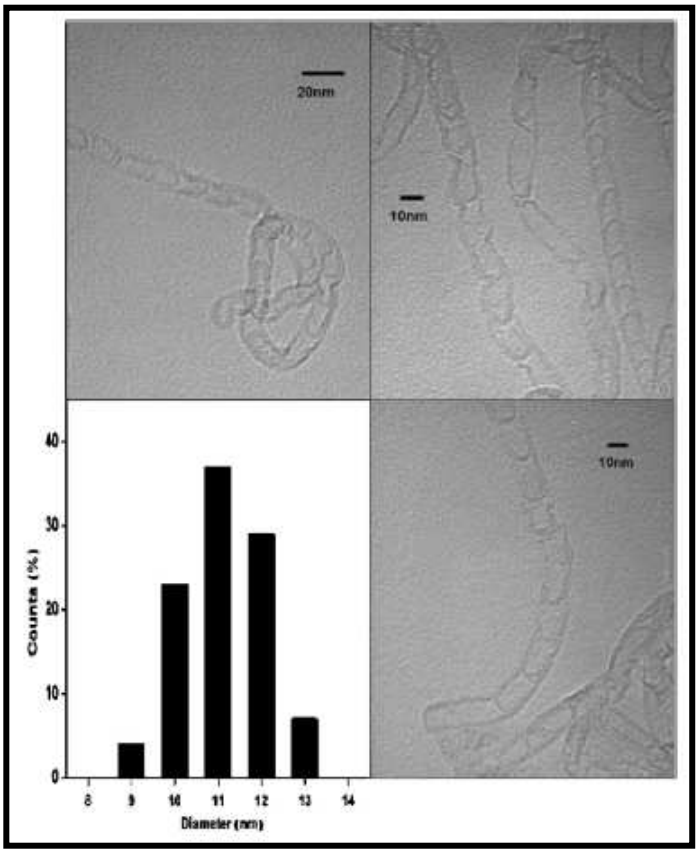

Fig.5 Typical TEM images of bamboo-shaped nitrogen-doped carbon nanotubes.

More complicated is the production of nitrogen doped SWCNTs. Therefore only few groups succeeded in this attempt. A new approach for the synthesis of nitrogen and/or boron doped SWNTs in arch discharge experiments has been proposed by Glerup et al. [16]. Instead of performing the experiment in a nitrogen rich atmosphere, they chose to add organic and inorganic nitrogen rich precursors into the graphitic anode rod. The maximum value of nitrogen concentration achieved is

about 1%, determined using electron energy loss spectroscopy (EELS) and transmission electron microscopy (TEM). Examples of samples produced are shown in fig.6 (a,b).

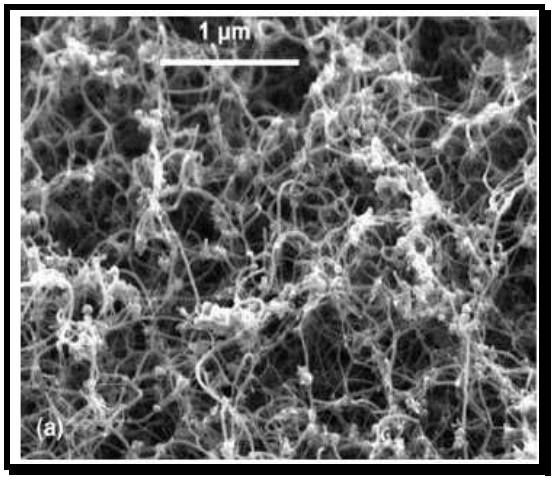

Fig.6a SEM image of nanotubes 1% N-doped.

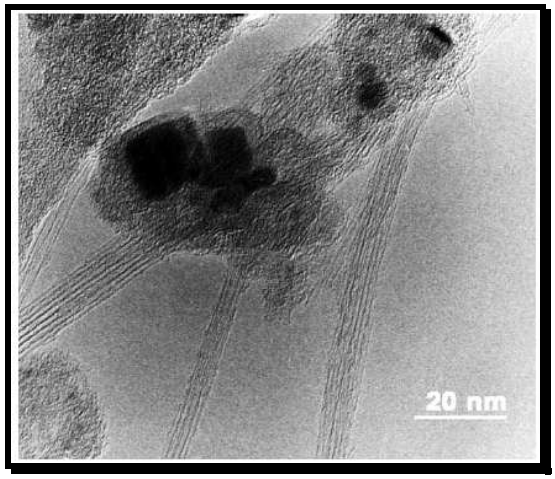

Fig.6b HRTEM image of nanotubes 1% N-doped.

2. Nitrogen implantation in carbon nanotubes : theoretical predictions

Due to recently proposed atomistic computer simulations, a new way of incorporating nitrogen atoms in SWCNTs has been tested. Indeed, using synthesis techniques shown above usually results in most of the nitrogen atoms chemisorbed on the nanotube surface, forming nitrogen molecules intercalated between graphite layers or bondings with irregular carbon structures in sp^3 sites. Only a very tiny percentage of them would occupy the substitutional sp^2 position in the graphitic network. Kotakoski et al. [17] proposed the use of ion irradiation as a tool to dope nanotubes with boron or nitrogen. Using molecular dynamics with empirical potential and density functional force models they showed that during irradiation of single-walled carbon nanotubes with boron or nitrogen atoms up to 40% of the impinging ions can directly occupy the substitutional sp^2 position in the nanotube atomic network. The most probable atomic configurations resulting from simulations during ion irradiation are shown in fig.7(a,b,c,d).

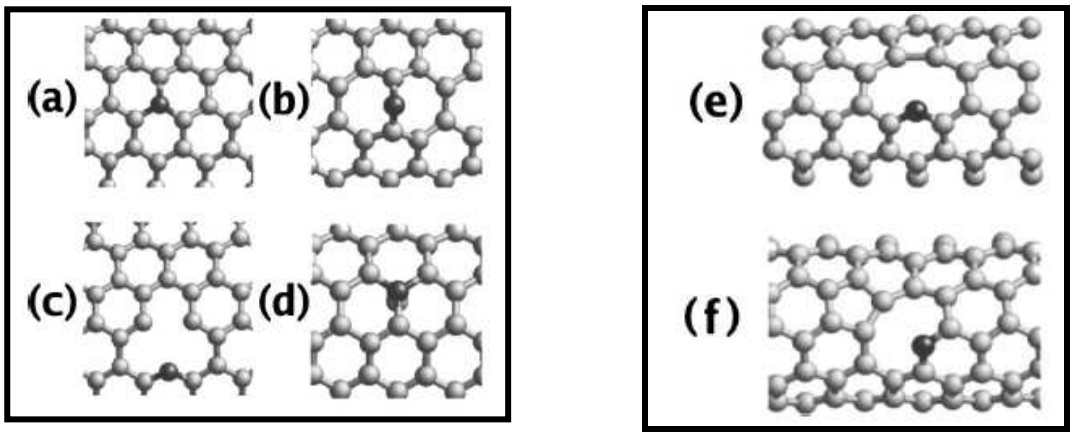

Fig.7 Most abundant atomic configurations after N ion impacts onto SWCNTs. (a) perfect sp^2 impurity, (b) bridge, (c) rocket, (d) sp^2+C configurations in a (10,10) SWNT calculated with the analytical model. (e) and (f) rocket configurations in a (5,5) SWNT calculated with the DFT model

The most important is the substitutional sp^2 configuration with a nitrogen atom replacing a carbon atom in the graphitic network (fig.7a). Fig.7b shows the 'bridge' configuration with the N adatom on the tube surface. Other possibilities are illustrated in fig.7c with the 'rocket defect type' (in case of an impacting ion displacing a carbon atom from its site and replacing another one) and in fig.7d with the 'sp^2+C defect type' (in this case the dopant atom has replaced a carbon atom which remains bonded to the dopant). It is also possible to calculate the number of dopant atoms with different coordination numbers per one impinging ion. In fig.8 this is shown as a function of the ion energy. In case of N ions the probabilities for three-coordinated dopant atoms, which will mostly result in the substitutional configuration, can almost reach the value of 50% at the energy of about 50 eV. Then this probability decreases with the ion energy together with the fraction of ions that remain in the tube during irradiation. Considering only N atoms which remain in the tube, simulations show that the probability to occupy a site in the sp^2 configuration can reach the value of 65% at 50 eV before annealing. The probability decreases to 55% at 300 eV. The reason of the highest probability at about 50 eV is explained in terms of energy transfer. According to their model it is necessary for a C atom to acquire a kinetic energy of ~ 25 eV to be able to move from its site. Considering head-on collisions in the frame of the binary collision approximation, this leads to an ion energy of about 30 eV. Nevertheless, it must also be considered that in simulations the impact parameter is randomly distributed and the atom kinetic energy will be partially lost in multi-atom interactions. This causes an increase of the most suitable energy to 50 eV. At higher values of kinetic energy the probability that impinging ions can pass through the tube increases.

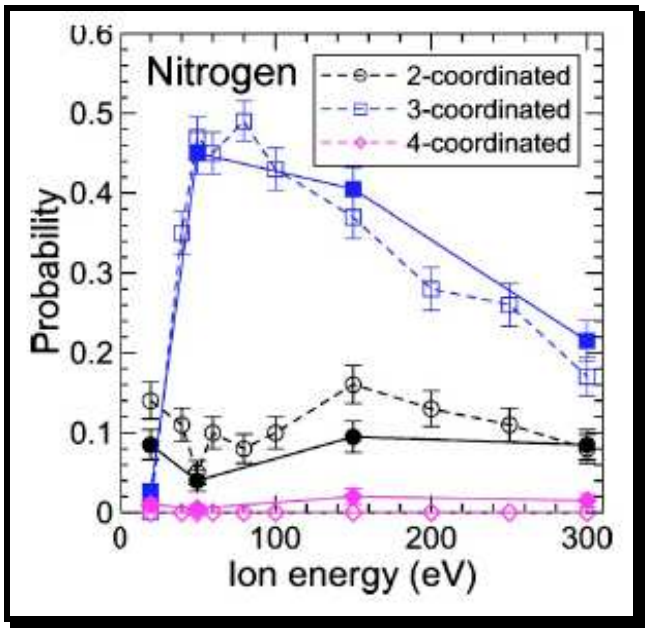

Fig.8 Probabilities for coordination numbers for N as functions of the initial ion energy. The open/full symbols stand for the results before/after annealing.

Sample annealing after irradiation will result in an increase of the number of dopant atoms in the sp^2 configuration due to their thermal migration and annihilation with vacancies created by energetic recoils. Moreover, even if irradiation is performed at energies higher than 50 eV, vacancies created in the process are supposed to recombine with dopant atoms when they become mobile in the sample.

Experimental works recently performed confirmed the efficiency of ion implantation in incorporating dopants in carbon nanotubes. Irradiation of SWCNTs with N_2^+ ions at energy of 0.5 keV and flux equal to 15 nA/cm^2 has been reported [18]. The samples have been investigated by atomic force microscopy (AFM) in order to get information about their morphology and mechanical properties before and after irradiation, and x-ray photoelectron spectroscopy (XPS) to check the nitrogen concentration and chemical bondings. The authors found that the morphology of the tubes is preserved after irradiation for 17 and 47 minutes. Moreover XPS analysis shows that there are two components in the N 1s core level spectra related to nitrogen atoms bonded to carbon atoms in sp^2 and sp^3 configuration. Deconvolution of the C 1s signal confirms this attribution (see fig.9). AFM analysis gives information about the tube hardness and its evolution in time as well. During nitrogen implantation CNT hardness increases. This corresponds to an increase in the XPS spectra of the intensity of the sp^3 bonded nitrogen atoms, which is in agreemet with theoretical

expectations. Another experiment about nitrogen doping in SWCNTs has been performed with 3 keV N_2^+ implantation at room temperature for a N:C atomic ratio varying from 0.06 to 0.12 [19]. Samples have been analysed by XPS to check the nitrogen concentration and chemical bondings and by EELS to monitor the level of damage induced by ion irradiation.

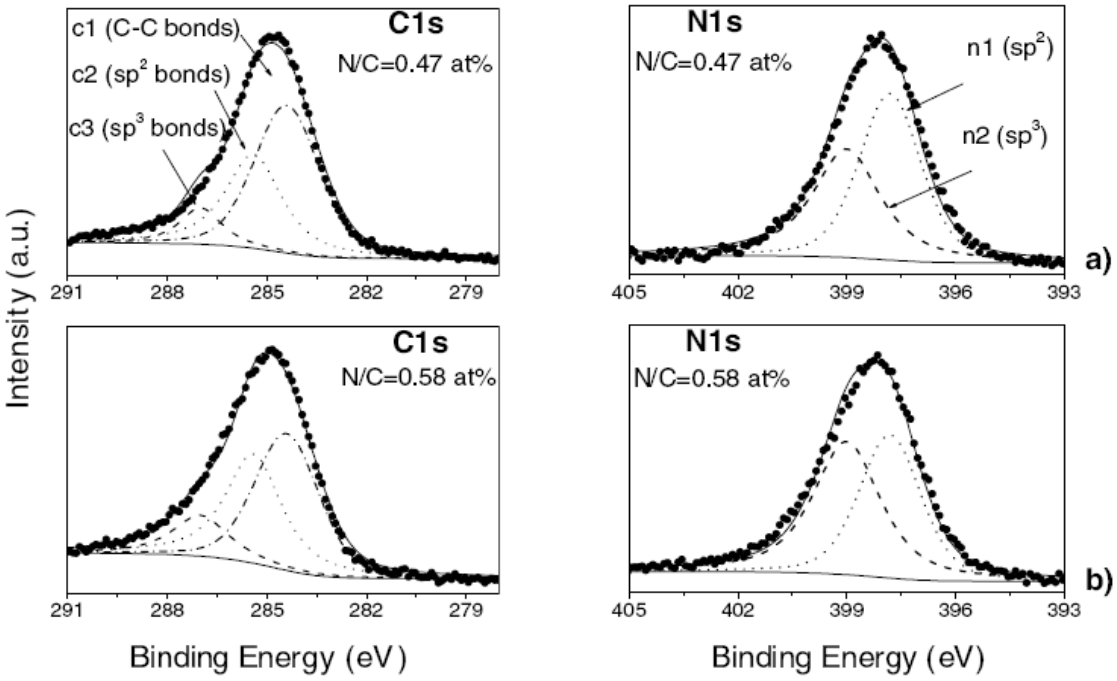

Fig.9 Deconvoluted C1s and N1s spectra. Experimental data (dots), components attributed to different bonds (dashed and dotted lines) and fitted results (solid lines).

X-ray photoelectron spectroscopy analysis shows that nitrogen atoms are bonded to carbon atoms in three different configurations : tetrahedral sp^3, pyridine-like and substitutional triangular sp^2 configurations and these species are stable for annealing at 650 K. Samples have been annealed up to 1200 K showing that the most stable dopant atoms are those which are bonded in the substitutional configuration. Energy loss spectra for clean SWNTs show two peaks: the first at about 6 eV is attributed to 2p π-π^* transition and the broad structure at 27 eV is due to plasma loss with both π and σ characters. During N_2^+ irradiation the intensity of the first peak is strongly reduced while it partially recovers when the sample is annealed to high temperature (see fig.10a).

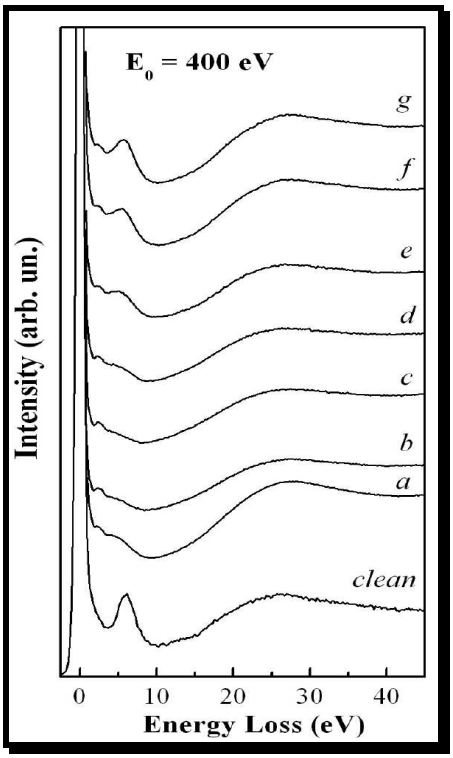

Fig.10a Electron energy loss spectra for N_2^+ irradiated SWNTs and subsequent annealing. (e-g). The bottom-most curve is for clean and undoped sample.

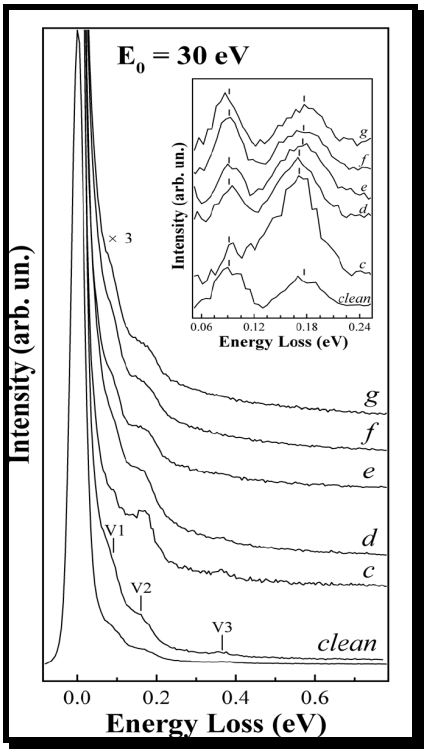

Fig.10b High resolution electron energy loss spectra for N_2^+ irradiated SWCNTs and subsequent annealing (e-g). The bottom-most curve is for clean and unbombarded sample.

A similar behaviour of the π-loss feature has already been observed in experiments of CNT irradiation with Ar^+ and Ne^+ ions and attributed to increased level of disorder and damage in the tube network during sputtering [19]. The authors attribute the observed changes in the EELS spectra to similar reasons and justify the increase of the π signal upon annealing with a partial restoring of the tube network. This is also confirmed by high resolution electron energy loss measurements shown in fig.10b. For clean SWNTs the peaks V1and V2 at 90 meV and 175 meV are assigned to radial and tangential optical modes of phonon excitations, respectively. The peak V3 at 360 meV is attributed to C-H stretching bonds in aromatic rings. During ion irradiation, decrease of V1 and increase of V3 is observed indicating the presence of disorder and defects with carbon dangling bonds to which hydrogen atoms can bind. The reduction of V3 upon annealing indicates the restoring of the initial carbon structure.

The efficiency of ion irradiation in doping carbon nanotubes has been recently proven also in case of alkali metal dopants. Alkali metals intercalation in CNTs is usually performed by mean of vapor

deposition by thermally diffused gas, capillary wetting of liquid face substances or direct soaking in the solution. These techniques, however, allow to introduce only a single species dopant with a more or less uniform distribution. On the contrary, through ion irradiation it is possible to localize dopants in a well defined sample region, which could result very useful for practical applications. Collisionally excited autoionization electron spectroscopy has been used to study the interaction of slow Na^+ ions with both SWNT and MWNT mats [20]. This spectroscopy is based on energy analysis of electrons emitted by autoionization decays of sodium atoms excited by electron promotion in collisions between an incoming sodium projectile and a sodium atom previously deposited on the sample. The deposition has been performed in two ways: implantation due to the ion beam itself and evaporation of sodium atoms on the target before ion irradiation. In the first case an intense and time increasing Na autoionization electron signal has been observed during ion irradiation, which confirms the presence of sodium atoms on the surface. They stick on it and remain localized there. An example of such a kind of signal and its evolution in time is shown in fig.11.

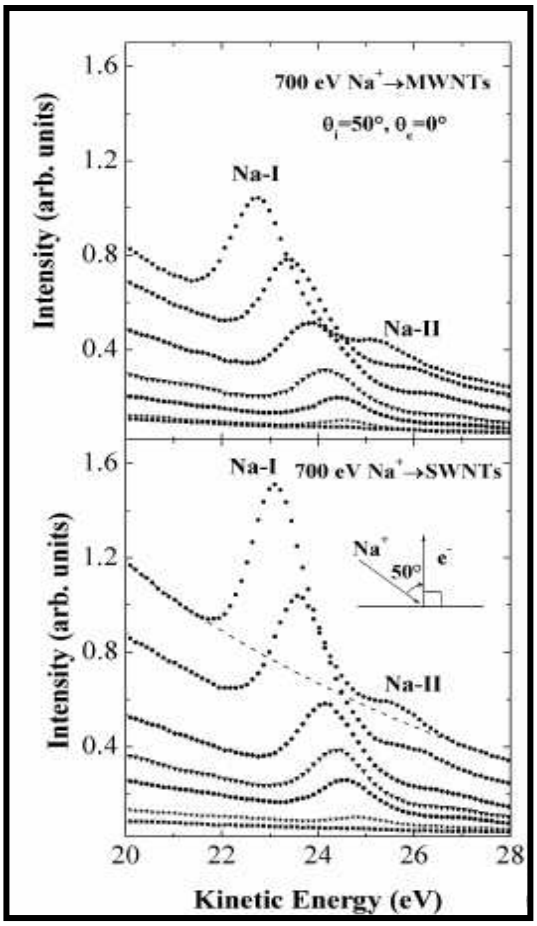

Fig.11 Autoionization electron spectra taken during 700 eV Na^+ ion irradiation on MWCNTs (upper panel) and SWCNTs (lower panel).

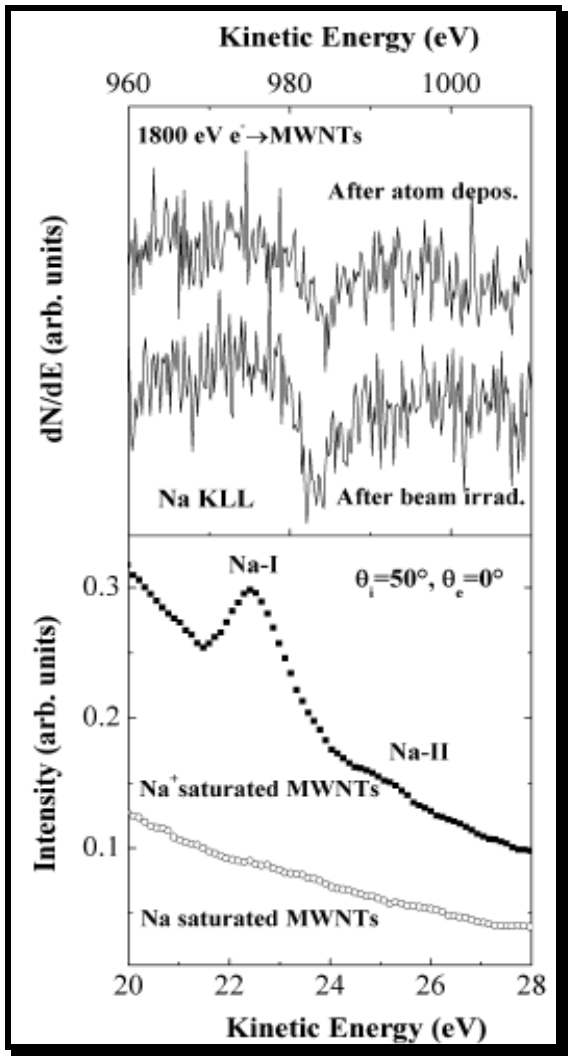

Fig.12 Na KLL Auger electron spectra at saturation coverages for MWCNTs after Na atom deposition and after 300 eV Na^+ ion irradiation (upper panel-a) and autoionization electron spectra during 300 eV Na^+ ion irradiation on Na^+ and Na saturated MWCNTs (lower panel-b)

Very different is the case in which sodium atoms are evaporated on the sample before ion irradiation. No detectable signal of autoionization decay of excited sodium atoms (see fig.12b) is observed from the sample which indicates both a poor sticking efficiency and large mobility to diffuse in the bulk of the dopants. Moreover the maximum concentration of sodium atoms which can be reached in MWNTs by both evaporation and ion irradiation has been checked. In fig.12a Na-KLL Auger electron spectra at saturation coverages for MWNTs are plotted. Auger electron spectroscopy shows that in the first case sodium concentration is nearly half of the concentration reached in the second case.

References

[1] M.S. Dresselhause, G. Dresselhause, Carbon nanotubes : syntesis, structure, properties and applications, Ph. Avouris (Eds), Berlin (Springer 2000).

[2] Hongjie Dai, Surf. Sci. 500, 218 (2002).

[3] C.C. Kaun, B. Larade, H. Mehrez, J. Taylor, and H. Guo, Phys. Rev. B 65, 205416 (2002).

[4] D. Srivastava, M. Menon, C. Daraio, S. Jin, B. Sadanadan, and A. M. Rao, Phys. Rev. B 69, 153414 (2004).

[5] H.S. Kang and S. Jeong, Phys. Rev. B 70, 233411 (2004).

[6] G. Keskar, R. Rao, J. Luo, J. Hudson, J. Chen, and A. M. Rao, Chem. Phys. Lett. 412, 269 (2005).

[7] A.H. Nevidomskyy, G. Csannyi, and M.C. Payne, Phys. Rev. Lett. 91, 1055021 (2003).

[8] K. Suenaga, M. Yudasaka, C. Colliex, and S. Iijima, Chem. Phys. Lett. 316, 365 (2000).

[9] L.H. Chan, K.H. Hong, D.Q. Xiao, T.C. Lin, S.H. Lai, W.J. Hsieh, and H.C. Shih, Phys. Rev. B 70, 125408 (2004).

[10] Y.T. Lee, N.S. Kim, S.Y. Bae, J. Park, S.C. Bae, J. Park, S.C.Yu, H. Ryu, and H.J. Lee, J. Phys. Chem. B 107, 12958 (2003).

[11] H.C. Choi, J. Park, and B. Kim, J. Phys. Chem. B 109, 4333 (2005).

[12] X. Wang, Y. Liu, D. Zhu, L. Zhang, H. Ma, N. Yao, and B. Zhang, J. Phys. Chem. B 106, 2186 (2002).

[13] M. Terrones, P. Redlich, N. Grobert, S. Trasobares, W.K. Hsu, H. Terrones, Y.Q. Zhu, J.P. Hare, C.L. Reeves, A.K. Cheetham, M. Ruehle, H.W. Kroto, and D.R.M. Walton, Adv. Mater. 11, 655 (1999).

[14] R. Droppa, C.T.M. Ribeiro, A.R. Zanatta, M.C. dos Santos, and F. Alvarez, Phys. Rev. B 69, 045405 (2004).

[15] S.H. Lim, H.I. Elim, X.Y. Gao, A.T.S. Wee, W. Ji, J.Y. Lee, and J. Lin, Phys. Rev. B 73, 045402 (2006).

[16] M. Glerup, J. Steinmetz, D. Samaille, O. Stephan, S. Enouz, A. Loiseau, S. Roth, and P. Bernier, Chem. Phys. Lett. 387, 193 (2004).

[17] J. Kotakoski, A.V. Krasheninnikov, Yuchen Ma, A.S. Foster, K. Nordlundm and R.M. Nieminen, Phys. Rev. B 71, 205408 (2005).

[18] C. Morant, J. Andrey, P. Prieto, D. Mendiola, J.M. Sanz, and E. Elizalde, Phys. Stat. Sol. A 203, 1069 (2006).
[19] F. Xu, M. Minniti, C. Giallombardo, A. Cupolillo, P. Barone, A. Oliva, and L. Papagno, Surf. Sci. 601, 2819 (2007).
[20] M. Commisso, A. Bonanno, M. Minniti, P. Barone, P. Riccardi, A. Oliva, L. Papagno, and F.Xu, Surf. Sci. 601, 2832 (2007).

Chapter 2

Nitrogen implantation in single-walled carbon nanotubes

1. Experimental results

A SWCNT bucky paper of nominal 100 μm thickness has been irradiated with a 300 eV N_2^+ beam and then analysed using x-ray photoelectron spectroscopy and reflection electron energy loss spectroscopy (REELS). Experiments have been performed in a UHV chamber equipped for standard surface analysis with a base pressure of $1x10^{-9}$ Torr. The sample was mounted on a hollow sample holder and kept fixed by sandwiching it between four stainless steel disks. The pristine sample was analysed by scanning electron microscopy (SEM) to characterise CNTs' structure. Fig.1a shows a typical SEM image: SWCNT bundles with a tube diameter distribution centered around 1.4 nm are clearly visible.

Before N_2^+ implantation the sample was cleaned in situ by several annealing cycles at a temperature of about 1000°C monitored with an optical pyrometer. Annealing has been performed by directly passing a current through the sample. After heating an oxygen concentration of about 1% was still detected, most probably due to the oxide form of nickel catalyst.

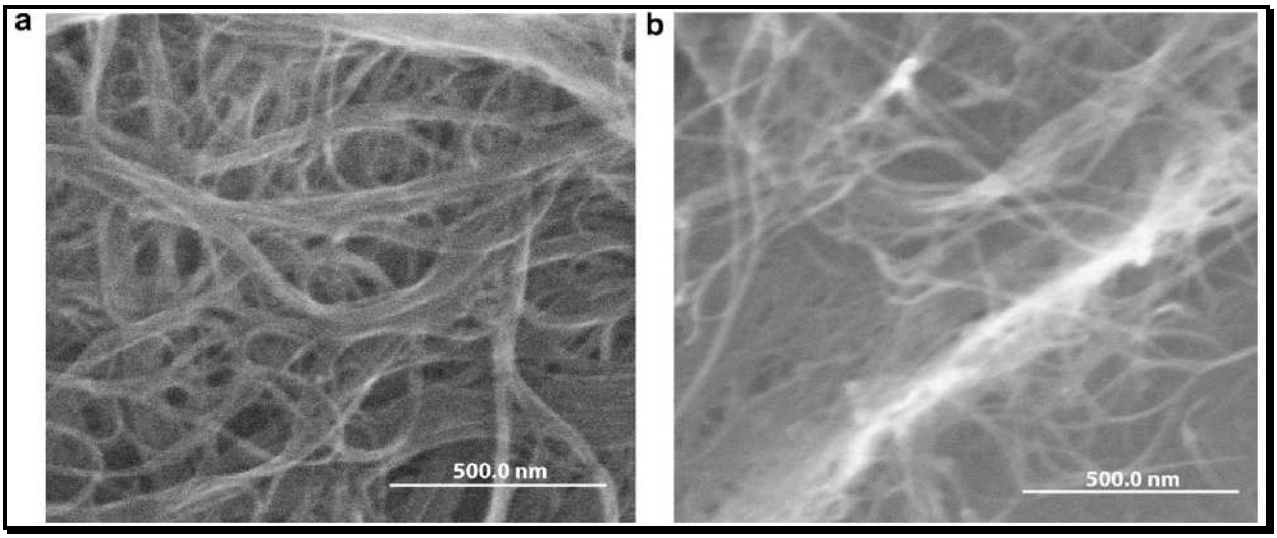

Fig.1 Sem images of carbon nanotube samples, before (a) and after (b) ion irradiation.

300 eV N_2^+ ions were produced in a differentially pumped cold cathode ion source and focused on the sample along normal incidence direction. During irradiation the beam has been rastering over the whole surface area of 7 x 8 mm^2 to have the best possible lateral homogeneity. The current density was in the order of 0.5 nA/mm^2. Because of the high reactivity of the defected SWNTs, the oxygen contamination level raised to up to 3-4 % after long time ion irradiation but sensitively decreased after heating and for final annealing at 1000°C it was reduced to the original value of about 1%. Nitrogen implantation was performed at room temperature in consecutive steps and the ion fluence Φ_{N_2} reported here refers to the total cumulative irradiation amount. After the final exposure to the ion beam for $\Phi_{N_2} = 2x10^{15} ions/cm^2$, the N-doped SWCNT sample was heated to T=400°C for 20 min and then cooled down at room temperature to take measurements. Further cycles of annealing to higher temperatures for 20 min each were successively taken and the highest temperature was 1000°C. In fig.1b a SEM image of N-doped SWCNTs after the last annealing is shown. The tube structure is still visible so it has been preserved during experiments. Non monochromatic Al K_α x-ray ($h\nu$ = 1486.6 eV) was used as excitation source for core level photoemission spectroscopy studies. Reflection electron energy loss spectroscopy measurements were also taken with an electron gun operating at a primary energy of E_p = 400 eV. Emitted electrons were collected with a rotatable hemispherical energy analyzer mounted on a goniometer. The analyzer had an acceptance angle of 2° and was operated with a constant pass energy of 100 eV. The full width at half maximum was 0.8 and 1.7 eV for reflected electron elastic peak and C1s peak, respectively. Table1 is a summary of all experimental steps indicating the nitrogen ion fluence

Φ_{N_2} and the subsequent annealing temperature. Also given is the nominal nitrogen concentration ρ_N as determined from the N1s and C1s core level photoemission intensities at normal emission direction:

$$\rho_N = \frac{I_{N1s}/\sigma_{N1s}}{I_{C1s}/\sigma_{C1s} + I_{N1s}/\sigma_{N1s}} \qquad (1)$$

with σ_{N1s} and σ_{C1s} are the photo-ionization cross sections.

Table 1 – Experimental steps of N_2^+ ion implantation and subsequent annealings

Φ_{N_2} (ions/cm^2)	0	7.7×10^{13}	1.7×10^{14}	2.6×10^{14}	3.6×10^{14}	4.6×10^{14}	6.3×10^{14}	9.6×10^{14}	1.4×10^{15}	2.0×10^{15}
ρ_N (at.%)	0	1.5	2.7	3.7	4.3	4.9	6.1	8.5	10.0	11.3
T (°C)	400	500	600	700	800	900	1000			
ρ_N (at.%)	10.1	9.3	7.7	6.5	5.6	3.4	1.6			

Table 1 Experimental steps of N_2^+ ion implantation and subsequent annealings.

To investigate the atomic nitrogen doping concentration and the dopant depth profile, both N1s and C1s core level photoemission intensities I_{N1s} and I_{C1s} at three different emission angles (θ_e=70° for grazing emission, θ_e=40° and θ_e=0° for normal emission) have been measured. The calculated nitrogen concentration ρ_N is plotted in fig.2 as a function of ion fluence and annealing temperature. It can be immediately noticed that for as-implanted N-SWCNTs ρ_N is smaller on the surface and in the near surface region than in the deeper zone indicating that nitrogen particles do penetrate in the bulk. In fig.3a ρ_N as a function of θ_e for the sample irradiated with $\Phi_{N_2} = 2x10^{15} ions/cm^2$ at room temperature followed by heating at T=600° is shown. In case of as irradiated SWNTs, it is possible to note that the polar angle dependence of ρ_N is quite similar to that reported by Palacio et al. [1] for 1 keV N_2^+ implantation into a graphite sample along an incidence angle of 55° with respect to the surface normal.

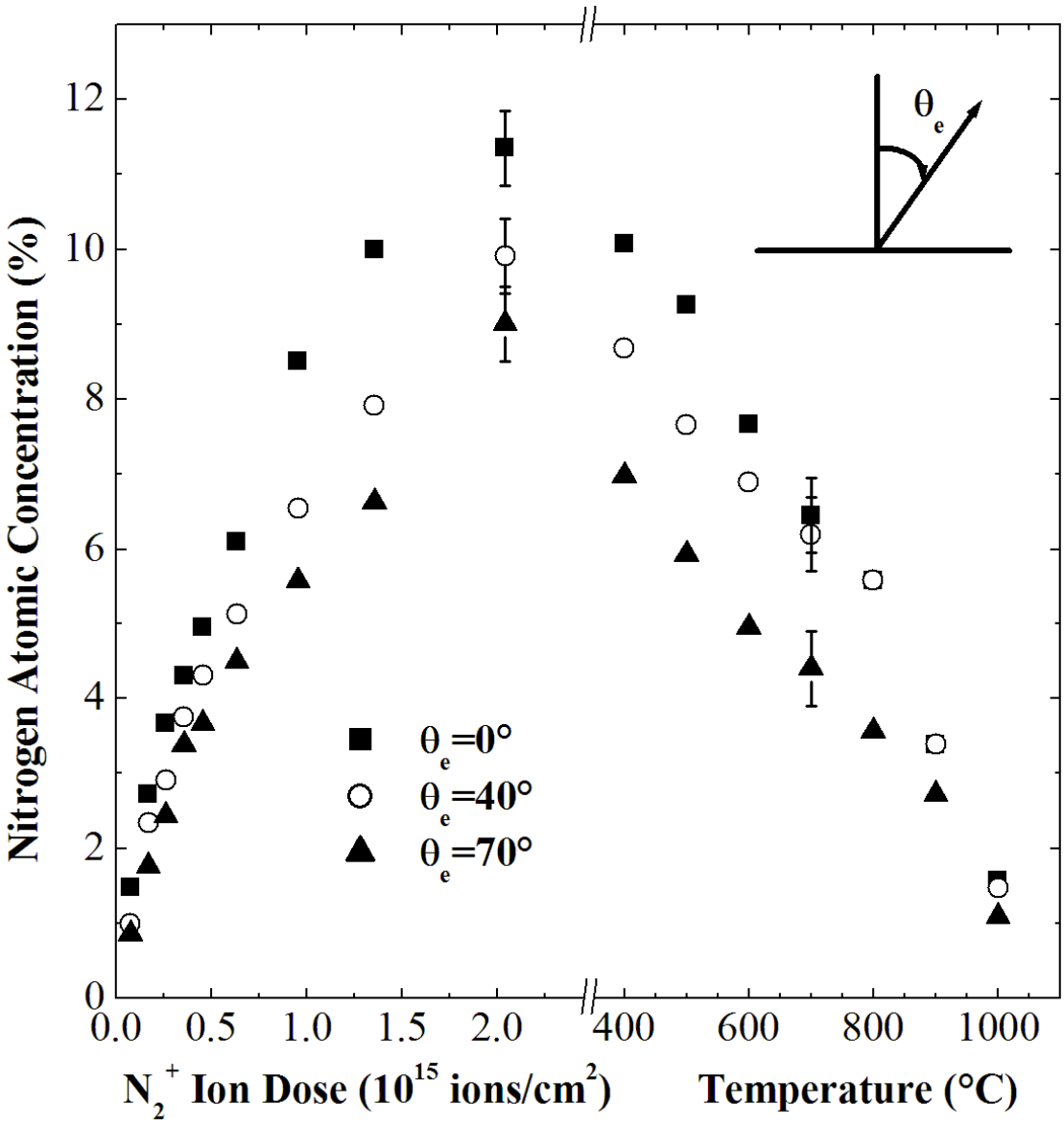

Fig.2 Nitrogen atomic concentration measured at three different emission angles as function of N_2 ion dose and annealing temperature. They are determined from the N1s and C1s core level XPS spectra after correction for the photo-ionization cross sections.

It is well known that the detected photoemission intensity of an atomic species *x* having a concentration profile $c_x(z)$, with *z* being the distance measured from the sample surface, can be written as:

$$I_x(\theta) \propto \frac{\sigma_x}{\lambda_x \cos\theta} \int_0^\infty c_x(z) \exp\left(-\frac{z}{\lambda_x \cos\theta}\right) dz \qquad (2)$$

In the present case, N1s and C1s photoelectrons have quite similar kinetic energies of about 1086 and 1215 eV, respectively, so they should have nearly the same inelastic mean free path λ. Therefore, the measured polar angle dependence of $\rho_N(\theta)$ is directly correlated to $c_N(z)$ as:

$$\rho_N(\theta) = \frac{I_{N1s}(\theta)/\sigma_{N1s}}{I_{C1s}(\theta)/\sigma_{C1s} + I_{N1s}(\theta)/\sigma_{N1s}} = \frac{1}{\lambda\cos\theta}\int_0^\infty c_N(z)\exp\left(-\frac{z}{\lambda\cos\theta}\right)dz \qquad (3)$$

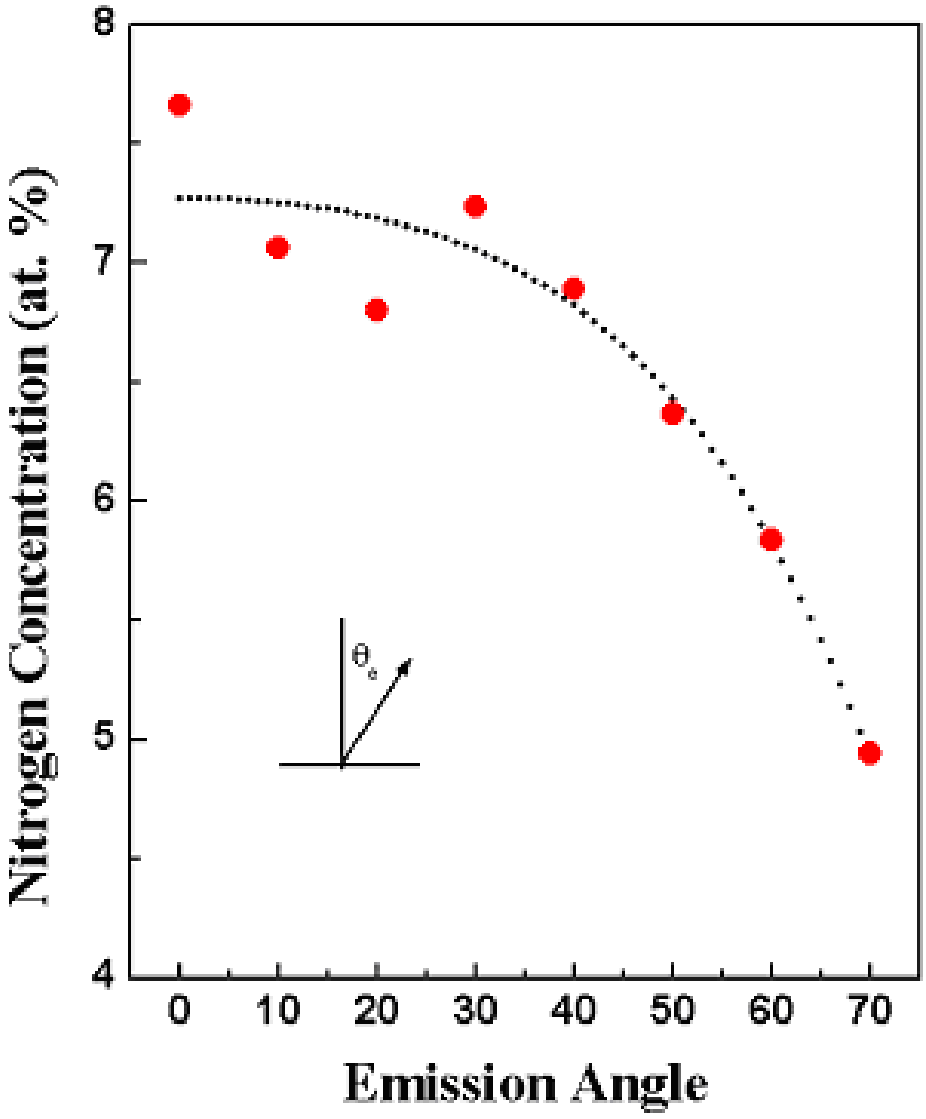

Fig3a N dopant concentration ρ_N as a function of emission angle θ_e for the sample irradiated with $\Phi_{N_2} = 2x10^{15} ions/cm^2$ at room temperature followed by heating to T=600°C. The dotted curve is the fitting using the concentration depth profile shown in fig.3b

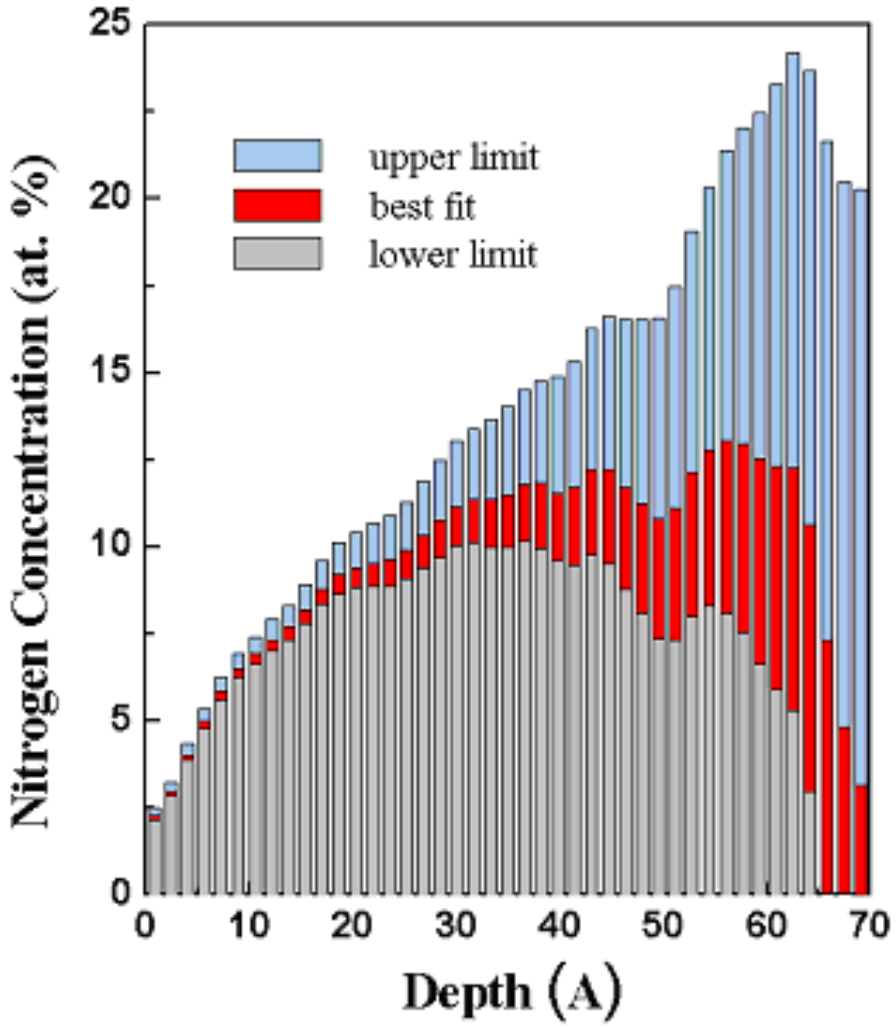

Fig3b Nitrogen concentration depth profile calculated with eq.(4) (red region). The grey and blue histograms represent the uncertainties defined by an increase of 1% in the minimum χ^2 value.

This integral equation has been solved numerically by dividing the probed region (assumed to be ~ 4λ thick) into n = 50 equally spaced slices and optimizing the concentration profile by the least square best fitting:

$$\sum_j \left[\rho_N(\theta_j) - \frac{1}{\lambda \cos\theta_j} \int_0^\infty c_N(z) \exp\left(-\frac{z}{\lambda \cos\theta_j} \right) dz \right]^2 = \min \qquad (4)$$

in which $\rho_N(\theta_j)$ are the measured values. The so obtained theoretical nitrogen atomic concentration depth profile is depicted in fig.3b for the case studied. The fitting to the experimental data is also shown in fig.3a as dotted lines.

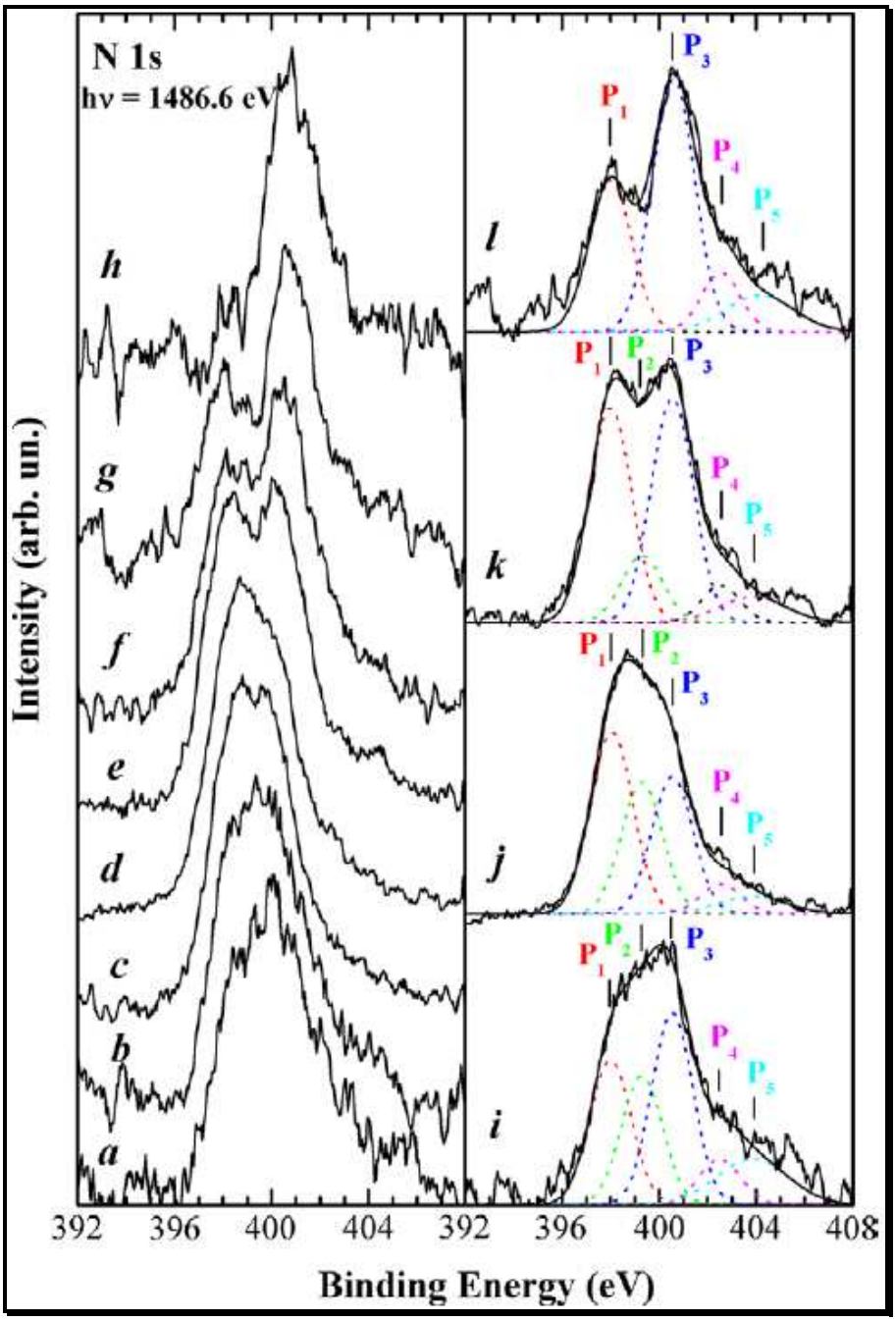

Fig.4 Left panel: Normalized N 1s core level photoemission spectra for several ion doses of *a)* $\Phi_{N_2} = 1.7x10^{14} ions/cm^2$; *b)* $\Phi_{N_2} = 3.6x10^{14} ions/cm^2$; *c)* $\Phi_{N_2} = 9.6x10^{14} ions/cm^2$; *d)* $\Phi_{N_2} = 2x10^{15} ions/cm^2$; and post irradiation annealing at temperatures of *e)* *T*=400°C; *f)* *T*=600°C; *g)* *T*=800°C; *h)* *T*=1000°C. Right panel: some representative N1s line shape curve fitting schemes for *i)* $\Phi_{N_2} = 2.6x10^{14} ions/cm^2$; *j)* $\Phi_{N_2} = 2x10^{15} ions/cm^2$; *k)* *T*=500°C; *l)* *T*=800°C. Note that the binding energies of all components are constant and for their identification see text.

In doing so, it is assumed λ = 2 nm. A different choice of λ changes somehow the absolute values of $c_N(z)$ but leaves the overall profile shape unaltered. A larger (smaller) value of λ shifts the maximum of $c_N(z)$ to deeper (shallower) z and makes it slightly broader (narrower). It must be mentioned that because of the exponential factor in eq.(4), the uncertainty associated to $c_N(z)$ increases greatly with z and becomes quite insensitive to the dopant concentration in the region deeper than 3λ. Indeed the contribution to the measured intensity is only less than a few percent. To make a rough estimate of the concentration uncertainty, a single fitting parameter was allowed to vary to yield an arbitrary increase of 1% in the minimum χ^2 value and the so determined upper and lower limits of $c_N(z)$ are also shown in fig.3b as blue and grey histograms, respectively. Increasing the number of slices n of the sampling region produces little effects on the profile. In the left panel of fig.4, N1s core level photoemission spectra for several ion fluences and annealing temperatures are shown. These spectra were taken at normal emission and have been corrected for the analyzer transmission factor, Shirley-type background subtracted, normalized to the same height and vertically shifted to emphasize line shape evolution. The energy scale has been calibrated so that the maximum of C1s core emission is centered at a binding energy BE = 284.5 eV for clean SWCNTs. Looking at curves (a), (b), (c) and (d) it can be seen how continuous N_2^+ irradiation on SWCNTs at room temperature results in a gradual change of N1s line shape.

In particular a structure at lower BE grows. Spectra taken after annealing (e), (f), (g) and (h) present sharper spectroscopic features showing in a certain temperature range two well separated peaks. To gain more detailed insight into the nitrogen chemical bonding nature, core level energy distribution curves (EDCs) have been fitted using a series of Gaussian functions. Examples of the used deconvolution schemes are shown in the right side of fig.4. For room temperature, in as-implanted N-SWCNTs the N1s spectra are very broad and can be consequently well fitted with 2-3 or even more components at nearly quite arbitrary binding energies with different line widths and relative intensities. The best choice to overcome the large uncertainty is to analyse first the spectra taken after annealing at 600, 700 and 800°C for which two well distinct peaks are clearly resolved. These two peaks are indicated as P_1 and P_3 in fig.4. They have constant binding energies of 398.0 ± 0.1 and 400.5 ± 0.1 eV and full width at half maximum of 2.0 ± 0.1 eV. This indicates that the chemical bonding environments are the same for nitrogen dopant atoms in these annealed N-SWCNTs. The tail at higher BEs has been fitted with two small structures indicated as P_4 and P_5 at energies of 402.3 ± 0.2 and 403.4 ± 0.2 eV, respectively.

Their total spectral weight is only about 10-20%. For samples annealed at lower temperatures, it can be noticed that the valley between peaks P_1 and P_3 is gradually filled. This can not be simply explained by a broadening of the two main peaks and it is necessary to introduce a new component

at a binding energy of 399.3 ± 0.1 eV marked as P_2. This decomposition scheme with constant BEs and widths can well reproduce the whole set of spectra and its self-consistence gives a good confidence in the analysis procedure. It is interesting to mention that in literature there is a large variety of XPS studies on nitrogen containing carbon materials and N1s line shape curve fitting employing components with varying energies and widths often resulted in arbitrary and controversial peak assignment. Decomposing a set of XPS curves using components with fixed binding energies implies the assumption of well defined chemical environments while other parameters like dopant concentration, defects and temperature are changed. In fig.5 the total and component specific N concentration as a function of N_2^+ ion fluence and annealing temperature is shown.

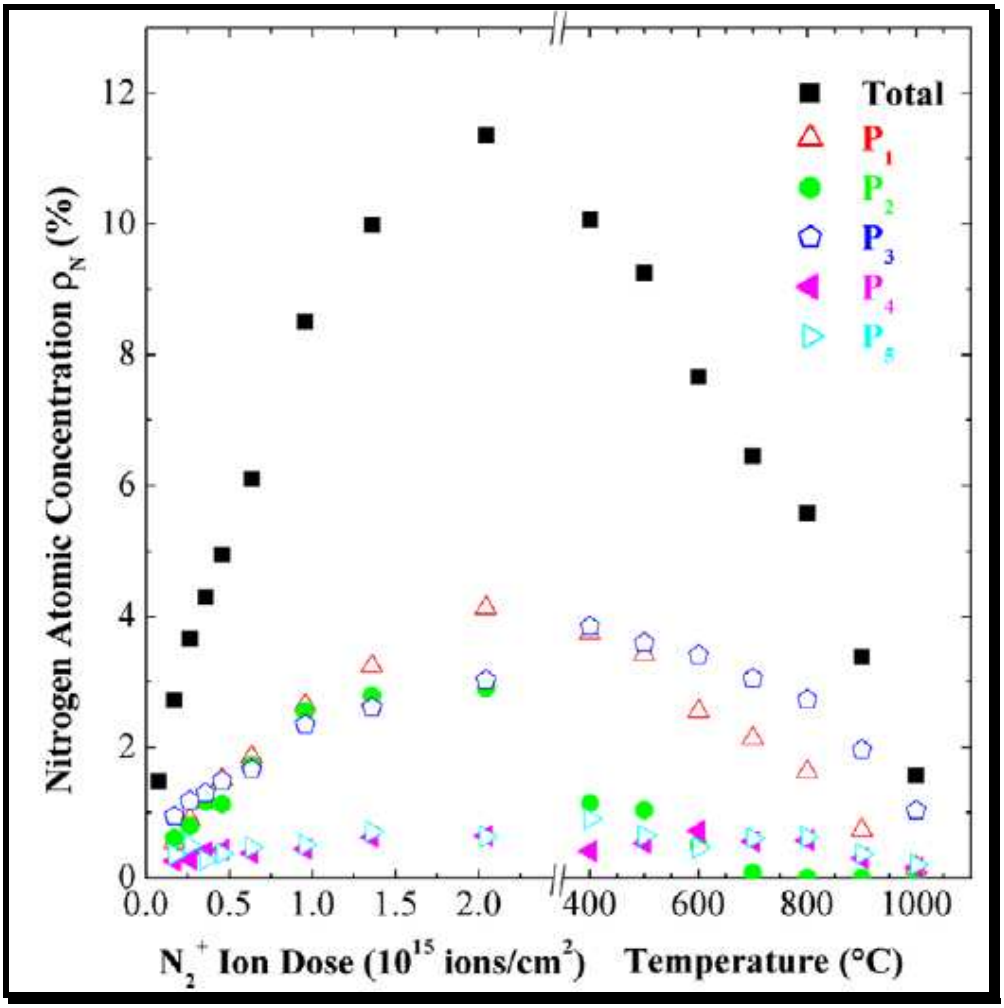

Fig.5 Total and component specific N concentration as a function of N_2^+ ion dose and annealing temperature. P_1, P_2,… are the fitting components using in the right panel of fig.4.

In the first stage of doping, peak P_3 is the most relevant component but P_1 increases faster with Φ_{N_2} and its intensity reaches that of P_3 at $\Phi_{N_2} = 4.6x10^{14} ions/cm^2$ and becomes the dominant species afterwards. Annealing causes a partial loss of nitrogen dopant atoms in the probing region due to sublimation and/or diffusion into deeper zones. The bond corresponding to the peak at 400.5 eV is the most stable one against heating to high temperatures. The relative abundance of each N species is indicated as: $R_i = \frac{I_i}{I_{N1s}}$, where the index *i* stands for P_1, P_2, etc. It is plotted as a function of the total nitrogen content in fig.6 for as irradiated (left panel) and annealed (right panel) samples.

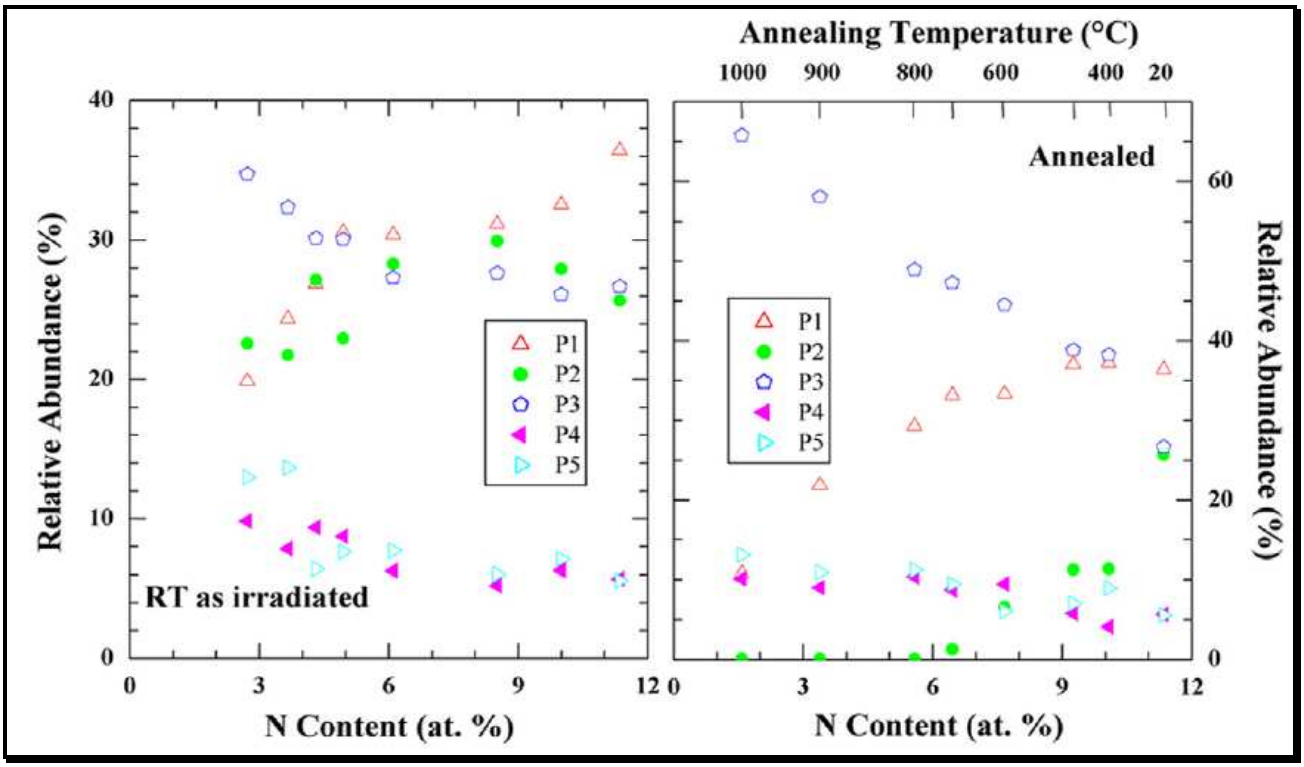

Fig.6 Relative abundance of various components of N1s core level spectra shown in fig.4

Nitrogen doping into SWCNTs certainly induces profound modifications in the electronic band structures and such information can be closely followed by REELS. In fig.7 some spectra taken with a primary energy of E_p=400 eV are shown.

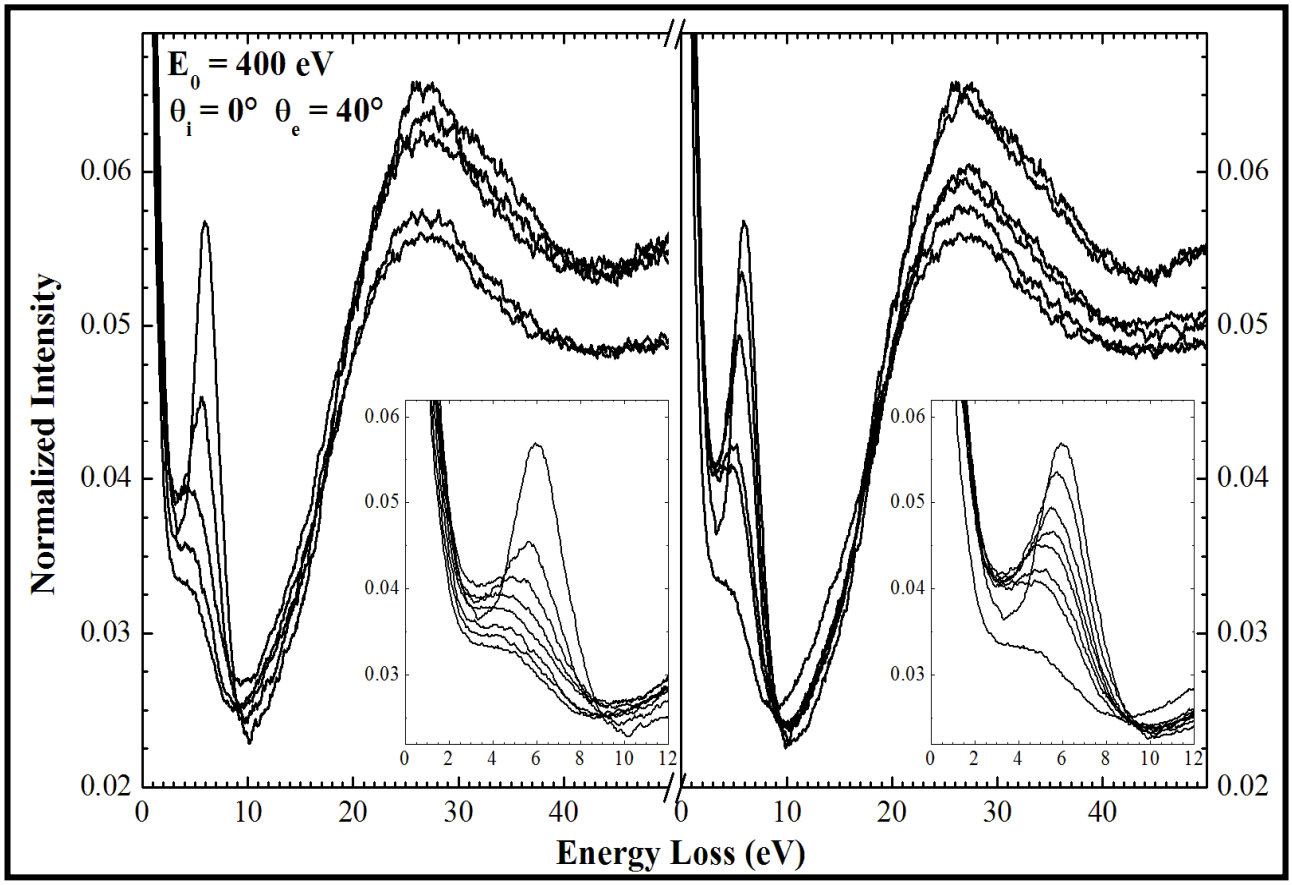

Fig.7 REELS taken with a primary energy of Ep=400 eV. The incidence and emission angles were 0° and 40°, respectively, both measured relative to the surface normal. The spectra have been corrected for the analyzer transmission factor and normalized to the height of elastically scattered peaks. The inset show the details of π-π* loss feature. The left panel shows how the π-π* loss intensity decreases during sputtering, the right panel shows how it recovers upon annealing.

The incidence and emission angles were θ_i=0° and θ_e=40°, respectively, both measured relative to the surface normal. The spectra have been corrected for the analyzer transmission factor and normalized to the height of elastically scattered peaks. As already mentioned, the loss feature at about 6 eV is due to π-π* transition whereas the wide and intense structure at ~26 eV is commonly attributed to $\sigma + \pi$ plasmon excitations involving all valence electrons. In the insets, the enlarged portions of the REELS curves are depicted to highlight the evolution of the π loss structure. To better illustrate the dramatic changes of the π loss peak a simple linear background was substracted and the resulting integrated peak intensity $I_{\pi-\pi^*}$ was then normalized to that of the elastic peak I_0, taken by doubling the spectral area on the negative loss side. The so normalized π-π* loss transition

probability $\mu_{\pi-\pi^*} = I_{\pi-\pi^*} / I_0$, together with its energy position $E_{\pi-\pi^*}$ is plotted in fig.8 as a function of Φ_{N_2} and annealing temperature for two emission angles of θ_e=40° and 80°. As can be seen, upon irradiation, the π-plasma excitation rate decreases monotonically with Φ_{N_2} and its transition energy continuously shifts to lower values for $\Phi_{N_2} \leq 4.6x10^{14} ions/cm^2$ and then levels off afterwards.

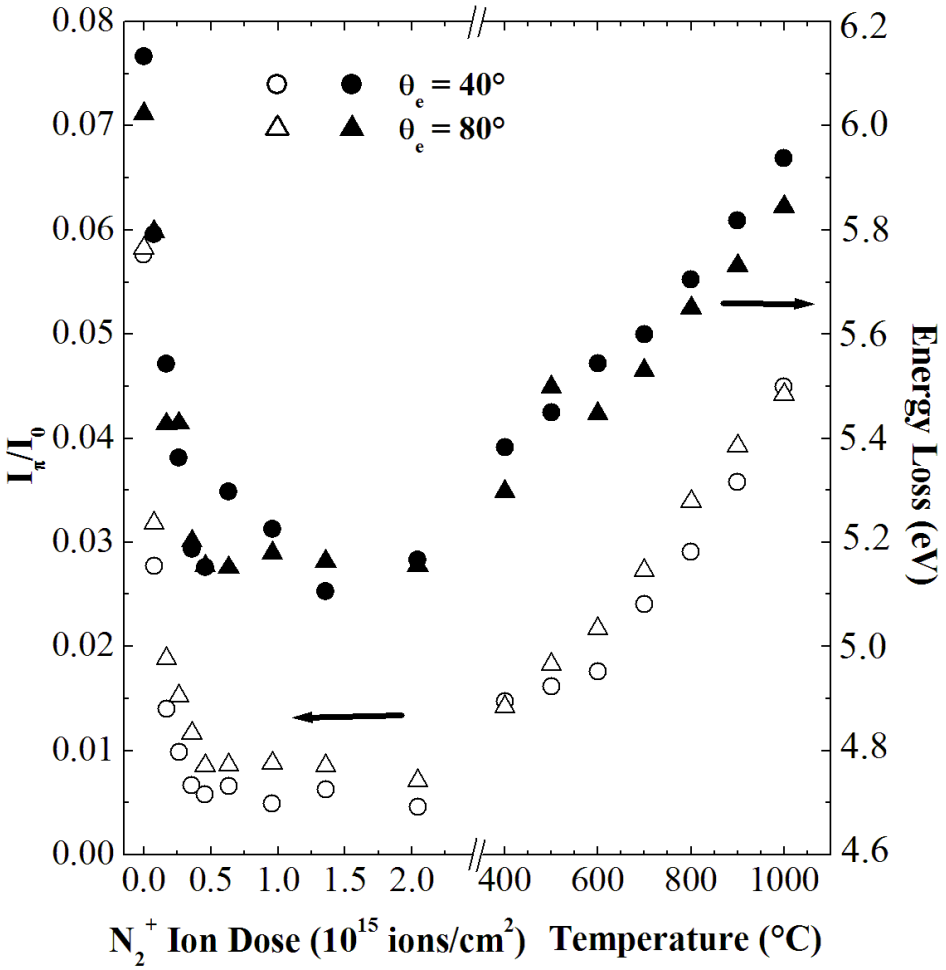

Fig.8 π-π* transition energy and probability as a function of N_2^+ ion dose and annealing temperature.

With respect to the pristine SWNTs, the π-π* loss intensity is decreased by a factor of 11 and its transition energy reduces from 6.1 to 5.2 eV. Annealing produces a gradual increase in its intensity and in $E_{\pi-\pi^*}$. It is interesting to note that even after annealing to the highest temperature of

T=1000°C, its transition probability is still much less than that for untreated SWNT sample, though the nitrogen atomic concentration is reduced to only about 1-2 percent.

2. Discussing XPS data

In discussing nitrogen doping of SWCNTs through N_2^+ ion irradiation, two fundamental and intrinsicly correlated issues will be addressed: bombardment induced structure damage and N-C chemical bonding. The consequent modifications to the system electronic properties will be also discussed.

It is well known that during approaching to the target surface the incoming N_2^+ ions can undergo a charge exchange process and will most probably be neutralized via a resonant or Auger neutralization mechanism [2]. These nitrogen molecules then will likely be collisionally dissociated at the surface into two N atoms, each of them carries about half of the primary kinetic energy, which means about 150 eV. Heavy particle impact on SWCNTs can produce point defects such as vacancies and adatoms due to momentum transfer in knock-on N-C collisions. The threshold displacement energy has been estimated to be about 20-25 eV [3]. Moreover, physical and chemical sputtering can also be responsible for the loss of C atoms in the surface region [4]. In an atomistic simulation of low energy and low fluence irradiation on SWCNTs, Krasheninnikov and Nordlund showed that a 150 eV Ne^+ ion can create one or two single atomic vacancies in a nanotube [5]. Such vacancies on small diameter nanotubes are metastable and can reconstruct forming pentagons to saturate or partially saturate the dangling bonds [6-8]. The C atoms knocked out in a primary collision can leave the surface as a sputtered particle or remain attached to the tube as an adatom. Such C atoms can also migrate through the nanotube to annihilate other vacancies or to be bond in a place quite far away from their original sites [9]. Because of the low primary energy used in this study the average number of defects produced by C recoils in secondary and cascade collisions is expected to be small [10]. For SWCNT bundles it is also possible to create inter-tube links through covalent bonds mediated by carbon recoils [11].

Irradiation using nitrogen particles can create similar structural defects in SWCNTs as noble gas particles do. However its high chemical reactivity makes probable the trapping of nitrogen in the created vacancies. Indeed, because of the very similar masses a large energy and momentum transfer from a projectile N particle to a target C atom is likely. A schematic representation of possible N-C bonding configurations is given in fig.9. With $C^{-\alpha}N^{+\beta}$ it is meant that α carbon atoms are removed and β nitrogen atoms are added. After knocking off a carbon atom, if the kinetic energy of the impinging nitrogen particle is small enough, it can replace the C atom inserting itself

in the three-fold coordinated hexagonal ring (a) or bond to two C atoms (b) but this later bonding is expected to be unstable and should readily transform to the former one.

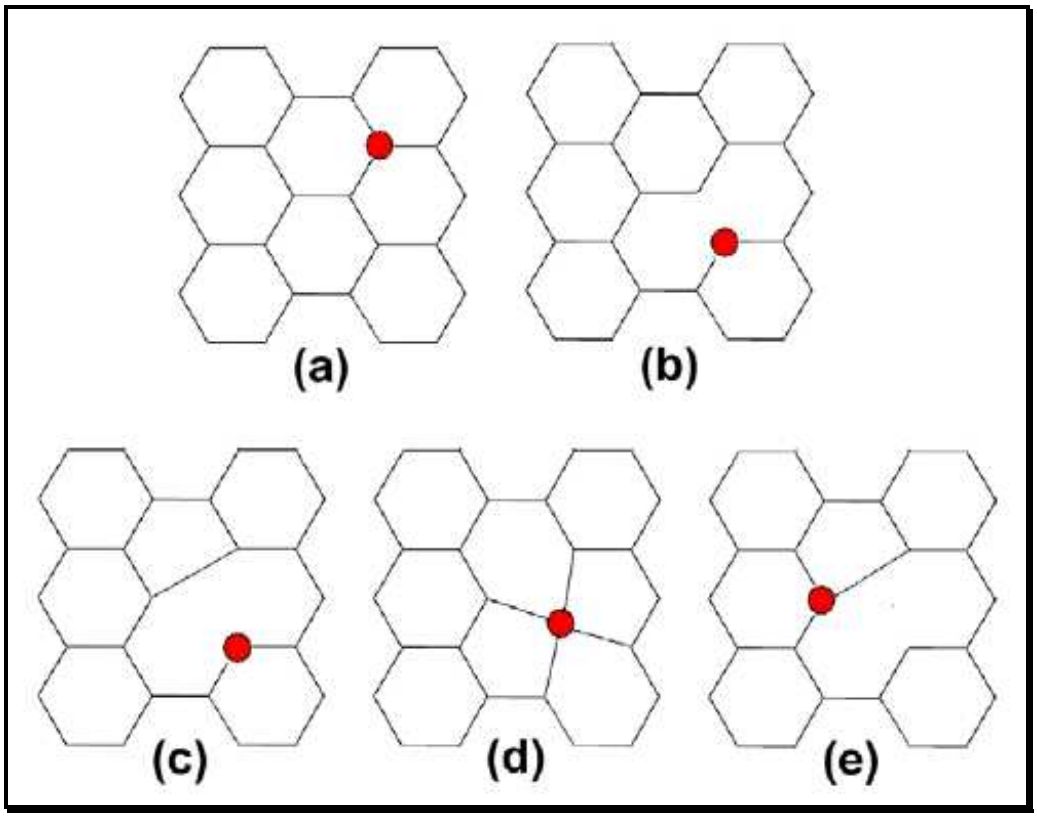

Fig.9 Schematic representation of possible N-C bonding configurations with a nitrogen dopant atom inserted in a graphitic network : a) substitutional N-3sp^2C $C^{-1}N^1$; b) pyridne like N-2sp^2C $C^{-1}N^1$; c) pyridine like N-2sp^2C $C^{-2}N^1$; d) N-4sp^3C $C^{-2}N^1$; e) N-3sp^3C $C^{-2}N^1$.

Even if the projectile N is not captured in the original vacancy, it can migrate in the nanotube network and finally be trapped in some other vacancy sites [12]. A double or multiple vacancy can also be created in one or two separated collision sequences and if a N atom is trapped there it will link to two sp^2 C atoms forming a pyridine-like bonding (c) or can connect to four or three sp^3 C atoms (d-e). Of course a nitrogen impurity atom can also be present in the SWCNT bundles as an interstitial or bind to the inner wall of a nanotube as an adatom. The most stable configuration is the bridge-like one in which N is bonded to two sp^3 C atoms [12]. Srivastava et al. showed that nitrogen atoms may be chemisorbed on the reconstructed vacancy sites [13].

In the last 15 years a great effort has been put in identifying the chemical composition of carbon nitride films grown with a variety of techniques and of nitrogen ion irradiated graphite, amorphous carbon and fullerene films in a tentative to synthesize superhard β-C^3N^4. Nevertheless, the N

bonding character is nowadays still a controversial issues of long lasting debate. Marton et al. proposed a two phase model: small C^3N^4-like crystallites with tetrahedral sp^3 bondings (P_1) are embedded in a graphite-like sp^2 bonded CN_x regions (BE = 400.0 eV) [14]. This scheme has been widely adopted in subsequent studies. Ripalda et al. argued that the introduction of a third component (P_2) in a position intermediate between P_1 and P_3 can somehow explain the otherwise abnormal peak shifts in CN_x films after annealing and renders the fitting more rational [15]. They suggested to attribute P_1 to atoms linked to two C neighbours in a sp^2 pyridine-like configuration, P_2 to metastable ion beam induced defects and P_3 to N atoms substitutionally incorporated in sp^2 hexagonal C rings. These assignments were later supported by a polarization dependent near-edge x-ray absorption fine structure study [16] but also were criticized by Zheng et al. [17]. Based on theoretical calculations [18], they confirmed P_1 to have a tetrahedral sp^3 character and proposed P_2 to be a pyridine-like sp^2 bonding and P_3 to be substitutional sp^2 in a graphene network. Peaks P_4 and P_5 at high binding energies are commonly attributed to N-O bondings, though some studies suggested that they may originate from molecular N_2 [19].

For nitrogen doped carbon nanotubes the experimental N1s core level photoelectron emission spectra reported in literature are essentially the same as those for CN_x : two main peaks at 398.0-398.6 eV and 400-401 eV which correspond to P_1 and P_3 in fig.4, respectively. Sometimes a third intermediate component (P_2) has been observed. Two main identification schemes exist in literature. The first is based on the binding energy calculations performed by Souto et al. and by Johansson and Staftroem who assigned P_1 to nitrogen atoms tetrahedrally bonded to three sp^3 hybridized C atoms, P_2 to those linked to two sp^2 C neighbours at the edges of a graphene sheet, and P_3 to substitutionally threefold coordinated nitrogen in the aromatic ring network [20,18]. This can be regarded as an extension of the two phase model originally proposed by Marton et al. [14] for CN_x or as a replica of the assignments suggested by Zheng et al. [17]. The second well adopted scheme is based on the Hartree-Fock self-consistent-field calculations performed by Casanovas et al. [21] for a planar graphene structure which identifies the peak at BE = 398.5 eV as due to twofold coordinated nitrogen atoms in pyridine-like sites and that at BE = 400.5-402.5 eV as substitutional graphite-like N.

As can be clearly seen in fig.4, annealing of N-SWCNTs to high temperatures produced a dominant N1s peak at 400.5 eV. In agreement with nearly all previous theoretical and experimental studies, P_3 has been assigned to nitrogen atoms substitutionally bonded to three carbon neighbours in a sp^2 hexagonal graphene network. This is consistent with the theoretical calculations that show the single substitutional defect to have the lowest formation energy [12] and is also supported by the

atomistic simulations of Kotakoski et al. who evidenced the dominance of the threefold N sp^2 bonding configuration for low energy ion irradiation in SWCNTs and its stability and increasing prevalence upon annealing [3]. However, in their simulations they totally ignored the possible cumulative effects of ion bombardment.

In this study peak P_1 is assigned to N atoms bonded either to four sp^3 C in the center of a reconstructed vacancy site formed by two pentagonal and two hexagonal rings (d in fig.10) or bonded to three sp^3 C atoms in the vertex of a pentagon, a hexagon and a nine-member ring (e). Peak P_2 is assigned to N atoms linked to two sp^2 C in a pyridine-like structure (c and marginally b). These structures are created by knocking out two C atoms and localizing one N in such vacancy sites. This scheme of assignment is essentially in agreement with those proposed by Souto et al. [20] and by Johansson and Staftroem [18] and is consistent with the fact that the relative abundance of both P_1 and P_2 rises when ion fluence increases. It indicates a larger concentration of vacancy defects in the nanotube network and a consequently higher probability for divacancy creation. The reduction of R_{P_2} for N content larger than 9% may be due to the increasing defect-defect (vacancy-vacancy) interactions which may render instable the configuration like that shown in fig.9c, thus its transformation into those of (d) and (e). The drastic intensity drop of P_2 upon first annealing at 400°C is mainly related to the high mobility of carbon adatoms which can efficiently diffuse in the nanotube and recombine with vacancies in the pyridine-like sites (c) or sp^3 bonding states (e) to transform them into perfect substitutional trigonal bondings (a) or just a simple bond bridging between N and C in the pyridine site (b) causing a corresponding rise of the absolute intensity of P_3. Of course, heating can weaken and eventually break the N-C bonds leading to a loss of nitrogen dopants, especially for those in the energetically less stable non substitutional sites. Moreover, it can be noticed that the interstitial bridge bonding to two sp^3 C is not consistent with the results shown in fig.4. Indeed, the probability for a nitrogen particle to become an interstitial should be constant for scattering from perfect nanotube, but is expected to gradually decrease if scattered in an increasingly defective network because of a larger opportunity for a nitrogen atom to recombine with an existing vacancy, in clear contrast to the observed behaviour of P_1 and P_2. The other bonding configurations with two or more nitrogen atoms located in the same (closed or opened) ring are not very likely for low N content, especially for the present case of forced nitrogen incorporation. At this point it is interesting to underline the basic differences between these real experiments and the simulations performed by Kotakoski et al [3]. These authors simulated the statistical effect of a single impact of a free standing single (10,10) nanotube. They did not take into account the case of more SWCNTs (bundles), thus the possibility that a scattered projectile N or recoil C atom can interact with a second nanotube to create more defects. More importantly, they

totally ignored the cumulative effects of ion irradiation induced defect production. In fact, in a subsequent collision sequence it is much easier to knock out a carbon atom (with dangling bonds) in a vacancy site and create a double or multiple vacancies. Their simulation should be regarded as a limiting case at very low ion fluence. Finally, the incident direction is completely random in the SWCNT bucky paper sample. Interestingly, though a quite large portion of nitrogen atoms are bonded in pyridine and other defective sites, linear extrapolation to $\Phi_{N_2} = 0$ would indicate an intensity ratio of substitutional P_3 to defective P_1 and P_2 of about 4:3. This means that if the N-O contribution is ignored, the threefold N sp^2 bonding fraction is very close to 60% predicted by the simulations [3]. Annealing the sample to high temperatures certainly reduces the number of defects. The increasing mobility of C interstitials and adatoms facilitates their diffusion in the nanotube network, thus their recombination with vacancies. As a result, the intensity of peak P_2 associated to pyridine-like bonding decreases rapidly with T: it is reduced to less than half of the original value for T=400°C and is no longer visible for T ≥ 700°C. A substantial portion is converted to the threefold graphitic bonding (P_3). With increasing heating temperature, there is a general loss of N species in the probing region due to both to the diffusion into the bulk and to the sublimation from the surface. These results are in very good agreement with an early study of Hoffman et al. on 500 eV N_2^+ implantation into graphite. These authors also found a similar intensity behaviour of the three main nitrogen peaks for post-irradiation annealing to 300 and 500°C [22].

Taylor et al. in an early thermal desorption study on CN_x films observed the emission of N and CN as the sample was heated and found that all N containing species are expelled at about 1200°C [23]. After heating to temperature of 1000°C the substitutionally configuration is virtually the only N bonding environment. This result may provide a practical guidance for obtaining good quality N-SWCNTs. It must also be noticed that due to the limitation of the experimental conditions (very low beam current density and long spectrum acquisition time) oxigen incorporation in N-SWCNTs was unavoidable. However, annealing to high temperature can substantially reduce the oxygen content, as evidenced in fig.4. As regarding the nitrogen spatial distribution, it is interesting to note that the concentration profile shown in fig.3 is in quite good agreement with the simulated distribution profile of defects for 500 eV Ar^+ bombardment on SWCNT bundles [11], though, strictly speaking, a direct comparison is not correct because the distribution of dopant location sites does not take into account vacancy and C adatom defects. It is worthwhile to note that high resolution TEM images of individual SWCNT bundles under 30 eV N^+ irradiation reported by Yamamoto et al. [24] showed that for an ion fluence of up to $1.7x10^{15} ions/cm^2$ the NT bundles suffered some damages but their tube structure remained essentially unchanged. The reported experimentals results are in agreement with such observations. Incorporation of 11% nitrogen atoms must imply the presence of CNT

network defects and structural deformation. However, as evidenced in the SEM image, the sample was not made amorphous and these damages can be somehow recovered with heating. The defects and disorder created by ion irradiation sensitively affect the original optimal p_z-p_z orbital overlap and lead to a narrowing of the π-π^* pseudo band gap causing a shift in the plasma energy loss $E_{\pi-\pi^*}$ to lower values [2]. On the other hand, the progressive loss of the long range order of the conjugated π orbital coupling results in a dramatic decrease of the collective oscillation intensity $\mu_{\pi-\pi^*}$. The extra electron of N atoms may also partially fill the anti-bonding π^* bands reducing the π-π^* transition probability [25]. The effects of annealing on reordering the graphene structure, saturating the dangling bonds and reducing defects, are also readly seen in REELS of fig.8. The intensity of π-π^* plasmon loss grows steadly and the transition energy increases continuously with temperature. Previously, a combined XPS and electron energy loss spectroscopy (EELS) study on 3 keV N_2^+ doping into SWCNTs has been reported [26]. A similar curve fitting scheme was found to be very successful for the N1s core spectra. However, as expected, the relative abundance of various components is significantly different. Indeed, the P_1 to P_3 intensity ratio for nitrogen concentration of about 10% is close to 3 for E_p = 3 keV while it is only 1.3 for E_p = 0.3 keV indicating a greater damage of the nanotube network, thus a smaller portion of perfect substitutional nitrogen doping for higher irradiation energy.

All these results provide further support to the description given above on the N_2^+ interaction with SWCNTs and the discussion regarding the nitrogen chemical bonding nature. Finally it must be mentioned that C1s core level emission spectra all exhibit an asymmetric broadenig at higher binding energy side with the maxima slightly shifted about 0.1-0.2 eV to larger values. Detailed line shape analysis is complicated by the presence of a large number of possible C bonding configurations and the quite small separation between these components. A tentative of curve deconvolution is shown in fig.10. For clean SWCNTs it is visible that the C1s spectrum is quite asymmetric and can not be fitted with one single Gaussian component, thus the whole EDC has been taken, after being opportunely broadened (convolution with a Gaussian function of FWHM = 0.85-1.2 eV), to represent contribution of the undoped portion of the sample in N-SWCNTs (marked as C0). The fitting indicates the presence of two well distinguished peaks C1 and C3 at 287.0 and 285.6 eV, respectively, together with a small peak C4 at 289.0 eV related to C-O. The contribution given by the structures C1 and C3 are attributed to C atoms bonded in a sp^3 tetrahedral geometry and to N atoms in a sp^2 graphitic network, respectively. A broader structure (FWHM=4.2 eV) at about 290.8 eV is adequately subtracted from C0 to account for the reduction of plasma loss intensity.

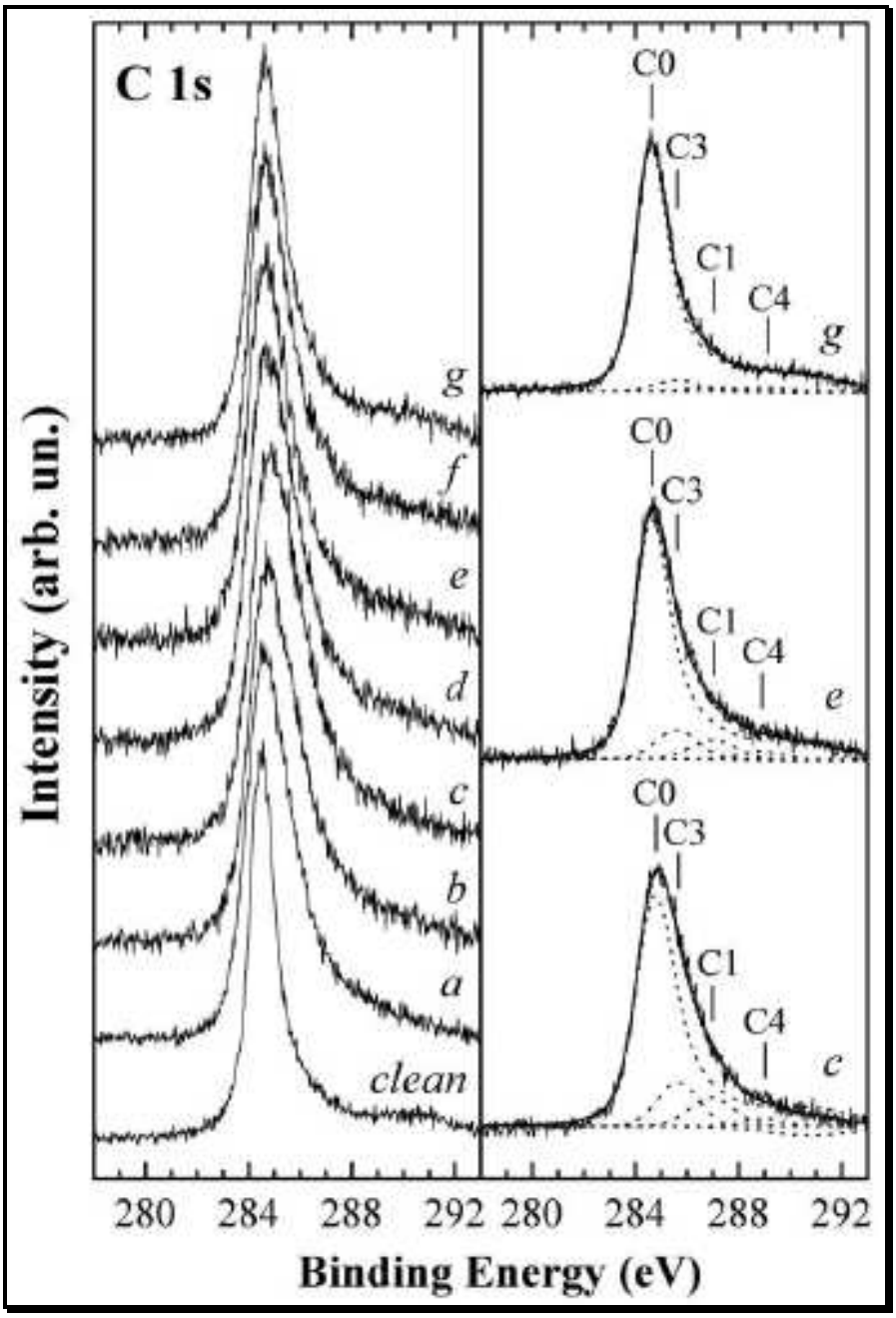

Fig.10 Left panel: Background subtracted and normalized N 1s core level X-ray photoemission spectra for 3 keV N_2^+ ion irradiated SWNT with a flux of $\Phi = 1 \times 10^{15}$ (curve a), 2×10^{15} (b), and 4×10^{15} ions/cm^2 (c) and subsequent annealing for 20 min each at $T = 650$ (d), 800 (e), 1000 (f), and 1200 K (g). Right panel: Fittings with a set of gaussian curves. See text for peak assignment.

References

[1] C. Palacio, C. Gomez-Aleixandre, D. Diaz, and M.M. Garcia, Vacuum 48, 709 (1997).

[2] H.J. Steffen, C.D. Roux, D. Marton, and J.W. Rabalais, Phys. Rev. B 44, 3981 (1991).

[3] J. Kotakoski, A.V. Krasheninnikov, Yuchen Ma, A.S. Foster, K. Nordlund and R.M. Nieminen, Phys. Rev. B 71, 205408 (2005).

[4] P. Hammer and W. Gissler, Diam. Rel. Mater. 5, 1152 (1996).

[5] A.V. Krasheninnikov and K. Nordlund, Nucl. Instr. and Meth. in Phys. Res. B 216, 355 (2004).

[6] J. Kotakoski, A.V. Krasheninnikov, and K. Nordlund, Phys. Rev. B 74, 245420 (2006).

[7] S. Berber and A. Oshiyama, Physica B 272, 376 (2006).

[8] C. Wang and C. Y. Wang, Eur. Phys. J. B 54, 243 (2006).

[9] A.V. Krasheninnikov, K. Nordlund, P.O. Lehtinen, A.S. Foster, A. Ayuela, and R.M. Nieminen, Phys. Rev. B 69, 073402 (2004).

[10] K. Nordlund, J. Keinonen, and T. Matilla, Phys. Rev. Lett. 77, 699 (1996).

[11] E. Salonen, A.V. Krasheninnikov, and K. Nordlund, Nucl. Instr. and Meth. in Phys. Res. B 193, 603 (2002).

[12] Y. Ma, A.S. Foster, A.V. Krasheninnikov, and R.M. Nieminen, Phys. Rev. B 72, 205416 (2005).

[13] D. Srivastava, M. Menon, C. Daraio, S. Jin, B. Sadanadan, and A.M. Rao, Phys. Rev B 69, 1553414 (2004).

[14] D. Marton, K.J. Boyd, A.H. Al-Bayati, S.S. Todorov, and J.W. Rabalais, Phys. Rev. Lett. 73, 118 (1994).

[15] J.M. Ripalda, I. Montero, L. Galan, Diam. Rel. Mater. 71, 402 (1998).

[16] I. Shimoyama, G.Wu, T. Sekiguchi, and Y. Baba, Phys. Rev. B 62, R6053 (2000).

[17] W.T. Zheng, Y. Sakamoto, J.H. Gao, X.T. Li, P.J. Cao, Z.S. Jin, and M. Takaya, Phys. Rev. B 64, 016201 (2001).

[18] A. Johansson and S. Staftroem, J. Chem. Phys. 111, 3203 (1999).

[19] P.Hammer, N.M. Victoria, and F. Alvarez, J. Vac. Sci. Technol. A 18, 2277 (2000).

[20] S. Souto, M. Pickholz, M.C. dos Santos, and F. Alvarez, Phys. Rev. B 57, 2536 (1998).

[21] J. Casanovas, J.M. Ricart, J. Rubio, F. Illas, and J.M. Jimenez-Mateos, J. Am. Chem. Soc. 118, 8071 (1996).

[22] A. Hoffman, I. Gousman, and R. Brener, Appl. Phys. Lett. 64, 845 (1994).

[23] J.A. Taylor, G.M. Lancaster, and J.W. Rabalais, J. Am. Chem. Soc. 100, 4441 (1978).

[24] K. Yamamoto, T. Kamimura, and K. Matsumoto, Jap. J. Appl. Phys. 44, 1611 (2005).
[25] M.C. dos Santos and F. Alvarez, Phys. Rev. B 58, 13918 (1998).
[26] F. Xu, M. Minniti, C. Giallombardo, A. Cupolillo, P. Barone, A. Oliva, and L. Papagno, Surf. Sci. 601, 2819 (2007).

Chapter 3

Nanopatterning by ion erosion

1. Theory of sputtering

The fabrication of regular nanostructures on the nanometer length scale is nowadays gaining a lot of interest due to their numerous possible technological applications in many different fields. As an example they are highly required in optoelectronics, biological optics and in the data storage industry, to create high density magnetic media [1,2]. Moreover, they can be used as templates for the deposition of thin films or heteroepitaxial growth of quantum dots and wires [3-5]. Generally there are two possible approaches for the fabrication of nanostructures [6]. The first is the top-down technique which consists in lithografic patterning by optical sources with a wavelength much smaller than the visible light. This technique is usually very time consuming and does not permit large scale production since costs are very high. The second is the bottom-up approach, which is based on self-organization processes. Among the methods which relie on it, the most promising is the low energy ion beam erosion of solid surfaces. Usually known as sputtering [7-12], it is a very widespread method in surface science. It is used for depth profiling, surface analysis, sputter cleaning, deposition and, not less important, production of well-ordered nano-scale topographies on surfaces. These kinds of topographies are originated by self-organization processes, which can

result in ripples (wave-like shaped structures) or dots [13]. The great advantage of ion erosion methods is the possibility to produce large-area nanostructured surfaces in a single step and with very reduced costs. Moreover, sputtering parameters can be easily changed leading to a change in nanostructrures' properties. On the contrary, among the disadvantages there is a less effective control of the shape of produced patterns.

To clarify the physical basis of the processes which rule the formation of such nanopatterns it is fundamental to deep understand what usually happens on a surface during ion irradiation. Indeed, the bombardment of solid targets with energetic particles can give rise to many different processes. Incident ions can be backscattered or implanted into the target, and many particles like atoms, electrons and photons can be emitted from it. Moreover, an ion penetrating a solid will undergo many collisions with target atoms, transferring them its kinetic energy and momentum. This may lead to displacement of atoms with consequent creation of lattice defects like vacancies and interstitials. When target atoms receive enough kinetic energy they will induce additional collisions with other target atoms and so additional atomic displacements. This process is known as 'collision cascade' [14,15]. In case of small number of atoms placed in motion and isotropic distribution of the collision density the process is called 'linear collision cascade'. The cascade is described in terms of binary collisions between moving ions and stationary atoms. When target atoms travelling towards the surface (due to momentum reversal) gain enough energy, they can overcome the surface binding energy barrier and be emitted in vacuum. This process will lead to material erosion (sputtering). Incident ions can loose their kinetic energy in both elastic (nuclear collisions) and inelastic (electronic excitation) processes. However, for the low energy range ion energy loss is mainly due to nuclear collision processes, which determine the energy deposition and the range of ions in the target. The amount of ion energy deposited by an ion and the ion range depend on the material properties and the ion mass and energy. Furthermore, the increasing number of ions will induce additional defects in the crystalline structure which may lead to surface amorphization in case of high defect density. The erosion rate of a surface under ion bombardment is determined by the sputtering yield Y, defined as the average number of atoms leaving the surface of a solid per incident particle [14,16,17]. Most of the sputtered atoms come from the surface. However, the scattering events take place within a certain layer of average depth a which is the average energy deposition depth. Usually the number of sputtered atoms is orders of magnitude smaller than the total number of atoms participating in the collision cascade. A well accepted description of ion sputtering has been developed by Sigmund [16,17]. He derived a set of transport equations describing the energy transfer during the sputtering process in case of amorphous targets. In Sigmund's theory of sputtering the rate at which material is sputtered from a point on an arbitrary

surface $z = h(x,y)$ is proportional to the power deposited there by the random slowing down of ions. The average energy deposited at a point $\mathbf{r} = (x,y,z)$ in the solid by an ion which travels along the z-axis until striking the surface has the following Gaussian distribution:

$$E(\bar{r}) = \frac{\varepsilon}{(2\pi)^{3/2}\sigma\mu^2}\exp\left(-\frac{(z-h(0,0)+a)^2}{2\sigma^2}-\frac{(x^2+y^2)^2}{2\mu^2}\right) \qquad (1)$$

In eq. (1) ε indicates the total energy carried by the ion and σ and μ are the widths of the distribution in the directions parallel and perpendicular to the incoming ion beam, respectively. A schematic illustration of the ion energy distribution is shown in fig.1.

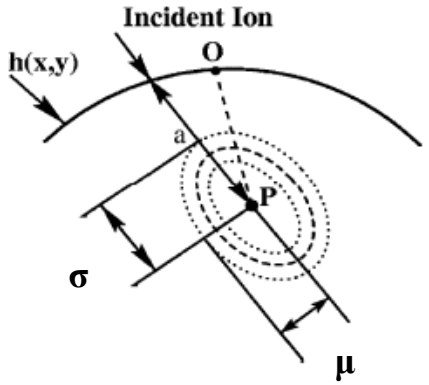

Fig.1 Schematic illustration of the energy distributed by an incident ion. While the collision process induced by an ion is rather complex, according to Sigmund it can be reduced to the following effective process: the ion penetrates the bulk of the material and stops at point P, where all its kinetic energy is released and spread out to the neighbouring sites following a Gaussian form with widths σ and μ.

Several Monte Carlo simulations of the sputtering process have shown that the deposited energy distribution can be well approximated by a Gaussian function for intermediate and high energies [18]. The mean energy deposition depth of an ion traveling inside the bulk is usually comparable to the penetration depth and is proportional to the ion energy according to this relation:

$$a(\varepsilon) = \frac{1-m}{2m}\gamma^{m-1}\frac{\varepsilon^{2m}}{NC_m} \qquad (2)$$

N represents the target atomic density, γ is equal to $\frac{4M_1M_2}{(M_1+M_2)^2}$ (M_1, M_2 are the mass of ion and target atom, respectively), C_m is a constant dependent on the interatomic potential and the exponent $m = m(\varepsilon)$ varies from $m = 1$ at high energies to $m \sim 0$ at low energies. For intermediate energies (10-100 keV) $m \sim ½$ and the energy deposition depth becomes $a\ (\varepsilon) \sim \varepsilon$. Eq. (1) describes what happens in case of a single ion hitting the solid. Actually the sample is irradiated by an uniform flux f of bombarding ions, which penetrate the solid at different points simultaneously. For such reason the erosion velocity at an arbitrary point O depends on the total power given by all the ions entering within the range of the distribution (1). The normal erosion velocity at a point O is calculated as [17]:

$$v_O = p\int_Q \Phi(\bar{r})E(\bar{r})d\bar{r} \qquad (3)$$

The integral is calculated over the region Q of all points at which the deposited energy contributes to the total power. $\Phi(\mathbf{r})$ is a local correction to the uniform flux f due to the variation of the local slopes, and p is a constant which depends on the material, according to binding energy and scattering cross-section:

$$p = \frac{3}{4\pi^2}\frac{1}{NU_0C_0} \qquad (4)$$

U_0 is the surface binding energy and C_0 a constant proportional to the square of the effective radius of the interatomic potential. Eq. (3) is only valid when shadowing effects and redeposition of sputtered material are ignored. Sigmund's theory offers a very detailed description of ion bombardment but it is not able to provide direct information about the morphology of ion sputtered surfaces. The equation for the erosion velocity in the given form can not be used to make analytical predictions about the dynamical properties of surface evolution, which is the aim of this dissertation.

2. Continuum models

The first and rather successful model able to explain the evolution of surface morphology under ion irradiation with subsequent ripple formation on it has been proposed by Bradley and Harper (BH model) in 1988 [13]. Starting from Sigmund's theory of sputtering, they demonstrated for the first time that the dependence of the sputtering yield on the surface curvature induces an instability which leads to the formation of periodically modulated structures. Many theoretical studies about

surface erosion by ion irradiation consider the sputtering yield independent from the local curvature of the surface. Nevertheless, such assumption is a good approximation only if the radius of curvature at an arbitrary point on the surface is much larger than the ion range. Bradley and Harper notified that it is impossible to predict the formation of wave-like structures on a surface without considering such effect. To determine the dependence of the sputtering yield on the curvature, they calculated from eq. (3) the normal component of the surface velocity $v(\Phi,R)$ at a point O when an uniform flux f is incident at angle Φ, measured relative to the z-axis. They treated the system as a two dimensional one, but this does not affect the result since it can be easily generalized to the three dimensional case. Moreover, they assumed that the surface height $h(x)$ varies slowly enough that R, the radius of curvature at point O, is much larger than the ion range a. The final result obtained from the calculation has the form:

$$v(\phi,R) \approx \frac{\Lambda \varepsilon f a}{\sqrt{2\pi}\sigma\mu} B_1^{-1/2} \exp\left(-\frac{a^2}{2\sigma^2}+\frac{A^2}{2B_1}\right)\left[\cos\phi+\Gamma_1(\phi)\frac{a}{R}\right] \qquad (5)$$

where

$$\Gamma_1(\phi) \equiv \frac{A}{B_1}\sin\phi - \frac{B_2}{2B_1}\left(1+\frac{A^2}{B_1}\right)\cos\phi - \frac{AC}{B_1^2}\left(3+\frac{A^2}{B_1}\right)\cos\phi \qquad (6)$$

Λ is a constant of proportionality relating the power deposited at O to the rate of erosion there, and the coefficients A, B_1, B_2 and C depend on the parameters σ, μ and the angle ϕ. Considering first the limit of a flat surface (R=∞), the yield results to be equal to:

$$Y_0(\phi) = \frac{N v(\phi, R=\infty)}{f\cos\phi} \qquad (7)$$

and it is shown to be an increasing function of the incident angle ϕ, which is a reliable result except of course for cases of grazing incidence where the model is not valid anymore. Eq. (5) contains the dependence of the sputtering yield on the surface curvature. The coefficient of a/R, Γ_1, is negative for $\phi = 0$. This means that when the ion beam is normally incident on a periodic disturbance, the valleys are eroded more rapidly than the crests, being the radius of curvature R negative in a valley. The result is that sputtering increases the amplitude of the perturbation and so leads to an instability and roughening of the surface. The process is well understandable looking at fig.2.

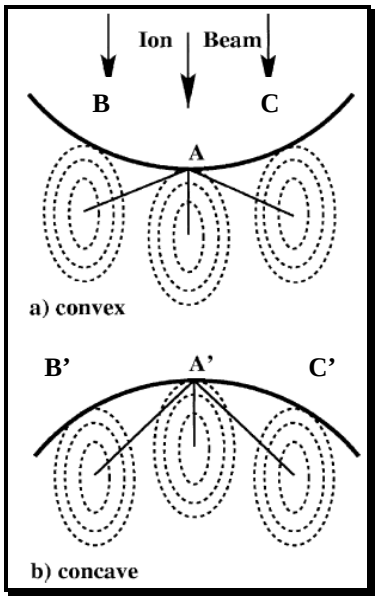

Fig.2 Schematic illustration of the physical origin of the instability during ion erosion of nonplanar surfaces. A surface element with convex geometry (a) is eroded faster than that with a concave geometry (b), due to the smaller distances (solid lines) the energy has to travel from the impact point to the surface (A or A′ points).

The energy deposited at the point A by ions hitting the surface at A is the same as that deposited at A' by ions hitting the surface there. However, the average energy deposited at A by an ion which hits the suface at B is higher than that deposited at A' by an ion incident at B' and the same is for C and C'. This leads to a rate of erosion higher in A compared to A'. Starting from the equation for the erosion velocity generalized for three dimentional systems and combining the smoothing effect due to thermally activated surface diffusion, Bradley and Harper derived a linear equation for the surface morphology evolution under ion sputtering [13] :

$$\partial_t h = -v_0(\vartheta) + v_0'(\vartheta)\partial_x h + S_x(\vartheta)\partial_x^2 h + S_y(\vartheta)\partial_y^2 h - K\nabla^4 h \qquad (8)$$

This equation describes the temporal evolution of the surface height $h(x,y,t)$ during sputtering under an incident angle ϑ considered respect to the normal of the initial flat surface. The coordinate system axis x and y lie parallel and perpendicular to the projection of the ion beam on the surface, respectively. The general meaning of this equation is the competition between two mechanisms: the roughening of the surface, due to the curvature dependent sputtering yield, and smoothing effects for thermal diffusion of target atoms. The first term on the right side represents the angle dependent erosion velocity of a flat surface. The second term is related to the lateral movement of the

structures on the surface. These first two terms do not affect the characteristics of the final topography (wavelength and amplitude). The third and fourth terms describe the curvature dependent erosion rate and are responsible for the roughening of the surface while the last one is the contribution of surface relaxation due to material transport on the surface. The two coefficients S_x and S_y depend on the ion energy, ion incident angle and material properties:

$$S_{x,y} = \frac{fa}{N} Y_0(\vartheta)\Gamma_{1,2}(\vartheta) \tag{9}$$

The two coefficients $\Gamma_{1,2}(\vartheta)$ account for the local variation of the sputtering yield and are equal to:

$$\Gamma_1(\vartheta) \text{ (see eq. 6)}$$

$$\Gamma_2(\vartheta) = -\frac{\mu^2}{a^2}\left(\frac{1}{2}B^2 + \frac{AC}{B_1}\right)\cos\vartheta \tag{10}$$

They depend on the ion incident angle and on the parameters which characterize the distribution of the deposited energy. They can be calculated using the SRIM code [18]. The coefficient K describes the thermally activated surface diffusion related with material transport on the surface:

$$K = \frac{D_s \gamma \Omega^2 n}{K_B T}\exp\left(\frac{-\Delta E}{K_B T}\right) \tag{11}$$

Here D_s is the surface diffusion constant, γ the surface free energy per unit area, Ω the atomic volume, n the number of atoms per unit area on the surface, ΔE the activation energy for surface diffusion, K_B the Boltzmann constant and T the surface temperature. Only by adding a smoothing term it is possible to predict the formation of ripple structures on the surface; the roughening terms alone are not enough. To practically see how the periodic solution comes out it is useful to take the Fourier transform of eq. (8), with $\mathbf{q} \equiv (q_x, q_y)$ the wave vector. Eq. (8) becomes:

$$\frac{dh(q_x, q_y, t)}{dt} = [-S_x q_x^2 - S_y q_y^2 - K(q_x^4 + q_y^4)]h(q_x, q_y, t) \tag{12}$$

The solution of such equation is:

$$h(q_x, q_y, t) = h(q_x, q_y, 0)\exp[r(q)t] \qquad (13)$$

where $h(q_x,q_y,0)$ is the initial amplitude spectrum of the Fourier component with growth factor:

$$r(q_x, q_y) = -S_x q_x^2 - S_y q_y^2 - K(q_x^4 + q_y^4) \qquad (14)$$

Eq.(13) describes the time evolution of the amplitude of the Fourier components and it increases exponentially for positive $r(q)$ values. According to the sign of the growth factor, the surface can roughen or smoothen. The function $r(q)$ has a maximum at $q^* = (\max|S_{x,y}|/2K)^{1/2}$, where $\max|S_{x,y}|$ is the largest in absolute value between $-S_x$ and $-S_y$. The diffusion coefficient K is always positive, so that the sign of $r(q)$ depends on the coefficients S_x and S_y, which means on the parameters $\Gamma_1(\vartheta)$ and $\Gamma_2(\vartheta)$. The amplitude with wavenumber q^* will growth faster than the others, resulting in a periodicity with wavenumber q^* which will dominate the surface topography. The corresponding wavelength of ripples can be written as:

$$\lambda = \frac{2\pi}{q_{x,y}} = 2\pi\left(\frac{2K}{\max|S_{x,y}|}\right)^{1/2} \qquad (15)$$

The direction of the wavevector of the periodicities depends on the values of S_x and S_y. The model can actually predict the dependence of the wavelenghts λ_x, λ_y on the ion incidence angle. An example for the case $\sigma = a/2$, $\mu = \sigma/2$ is shown in fig.3 [13] :

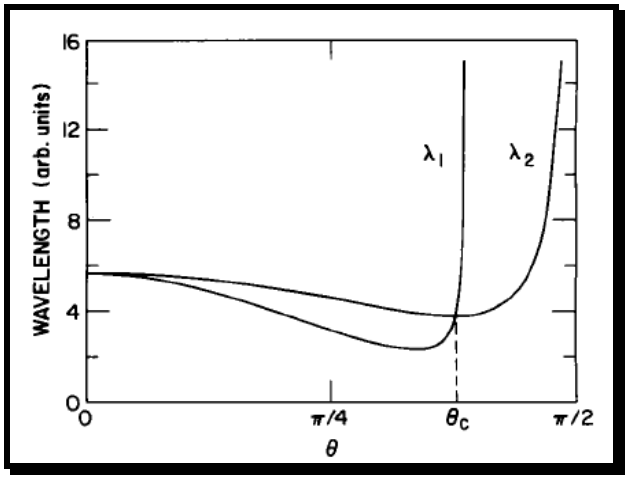

Fig.3 Plot of λ_1 and λ_2 vs ϑ for σ = a/2 and μ = α/2. The ripple wavelength is in the *x* direction for $0 < \vartheta < \vartheta_c$ and in the *y* direction for $\vartheta_c < \vartheta < \pi/2$.

As it is described in the plot the ripple wavevector is parallel to the projection of the ion beam on the surface (x-axis) when the incident angle ϑ is not too large, more precisely when it is smaller than a critical angle ϑ_c. In this case the absolute value of q_x is higher than q_y, so $\lambda_x < \lambda_y$. The wavevector is perpendicular to the beam direction when the ions hit the surface close to grazing incidence. For normal incidence, $\Gamma_1(\vartheta)$ is equal to $\Gamma_2(\vartheta)$ and the direction of the selected wavevector is arbitrary. In this case several ripple orientations will be selected by surface imperfections and a grid of hillocks and depressions will result on the surface, which is in agreement with what observed in experiments. It is possible to derive by simple calculations the dependence of the ripple wavelength λ on some sputtering parameters:

- λ decreases with increasing ion energy according to the relation $\lambda \approx \frac{1}{E^{1/2}}$;

- λ is a decreasing function of the ion flux of the form $\lambda \approx \frac{1}{J^{1/2}}$;

- λ does not depend on the ion fluence.

BH model does not take into account any other possible smoothing process except thermal diffusion. Nevertheless this mechanism is active on the surface and becomes the dominating relaxation process only at high temperatures. To exlain ripple formation at low temperature it is necessary to consider other smoothing effects. Makeev et al. [19] introduced the ion-induced effective surface diffusion (EDS) as the main relaxation mechanism at low temperatures. It does not imply a real mass transport along the surface, but it is based on preferential erosion of the target during the ion beam sputtering. Considering the EDS term as the main smoothing term eq.(8) becomes:

$$\partial_t h = -v_0 + v_0' \partial_x h + S_x \partial_x^2 h + s_y \partial_y^2 h - D_{xy} \partial_x^2 \partial_y^2 h - D_{xx} \partial_x^4 h - D_{yy} \partial_y^4 h \qquad (16)$$

The three coefficients D_{xy}, D_{xx}, D_{yy} depend on the parameters which determine the distribution of the deposited energy, ion flux and incidence angle. In this case:

$$\lambda = \frac{2\pi}{q_{x,y}} = 2\pi \left(\frac{2D_{xx,yy}}{\max|S_{x,y}|} \right)^{1/2} \qquad (17)$$

- and λ is increasing with ion energy: $\lambda \approx a \approx E^{2m}$;

- λ is independent from the ion flux and fluence.

Another relaxation mechanism which can contribute to surface smoothing is the ion-induced viscous flow (IVF) [20,21], which is related to material transport along the surface and depends on the concentration of defects created during the cascade. In this case the wavelength is independent from the ion flux and fluence and is increasing with the ion energy: $\lambda \approx E^{3m}$.

BH model was very successful in explaining the mechanism which leads to ripple formation as well as their amplitude, wavelength and orientation respect to the ion beam direction, in good agreement with experimental results. Nevertheless, theirs is a linear model unable to explain the long term behaviour of the surface evolution (like the appearence of kinetic roughening [22]) and to describe the stochastic nature of the sputtering process. For example, according to the linear model the ripple amplitude should increase exponentially in time, but in experiments amplitude saturation has always been observed to saturate [23]. The addition of non linear terms, which are terms depending on higher order powers of the surface height or its derivatives, can have the effect of modifying the long term behaviour of the surface evolution. Cuerno et al. [24,25] calculated non linear terms in the BH model by expanding the basic sputtering mechanism to include higher order effects. Performing the integral of the normal erosion velocity at a generic point *O* of the surface, they derived the equation of motion for the height profile:

$$\partial_t h(x,y,t) \cong -v(\varphi, R_x, R_y)\sqrt{1+(\nabla h)^2} \qquad (18)$$

where φ is the angle of the beam direction with the local normal to the surface at $h(x,y)$ and R_x, R_y the radii of curvature at *O*. To take into account the stochastic arrival of ions on the surface a Gaussian white noise $\eta(x,y,t)$ with zero mean has been added into the equation, as well as a term to describe the surface diffusion. Expanding eq.(18) they obtained an anisotropic noisy Kuramoto-Sivashinsky equation (AKS) :

$$\partial_t h = -v_0 + v_0'\partial_x h + S_x\partial_x^2 h + S_y\partial_y^2 h + \frac{\ell_x}{2}(\partial_x h)^2 + \frac{\ell_y}{2}(\partial_y h)^2 - D\nabla^4 h + \eta(x,y,t) \qquad (19)$$

The coefficients of the non linear terms, ℓ_x and ℓ_y, depend on the ion beam parameters and energy distribution parameters a, σ, μ. They describe the tilt-dependent erosion rate, proportional to the ratio between ion flux and penetration depth f/a. ℓ_y is negative for all incidence angles, ℓ_x can have both positive and negative values. Unlike the linear expression, the non linear surface evolution equation can not be solved analitically, but it can be calculated numerically. Integration of such equation has been perfomed by Park et al. [26]. They showed that for short sputtering times

the non linear effects are negligible and the system evolution is well described by the linear instability mechanism. However, after a crossover time, which depends on the coefficients of eq.(19), the surface morphology is completely determined by the non linear terms. Two cases can be distinguished according to the signs of ℓ_x and ℓ_y. For $\ell_x \cdot \ell_y > 0$ the non linear terms destroy the ripple morphology and lead to kinetic roughening. In case of $\ell_x \cdot \ell_y < 0$, ripple formation is followed by a long transient rough regime which ends in a new morphology of rotated ripples. The crossover time τ can be written as:

$$\tau \cong \frac{4D}{S_{\max}^2} \ln\left(\frac{S_{\max}}{\ell_{\max} A_0}\right) \qquad (20)$$

where A_0 is the initial amplitude (at $t = 0$) of the dominant mode and $\ell_{\max}$ is in the same direction of $S_{\max}$. The amplitude at the crossover time is predicted to be proportional to the ratio $S_{\max} / \ell_{\max}$. In fig.4a the calculated time dependence of the surface width, which is proportional to the ripple amplitude, is shown. It is defined as $W^2(L,t) \equiv \frac{1}{L^2} \sum_{x,y} h^2(x,y,t) - \bar{h}^2$.

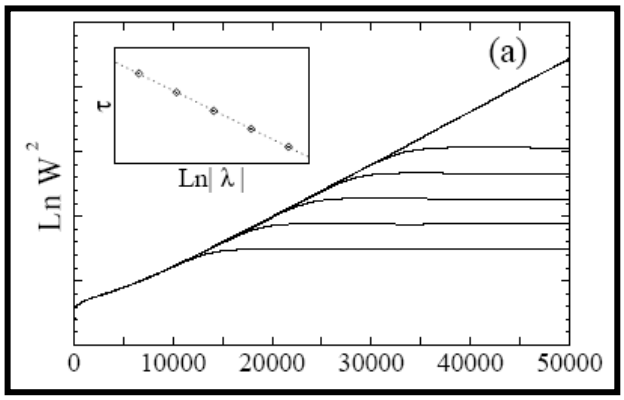

Fig.4a Time evolution of the surface width W^2 for different values of λ. From the top to the bottom, the curves correspond to λ =0, -10^{-5}, -10^{-4}, -10^{-3} -10^{-2},-10^{-1}, respectively. Inset: the cross over time τ is shown as a function of ln(λ).

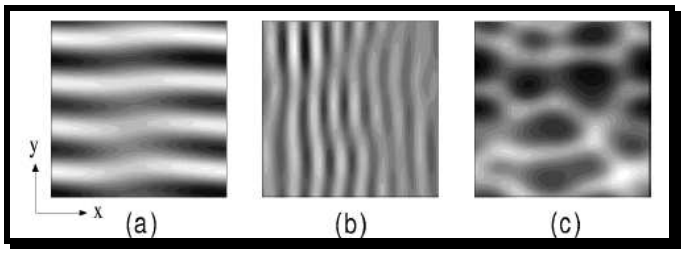

Fig.4b Grey scale plot for a surface 64x64.The KS equation predicts the wavelenght $l_y = 16$ (a), $l_x = 8$ (b). (c) surface configuration at a calculated time $t = 5 \times 10^5$.

For $t < \tau$ the width W increases exponentially, which is consistent with the prediction of the linear model. In this regime ripple wavelength and orientation are also correctly described by the linear theory. Beyond the crossover time the non linear terms become effective and as a consequence the surface width immediately stabilizes. Moreover, the ripple pattern generated in the linear regime disappears and the surface exhibits kinetic roughening. An example of this transition is shown in fig4b. The presence of kinetic roughening implies an increase of the surface width either

logarithmically (when $\ell = 0$) or as power law (when $\ell \neq 0$). However, compared with the exponential increase in the linear regime, this dependence is not visible in fig.4a. The time evolution of the surface width in case of $\ell_x \cdot \ell_y < 0$ is shown in fig.5a. Three different regimes characterize the dynamics of the surface. In regime I ripples form on it.

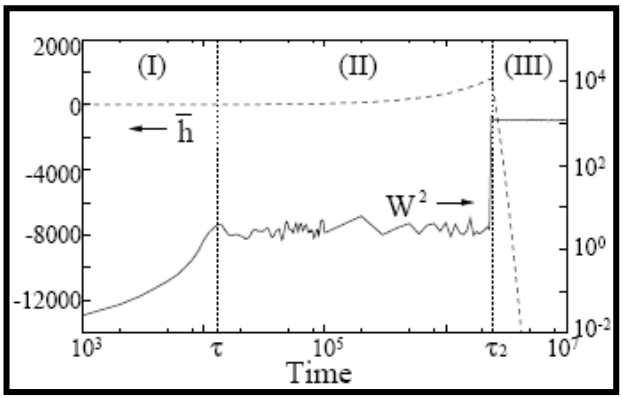

Fig.5a Time evolution of the mean height (dashed line) and the surface width (solid line). The dotted lines separate the three regimes discussed in the text.

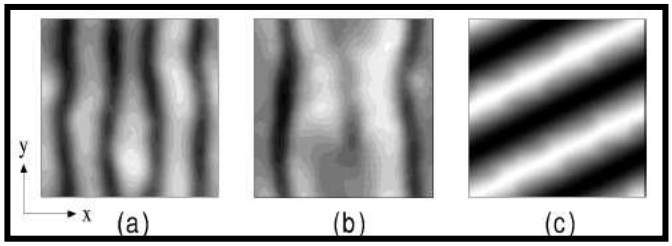

Fig.5b Grey scale plot of a surface of size 64x64, showing the surface morphologies at t = 10^4 in regime I (a), t = $2x10^5$ in regime II (b), t = 10^7 in regime III (c).

Their wavelength and orientation are correctly described by the linear theory and the surface width increases accordingly exponentially. After the first crossover time τ_1 the system enters a long transient regime in which the surface width is stabilized and the ripples disappear, as it shown in fig5b. In this second phase the surface is rough, without any spatial order. The third regime is characterized by a new kind of ripples which appear after a second crossover time τ_2. These ripples are rotated with an angle θ_c respect to the *x* direction. The angle θ_c can be calculated as:

$$\theta_c = \tan^{-1} \sqrt{-\frac{\ell_x}{\ell_y}} \qquad (21)$$

For $t > \tau_2$ the width suddenly increases and then stabilizes in regime III. Moreover it is interesting to notice that the amplitude of the rotated ripples is much larger than those in regime I.

The anisotropic generalization of the Kuramoto-Sivashinky equation has been very successful in predicting some of the non linear effects observed in experiments of ripple formation, but still presents some limitations. For example, it is not able to predict the possibility of a time-dependent behaviour of the typical pattern length scale. The increase of the ripple wavelength in time is known as coarsening. It has actually been observed many times in experiments [27-30], but models

introduced so far can not take it into account. Recently a new model for ion beam sputtering (IBS) ripple formation at off-normal incidence has been proposed by Garcia-Castro-Cuerno (GCC model) [31-33]. It is called 'hydrodynamic model' since it is based on the hydrodynamic description of pattern formation in aeolian sand dunes and ion sputtered systems. Starting from this general model, a single height equation in which coefficients can be related to experimental parameters has been derived. This equation contains both the AKS equation and the hydrodynamic theory and generalizes those obtained by previous continuum models. Moreover it is able to predict many experimental features of pattern formation by IBS at oblique incidence, like transverse ripple motion with non-uniform velocity, onset of kinetic roughening and ripple coarsening. The authors consider two coupled fields: the thickness of the mobile surface adatoms layer, $R(\boldsymbol{x},t)$, and the height of the bombarded surface, $h(\boldsymbol{x},t)$. Their time evolution is written as:

$$\partial_t R = (1-\phi)\Gamma_{ex} - \Gamma_{ad} + D\nabla^2 R \tag{22}$$

$$\partial_t h = -\Gamma_{ex} + \Gamma_{ad} \tag{23}$$

where Γ_{ex} and Γ_{ad} are the rates of atom excavation from and addition to the immobile bulk, $(1-\phi) = \bar{\phi}$ measures the fraction of eroded atoms that becomes mobile, and $D\nabla^2 R$ describes the motion of mobile atoms along the surface due to isotropic thermal diffusion. D is constant for amorphous materials. Even in case of all eroded atoms sputtered away (ϕ = 1), there is always a non-zero average fraction of mobile atoms, R_{eq}. The main difference between this model and previous ones is that in the present model not all the near-surface atoms which break their bonds with the surface will be eroded, but most of them will be redeposited locally, giving raise to an implicit viscous flow in the amorphized layer through the evolution of R. Combining the two equations (22) and (23) it is possible to derive an equation for the surface height (24):

$$\partial_t h = \gamma \partial_x h + \sum_{i=x,y} \left\{ -S_{i_i} \partial_i^2 h + \ell_i^{(1)} (\partial_i h)^2 + \Omega_i \partial_i^2 \partial_x h + \xi_i (\partial_x h)(\partial_i^2 h) \right\} + \sum_{i,j=x,y} \left\{ -\mathrm{K}_{i,j} \partial_i^2 \partial_j^2 h + \ell_{i,j}^{(2)} \partial_i^2 (\partial_j h)^2 \right\}$$

It is basically a generalized AKS equation but with the presence of new non linear terms with coefficients $\ell_{i,j}^{(2)}$, which depend on the fraction of eroded atoms that become mobile and are able to induce much richer pattern dynamics. Numerical integrations of such equation show that in the linear regime all the features predicted by the BH model are reproduced. Entering the non linear regime the main role is played by the second non linearities. The first non linearities $\ell_{i,j}^{(1)}$ always

lead to the saturation of the pattern with constant wavelength and amplitude. Pattern coarsening requires the presence of $\ell_{i,j}^{(2)}$. When the values of these coefficients increase compared to $\ell_{i,j}^{(1)}$, the coasening process is longer and the saturation values of the pattern wavelength also increase. The coarsening exponent *n* of the power law growth has a value which is larger the later the coarsening stops. This is shown in fig.6a where the calculated time dependences of the ripple wavelength for different values of the ratio between the second and the first non linearities *r* are plotted [33].

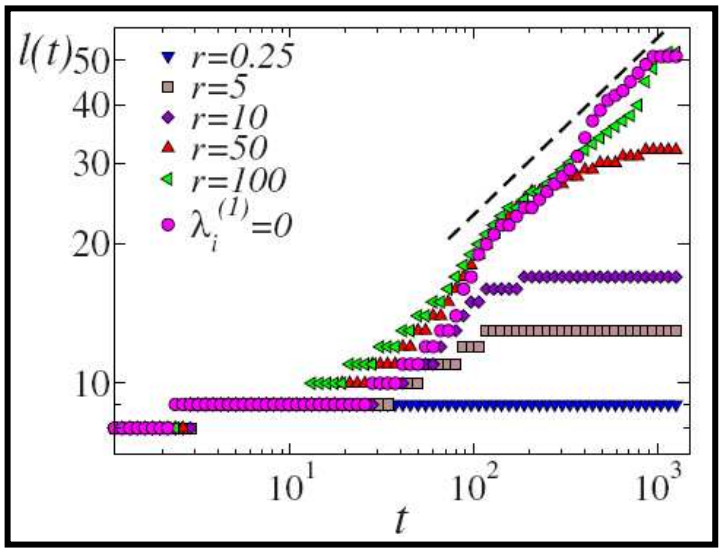

Fig.6a Temporal evolution of the pattern wavelength as calculated by the GCC model. The dashed line shows the fit to a power law for r =100 where $\ell \sim t^{0.38}$

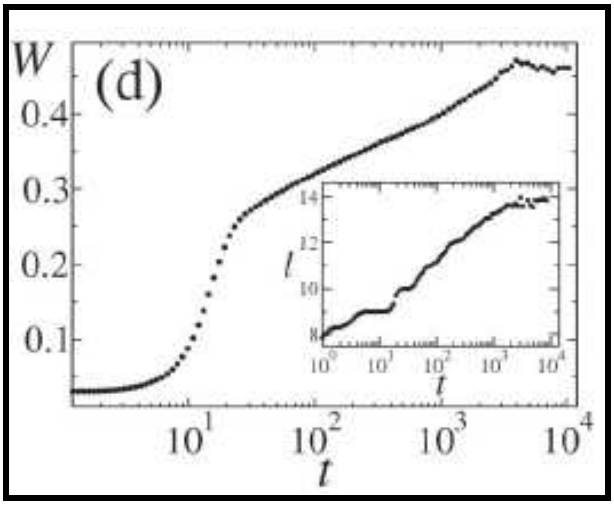

Fig.6b Surface roughness and lateral wavelength (inset) calculated in case of marginal coarsening.

Experiments in which ripple coarsening is absent or residual would correspond to small $\ell_{i,j}^{(2)}$ values. An example is shown in fig.6b, where ripple wavelength varies slowly in time with $\lambda(t) \sim log(t)$. Time evolution of surface roughness W(*t*) has also been evaluated. In general the roughness increases exponentially in the linear instability regime. Then the non linearities stabilize the system and induce slower growth for the roughness, till when a time independent value is reached. For very small values of the ratio *r* this stationary state is reached earlier and the intermediate power law growth regime is shorter. For larger values of *r* this intermediate phase is longer and can be well fitted by a power law function $W(t) \sim t^{\beta}$. Moreover the morphology appears to be more disordered (higher values of roughness) for smaller *r*. The temporal evolution of W(*t*) for different *r* is shown in fig.7 [33].

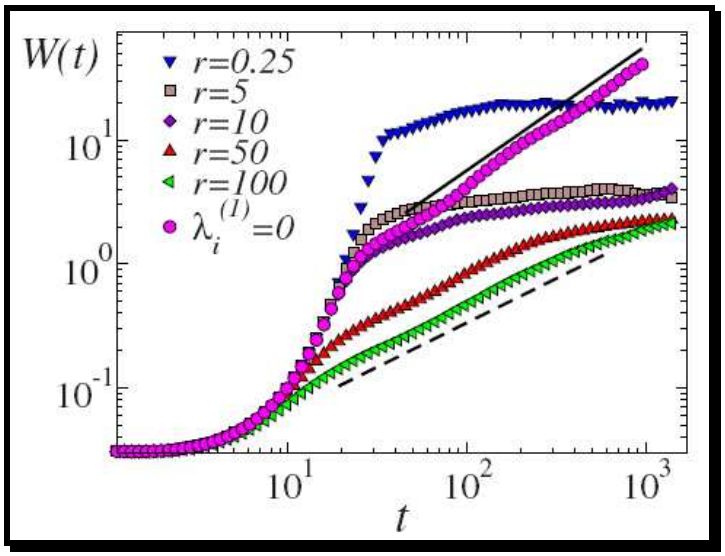

Fig.7 Temporal evolution of the global roughness as calculated by the GCC model. The solid and dashed lines show the fit to power laws for $\lambda_i^{(1)} = 0$ and r = 100 where $W \sim t^{1.00}$ and $W \sim t^{0.71}$, respectively.

The GCC model is nowadays the most complete theory among the ones proposed so far about IBS ripple formation, since it can account for many non linear effects which take place on the surface during ion irradiation. Systematic experimental results are strongly encouraged to test its validity.

References

[1] C. A. Ross, Annu. Rev. Mater. Res. 31, 203 (2001).

[2] B. D. Terris, T. Thomson, and G. Hu, Microsyst. Technol. (2006).

[3] G. A. Prinz, Science 282, 1660 (1998).

[4] M. A. Reed, C. Zhou, C. J. Muller, T. P. Burgin, and J. M. Tour, Science 278, 252 (1997).

[5] L. P. Lee and R. Szema, Science 310, 1148 (2005).

[6] B. Ziberi, Ph.D. Thesis, Ion Beam Induced Pattern Formation on Si and Ge Surfaces, University of Leipzig (2006).

[7] P. Sigmund, J. Mater. Sci. 8, 1545 (1973).

[8] R. Kelly, A. Oliva, Nucl. Instr. and Meth. in Phys. Res. B 13, 283 (1986).

[9] G. Falcone, Phys. Rev. B 33, 5054 (1986).

[10] P. Sigmund and A. Oliva, Alloy sputtering at high fluence: Preferential sputtering and competing effects, http://www.osti.gov/energycitations/servlets/purl/10141417-EsXvVB/native/ (1992).
[11] G. Falcone, Rivista del Nuovo Cimento 13, 1 (1990).
[12] G. Falcone and A. Oliva, Appl. Phys. A 33, 175 (1984).
[13] R.M. Bradley and J.M.E. Harper, J. Vac. Sci. Technol. A 6, 2390 (1988).
[14] R. Behrisch, Sputtering by Particle Bombardment, Springer Verlag, Heidelberg (1981, 1983).
[15] H. Gnaser, Low-Energy Ion Irradiation of Solid Surfaces, Springer, Berlin (1999).
[16] P. Sigmund, Phys. Rev. 184, 383 (1969).
[17] P. Sigmund, J. Mat. Sci. 8, 1545 (1973).
[18] J. F. Ziegler, J. B. Biersack, and U. Littmark, The Stopping and Range of Ions in Solids, Pergamon, New York (1985).
[19] M. A. Makeev and A. L. Barabasi, Appl. Phys. Lett. 71, 2800 (1997).
[20] C. Herring, J. Appl. Phys. 21, 301 (1950).
[21] W. W. Mullins, J. Appl. Phys. 30, 77 (1959).
[22] S. Habenicht, W. Bolse, K. P. Lieb, K. Reimann, and U. Geyer, Phys. Rev. B 60, R2200 (1999).
[23] J. Erlebacher, M. J. Aziz, E. Chason, M. B. Sinclair, and J. A. Floro, Phys. Rev. Lett. 82, 2330 (1999).
[24] R. Cuerno and A. L. Barabasi, Phys. Rev. Lett. 74, 4746 (1995).
[25] R. Cuerno, H. A. Makse, S. Tomassone, S. T. Harrington, and H. E. Stanley, Phys. Rev. Lett. 75, 4464 (1995).
[26] S. Park, B. Kahng, H. Jeong, and A. L. Barabasi, Phys. Rev. Lett. 83, 3486 (1999).
[27] G. Carter and V. Vishnyakov, Phys. Rev. B 54, 17647 (1996).
[28] D.P. Datta and T.K. Chini, Phys. Rev. B 69, 235313 (2004).
[29] A.D. Brown and J. Erlebacher, Phys. Rev. B 72, 075350 (2005).
[30] A. Keller, S. Rossbach, S. Facsko, and W. Moeller, Nano. Techn. 19, 135303 (2008).
[31] M. Castro, R. Cuerno, L. Vazquez, and R. Gago, Phys. Rev. Lett. 94, 016102 (2005).
[32] J. Munoz-Garcia, M. Castro, and R. Cuerno. Phys. Rev. Lett. 96, 086101 (2006).
[33] J. Munoz-Garcia, R. Cuerno, M. Castro, Phys. Rev. B 78, 205408 (2008).

Chapter 4

Ripple and dot pattern formation on Ge surface

1. Nanoscale ripple coarsening on Ge

Ion beam sputtering of solid surfaces under oblique incidence is a very efficient tool for the fabrication of nanoscale ripples [1]. Nowadays this method is gaining increasing interest since such nanostructured surfaces may find numerous applications in nanotechnology [2-5]. Formation of periodic surface ripple patterns during ion beam sputtering with wavelength smaller than 100 nm has been observed on a large variety of materials including metals [6], insulators [7] and semiconductors [8]. Up to now intensive studies have been performed on Si surfaces [8-12] but only a few experiments report about ripple formation on Ge surfaces. Ripple patterns on Ge have been produced by low energy Xe^+ ion sputtering at both near-normal (5°-20°) and at 55° ion incidence [13-15]. Chason et al. investigated the temperature-dependent roughening kinetics of Ge surfaces during low energy (1 keV) Xe^+ sputtering at an incident angle of 55° [15]. The authors found that at 150°C (and below) the surface is amorphized by ion impact and roughens to a steady small value. At 250°C the surface remains crystalline, roughens exponentially with time and develops a pronounced ripple topography. At higher temperatures this exponential roughening was found to be slower. Ziberi et al. reported about ripple formation on Ge bombarded with 2000 eV Xe^+ ions at an

ion incidence angle of 5° with respect to the surface normal at room temperature [14]. Ripple patterns had a mean wavelength of 56 nm with the wavevector oriented parallel to the projection of the ion beam on the surface. Ripples showed a very high degree of order and their wavelength was independent from ion flux and fluence. However, the increasing of ripple wavelength with sputtering time, known as coarsening, has quite often been reported without being well understood up to date. Experimental data which demonstrate this effect are seemingly inconsistent showing very different time dependencies. A linear increase of the wavelength at increasing ion fluence was observed on Si(100) sputtered at 45° off-normal incidence by 40 keV Xe^+ ions at room temperature [8], whereas power law coarsening has been widely reported on semiconductors [9,12], insulators [16] and metals [6] in an angular range between 45° and 70°. Power law exponents were found to increase at increasing ion energy [16] or to decrease with sputtering time [9]. For example, sputtering of SiO_2 with Ar ions at 50° incidence leads to formation of ripples which coarsen in time [16]. The power law exponent *n* changes from 0.19 to 0.40 when the ion energy is doubled from 600 eV to 1200 eV. On Si for 60 keV Ar sputtering at 60° an exponent of 0.64 has been found [9]. This value decreases to 0.22 for long time irradiation. Moreover Si ripples show the same power law exponent (0.08) varying the Ar ion energy from 300 to 500 eV for sputtering at 67° [12]. On rippled Cu under 1 keV Ar^+ bombardment *n* decreases with the incident angle from a value of 0.26 (at 45°) to 0.13 (at 70°) [6]. During low energy Ar^+ ion sputtering of Si(111) surfaces at 60° incidence and at elevated temperatures (500-750°C) an exponential increase of the ripple wavelength with time was observed [11]. Very differently, for Si ripples produced under near-normal ion sputtering with Ar^+, Kr^+ and Xe^+ ions at room temperature no coarsening of the ripples was found [10]. The above cited results show that only more systematic experimental studies about ripple coarsening may provide a possible explanation for such a strong scattering in the reported experimental data and lead to a better understanding of the basic physical mechanism which govern this non-linear effect.

In this work the coarsening behaviour of ripple patterns on Ge surfaces during 500 eV Xe^+ ion beam erosion is presented for different incidence angles in the range from 61° to 68°. No clear pattern develops on the surface for sample irradiation at near-normal incidence up to ~50°. In the chosen angular range perodic ripples always form during ion sputtering, but show strong differences in the pattern evolution. Commercially available Ge(100) wafers with a specific resistance higher than 40 Ωcm and a root-mean-square (rms) roughness of 0.4 nm were sputtered at nominally room temperature without cooling using a broad 500 eV Xe^+ ion beam from a Kaufman ion source. The ion flux was kept constant at each angle and equal to $1.5x10^{14} ions/cm^2 s$. The ion fluence was varied from $2x10^{16} ions/cm^2$ to $2x10^{18} ions/cm^2$. The surface topography was investigated by ex-

situ Atomic Force Microscopy (AFM) in tapping mode. The Si tip used had a nominal radius smaller than 10 nm. Pattern wavelengths were determined from the fast Fourier transforms (FFT) of the AFM pictures. Examples of topographies emerging on Ge surfaces after low-energy ion beam erosion at three different angles around 65° for an ion fluence of $5x10^{17}\,ions/cm^2$ are presented in fig.1.

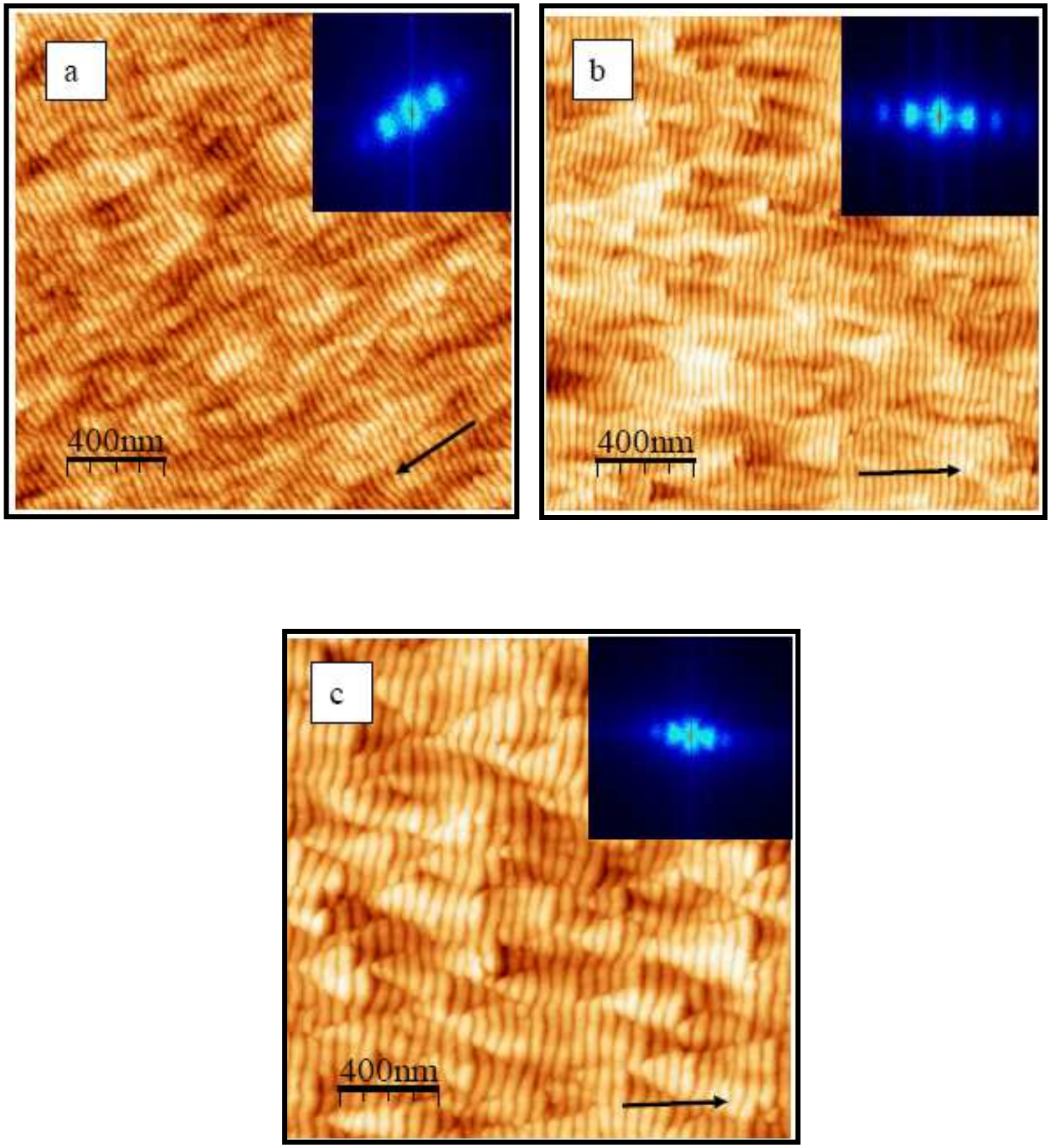

Fig.1 AFM images and relative FFT of Ge (100) surfaces sputtered by 500 eV Xe^+ ions at 61° a), 65° b), and 68° c), respectively. The fuence was fixed at $5x10^{17}$ ions/cm^2. Black arrows indicate the ion beam direction. Intensity scale are: 7 nm (a), 13 nm (b) and 22 nm (c), respectively. FFT images range from -100 to +100 μm^{-1}.

Well ordered ripple patterns with wavevectors oriented parallel to the ion beam projection are clearly visible in all cases, but they differ in both amplitude and periodicity. The 2-dimensional FFTs in the inset of each AFM image show side peaks that correspond to the dominating ripple wavelength. Ripples formed during sputtering at 61° have much smaller amplitude (saturation value ~ 0.7 nm) compared to those formed at 68° (saturation ~ 2.4 nm). Furthermore, the ripple wavelength is almost doubled by changing the sputtering angle by only three degrees from 65° to 68°. Fig.2 shows the dependence of the ripple wavelength on the ion fluence for different angles of incidence. Sputtering at 61° and 64° leads to a slight increase of the ripple periodicity in time without any clear saturation in the present range of fluence whereas a significantly different behaviour is observed for sputtering at 67° and 68°. In this case the value of l increases much faster in time until saturation is reached at a fluence of $5x10^{17}\,ions/cm^2$. Each set of data has been fitted with a power law function $l_\vartheta(\Phi) \propto \Phi^{n_\vartheta}$.

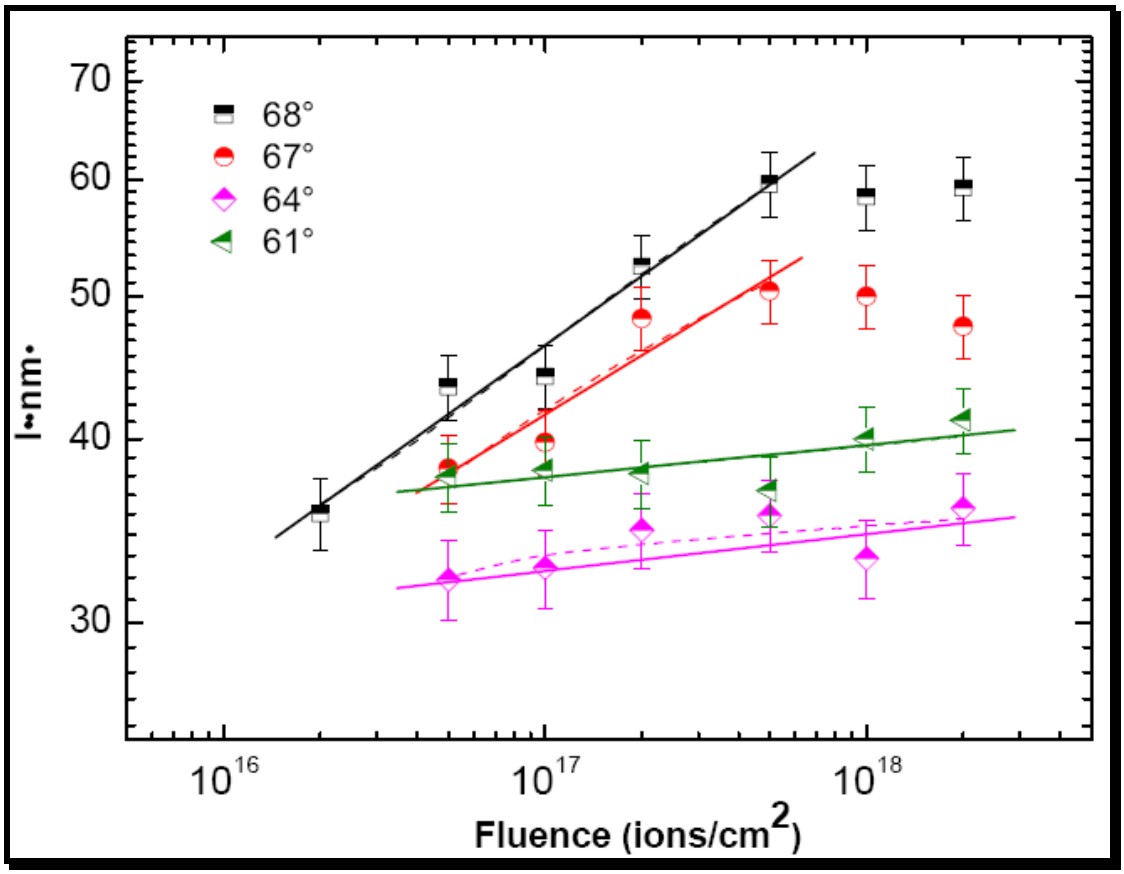

Fig.2 Time evolution of the ripple wavelength for four different sputtering angles. Solid lines represent power law and broken lines logarithmic fits, respectively.

The angular behaviour of the exponet n_ϑ is plotted in fig.3a. Its value is very low for sputtering in the angular range 61°-64°, but then it rapidly increases until it reaches a value of 0.16 ± 0.02 at 68°. However, since the values of the power law exponents still are rather small, the data could be fitted by logarithmic functions (dotted lines in fig.2) as well. In fig.3b the ripple wavelength as a function of the incidence angle is plotted. For each ion fluence shown, *l* has a similar dependence on the incidence angle. An initial slight decrease is followed by a rapid increase after a minimum is reached around 65°.

By comparing fig.2 and 3 two different regimes in the surface time evolution during ion sputtering can be identified. For angles lower than 65° the pattern wavelength undergoes only small variations at increasing incidence angle and ion fluence. At higher angles ripple coarsening is much stronger and the wavelength becomes a rapidly increasing function of the sputtering angle as well.

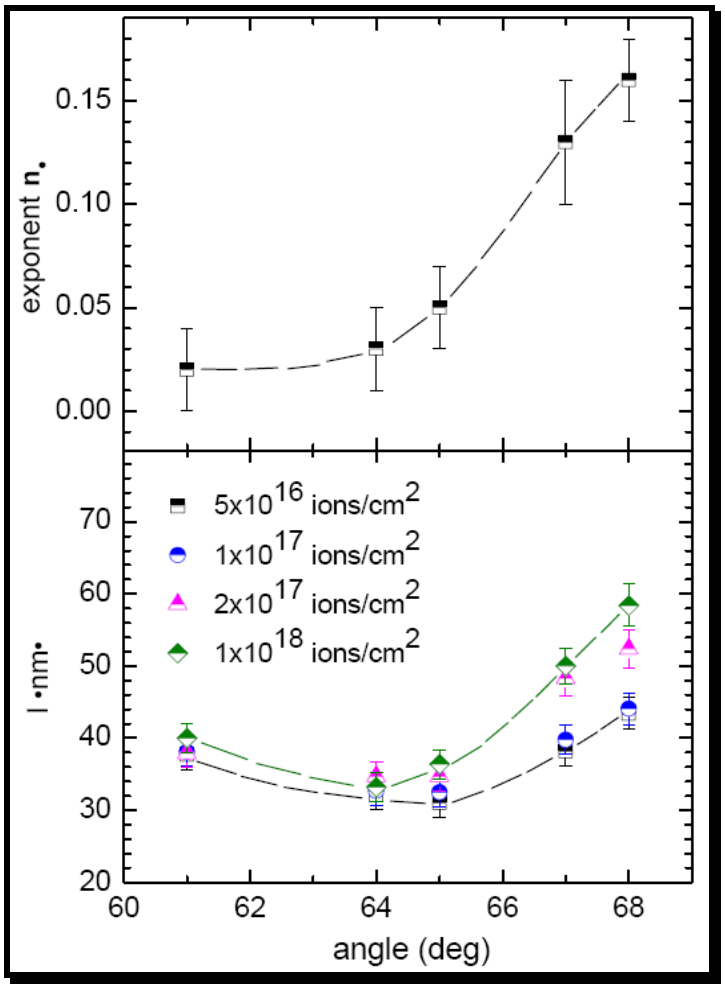

Fig.3 The exponent n_ϑ (upper panel) and the ripple wavelength (lower panel) as a function of the ion incidence angle. The ripple wavelength is shown for different values of ion fuences. Lines are drawn to guide the eye.

Finally, for a better understanding of the surface dynamics during ion sputtering, the time evolution of ripple amplitude and roughness for different incidence angles is shown in fig.4 a,b.

Ripple formation is generally understood in terms of a competition between roughening [17] and smoothing processes [7,18,19] which are active on the surface during sputtering. The BH linear model first [20] and the KS equation subsequently proposed do not succeed in predicting the experimentally observed increase of the ripple wavelength with ion fluence [21]. The only model which at present can account for this is the coupled two-field model by Garcia et al [22-24]. Starting from the hydrodynamic approach for aeolian sand dunes, they derived a continuum equation which contains two non-linear terms. The first non-linearity, which is already present in the KS equation, leads to pattern saturation with constant amplitude and wavelength. The second non-linearity, a conserved Kardar-Parisi-Zhang term (CKPZ), accounts for ripple coarsening.

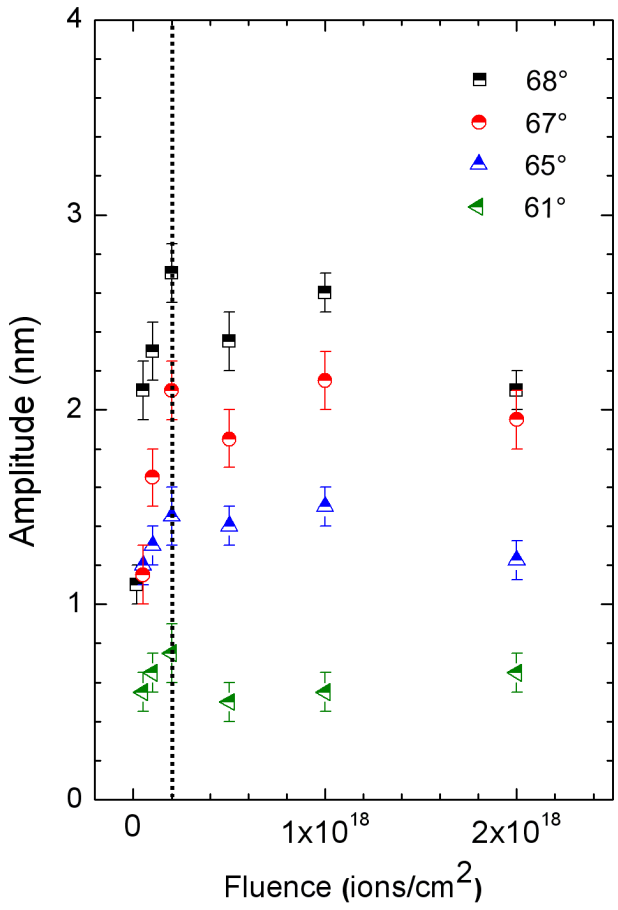

Fig.4a Ripple amplitude as a function of ion fluence for different sputtering angles.

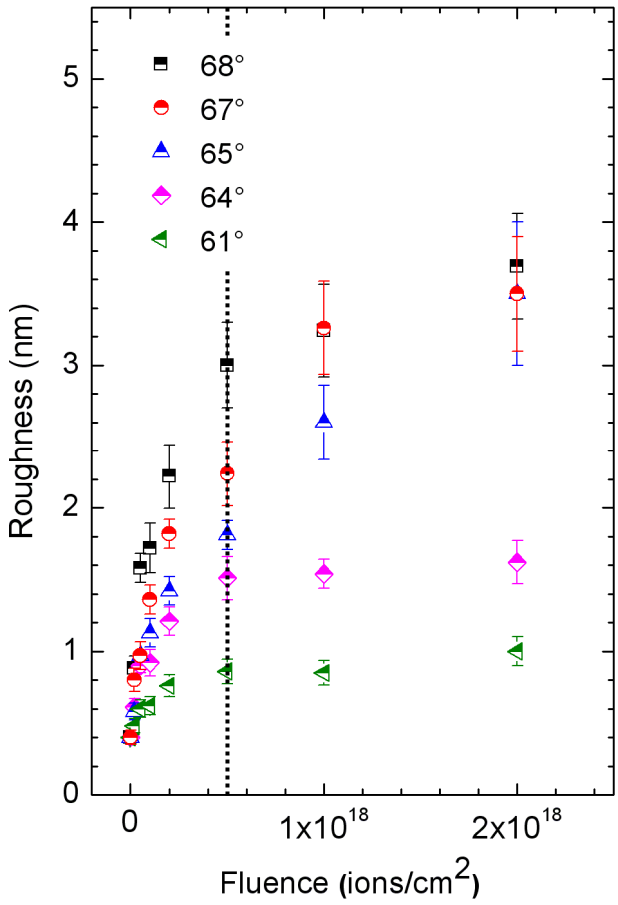

Fig.4b Surface roughness as a function of ion fluence for different sputtering angles.

In the framework of this new model the observed increase of the coarsening exponent and simultaneously of the ripple wavelength in the angular range from 64° to 68° has its origin in a corresponding change of the relative weight of the two non-linear terms at increasing incidence angles [23,24]. However, according to the model, coarsening should stop later when the value of *n* increases. This is in contrast with what has been experimentally observed. In case of marginal coarsening no clear saturation value of the ripple wavelength is detectable in the investigated fluence range. It is continuously increasing. Differently, at 67° and 68° ion incidence there is a clear saturation at a fluence of $5x10^{17} ions/cm^2$ when stronger coarsening is observed. Moreover, the roughness time evolution does not follow the theoretical predictions. Experimentally samples which show marginal coarsening are more ordered, corresponding to lower values of roughness. According to the model, the surface morphology should be more disordered (larger roughness) for smaller values of the ratio *r* between the second and the first non linearities [24]. Generally it is difficult to draw a direct correlation between the simulation and experimental parameters. Therefore, for a detailed prediction of the angular dependence of the ratio of the non-linear terms a deeper analysis of the continuum equation has to be performed for the present system since the absolute value of the non linear terms depend on the fraction of eroded atoms that become mobile on the surface, which is strictly connected with the ion-target system.

2. Dot pattern formation

For normal incidence of the ion beam an isotropic dot pattern is expected to form on the surface [25]. In fig. 5a,b,c the Ge surface evolution as a function of Xe ion fluence under normal incidence is shown. The beam energy is 100 eV and the flux is 2,5 x 10^{14} ions/ cm^2 s. For a fluence of 1 x 10^{17} ions/ cm^2 the surface appears smooth; only the presence of some holes can be detected (fig. 5a). Small dots form on the surface at a fluence of 3.5 x 10^{17} ions/ cm^2; in the Fourier space a ring is visible, which indicates the periodicity of the pattern. Further increase of the fluence produces a roughening of the surface; in the Fourier space the ring disappears (fig. 5c).

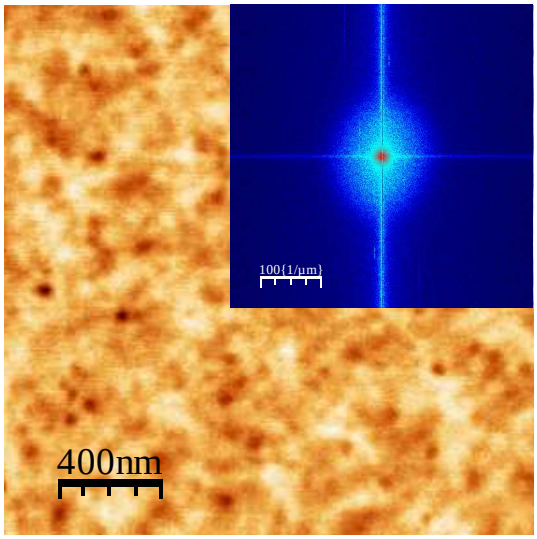

Fig.5a $Xe^{+} \rightarrow$ Ge, 100 eV, 1 x 10^{17} ions/cm^{2}

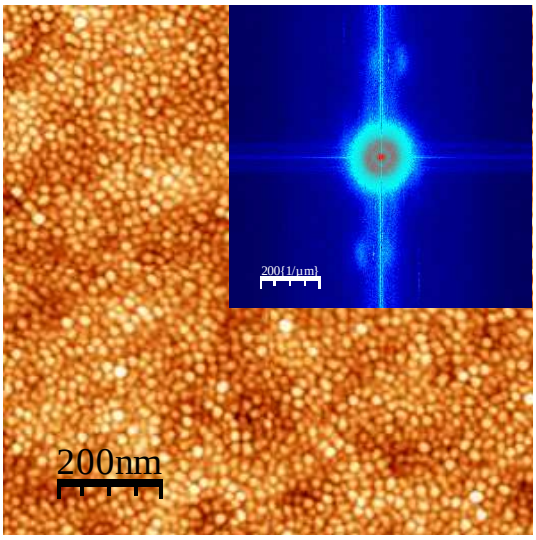

Fig. 5b $Xe^{+} \rightarrow$ Ge, 100 eV, 3.5 x 10^{17} ions/cm^{2}

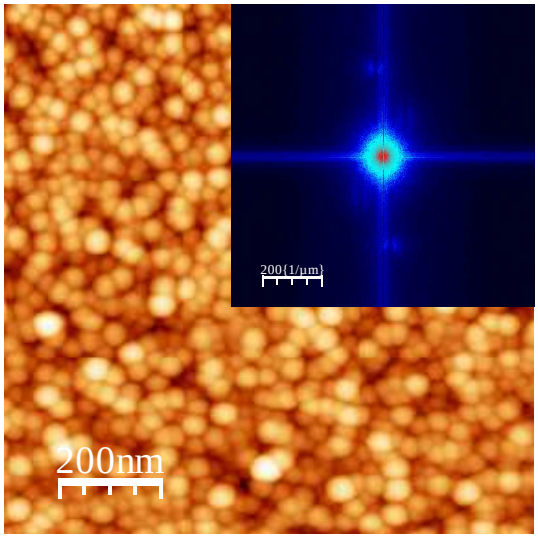

Fig. 5c $Xe^{+} \rightarrow$ Ge, 100 eV, 7 x 10^{17} ions/cm^{2}

These results obtained at normal incidence are in quite good agreement with what has been theoretically predicted by Kahng et al. [25]. To investigate the dynamics of quantum dot formation under normal incidence ion sputtering, they integrated numerically the Kuramoto-Sivashinsky equation [21], using isotropic coefficients as expected for normal incidence. The main goal of their work is shown in fig.6 for three different stages of surface time evolution.

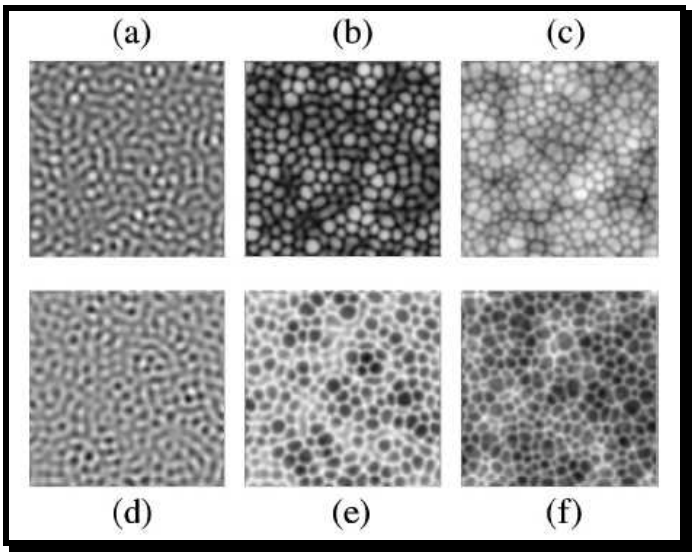

Fig.6 (a)-(c) Surface morphologies predicted for $\lambda = 1$ at different stages of surface evolution. The same in (d)-(f) but for $\lambda = -1$.

In the early stages of the sputtering process the surface is dominated by small perturbations, generated by the interplay between the ion induced instability and surface relaxation. However, since the system is isotropic in the (x,y) plane, these ripple precursors are oriented randomly, generating short wormlike morphologies on the surface. After a characteristic time, these small perturbations turn into isolated but closely packed islands, which are reminiscent of the ones that have been observed experimentally (fig. 5b). With increasing sputtering, the surface develops a rough profile, destroying the uniformity of the islands. This is also in agreement with what has been found on Ge surfaces at high ion fluences (fig. 5c). Considering the results obtained numerically, the authors present the following interpretation for IBS quantum dot formation. In the early stages of the erosion process the linear theory correctly describes the surface evolution, and so the cellular structure predicted by the BH theory [20] is observed. Then, as time increases, the non-linear terms turn on breaking the up-down symmetry of the surface. This happens at a characteristic time τ which depends on the flux and the ion energy. As time increases beyond τ, the non-linear terms lead to kinetic roughening of the surface at large length scales, and while the quantum dots do not

disappear, the substrate on which they exist becomes rough, destroying the overall island uniformity and order.

References

[1] W.L. Chan and E. Chason, J. Appl. Phys. 101, 121301 (2007).

[2] R. Moroni, D. Sekiba, F.B. de Mongeot, G. Gonella, C. Boragno, and U. Valbusa, Phys. Rev. Lett. 91, 167207 (2003).

[3] M.O. Liedke, B. Liedke, A. Keller, B. Hillebrands, A. Mucklich, S. Facsko, and J. Fassbender, Phys. Rev. B 75, 220407 (2007).

[4] T.W.H. Oates, A. Keller, S. Facsko and A. Mucklich, Plasmonics 2, 47 (2007).

[5] L. Vattuone, U. Burghaus, L. Savio, M. Rocca, G. Costantini, F.B. de Mongeot, C. Boragno, S. Rusponi, and U. Valbusa, J. Chem. Phys. 115, 3346 (2001).

[6] S. Rusponi, G. Costantini, C. Boragno, and U. Valbusa, Phys. Rev. Lett. 81, 4184 (1998).

[7] C.C. Umbach, R.L. Headrick, and K.C. Chang, Phys. Rev. Lett. 8724, 246104 (2001).

[8] G. Carter and V. Vishnyakov, Phys. Rev. B 54, 17647 (1996).

[9] D.P. Datta and T.K. Chini, Phys. Rev. B 69, 235313 (2004).

[10] B. Ziberi, F. Frost, T. Hoche, and B. Rauschenbach, Phys. Rev. B 72, 235310 (2005).

[11] A.D. Brown and J. Erlebacher, Phys. Rev. B 72, 075350 (2005).

[12] A. Keller, S. Rossbach, S. Facsko, and W. Moeller, Nano. Techn. 19, 135303 (2008).

[13] D. Carbone, A. Alija, O. Plantevin, R. Gago, S. Facsko, and T.H. Metzger, Nano. Techn. 19, 035304 (2008).

[14] B. Ziberi, F. Frost, and B. Rauschenbach, Appl. Phys. Lett. 88, 173115 (2006).

[15] E. Chason, T.M. Mayer, B.K. Kellerman, D.T. McIlroy, and A.J. Howard, Phys. Rev. Lett. 72, 3040 (1994).

[16] D. Flamm, F. Frost, D. Hirsch, Appl. Surf. Sci. 179, 95 (2001).

[17] P. Sigmund, J. Mater. Sci. 8, 1545 (1973).

[18] M.A. Makeev and A.L. Barabasi, Appl. Phys. Lett. 71, 2800 (1997).

[19] T.M. Mayer, E. Chason, and A.J. Howard. J. Appl. Phys. 76, 1633 (1994).

[20] R.M. Bradley and J.M.E. Harper, J. Vac. Sci. Technol. A 6, 2390 (1988).

[21] R. Cuerno and A.L. Barabasi, Phys. Rev. Lett. 74, 4746 (1995).

[22] M. Castro, R. Cuerno, L. Vazquez, and R. Gago, Phys. Rev. Lett. 94, 016102 (2005).

[23] J. Munoz-Garcia, M. Castro, and R. Cuerno. Phys. Rev. Lett. 96, 086101 (2006).

[24] J. Munoz-Garcia, R. Cuerno, M. Castro, Phys. Rev. B 78, 205408 (2008).

[25] B. Kahng, H. Jeong, and A.L. Barabasi, Appl. Phys. Lett. 78, 805 (2001).

Chapter 5

He atom diffraction from solid surfaces

1. About HAS

Scattering of monoenergetic beams of neutral particles from single crystalline solid surfaces has gained increasing interest since the end of the 1970s, especially due to the progress in combining ultra high vacuum techniques with high pressure nozzle beam producing systems [1]. Because of the low energies used, between 10 and 300 meV, the incident atoms are able to probe the topmost layer of the substrate surface in an absolutely nondestructive manner. Moreover they can investigate equally insulators, semiconductors and metals [2]. When a low energy beam of light particles like He is used, the scattering is predominantly elastic and diffraction effects dominate, since the de Broglie wavelengths are of the order of several tenths to a few Ångströms. Measurements of diffraction spectra allow to determine the size and the orientation of the surface unit cells through the angular location of the diffraction peaks and, more important, to calculate the surface corrugation through the analysis of diffraction intensities. In this way it is possible to obtain a direct picture of the geometrical arrangement of surface atoms [3-5]. Moreover, He beams are very sensitive in detecting the presence of very small amounts of surface impurities, down to 0.001 ML [2]. He atoms travelling towards the target with thermal energy feel an attraction due to van der Waals forces at distances not too far from the surface. Closer to the surface, they will be repelled

due to the overlap of their electronic wavefunctions with those of the atoms forming the solid surface (Pauli exclusion); for this reason the repulsive part of the interaction potential rises steeply. A qualitative picture of the interaction potential is shown in fig.1 [2].

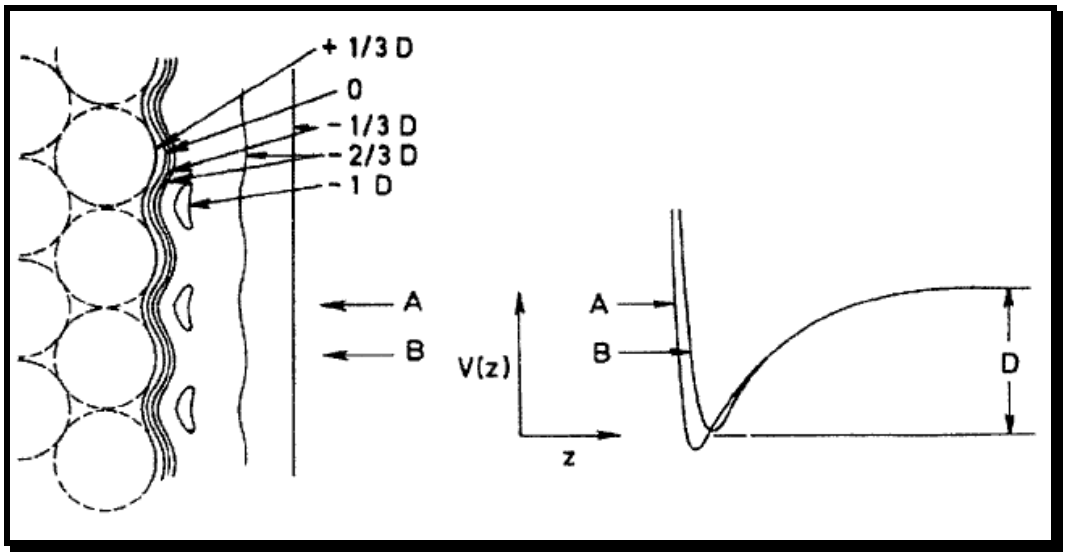

Fig.1 Schematic diagram showing equipotential lines for the interaction of an atom with an ordered surface. The (negative) potential energies are given in terms of the depth of the potential well *D*. On the right-hand side, the potential as a function of *z* (normal to the surface) for two different positions *A* and *B* is illustrated.

This scheme comes from calculations for a monoatomic solid perfomed by starting from individual particle-atom potentials and then summing over all binary interactions between the particle and the atoms in the solid. Generally, classical turning points are farther away for particles impinging on top of the surface atoms than for particles impinging between them. For this reason the repulsive part of the potential is periodically modulated. The resulting scattering surface is called the 'corrugation function' $\zeta(\mathbf{R})$ [6], where **R** indicates a two-dimensional vector in the surface plane. In the work of Esbjerg and Norskov [6], it is shown how $\zeta(\mathbf{R})$ corresponds in first order to a contour of constant surface electronic charge density $\rho(\mathbf{r})$ which is proportional to the particle energy $E(\mathbf{r})$:

$$E(\mathbf{r}) = \alpha\, \rho(\mathbf{r}) \qquad (1)$$

For this reason, thermal He atoms can investigate densities between $1\text{x}10^{-4}$ and $2\text{x}10^{-3}$ au with classical turning points about 2-3 Å away from the surface atom cores. The arrangement of the surface atoms can consequently be obtained by relating the experimental corrugation $\zeta(\mathbf{R})$ to calculations of surface charge density profiles. It is important to note that such a description implies

that the surface corrugation should increase with increasing kinetic energy, since high energy atoms penetrate deeper into the electron density profile. Experimentally it was found that this statement is not correct, since the corrugation can remain constant or even decrease by increasing the incoming energy of a factor of 3 [7]. This shows that the simple model proposed by Esbjerg and Norskov [6] is not always valid. Basically the main problem in relating models of surfaces to atom diffraction data is that of determining the surface charge density in regions where its value is about 10^{-4} electrons per $(au)^3$. This is not easily predictable since at such values of densities the effects of inhomogeneities in the electron gas become important. The method which is usually used to calculate charge density profiles is the overlapping of atomic charge densities through the approach introduced by Haneman and Haydock [8], in which the atomic wavefunctions are computed with a Herman-Skillman-like program [9]. This approach works well as long as bondings effects can be neglected, which is the case of clean metals.

At this point of the discussion it is worthful to summarize briefly some basic elements of diffraction kinematic for periodic two-dimentional systems. The wavelength λ of a particle of mass m and energy E_i impinging on a surface at an angle ϑ_i measured respect to the surface normal, is related to the particle energy through the de Broglie relation :

$$\lambda = \frac{h}{\sqrt{2mE_i}} \qquad (2)$$

The incoming vector $\boldsymbol{k_i}$ is related to the wavelength λ by $|\boldsymbol{k_i}| = 2\pi/\lambda$. The wavevector **k** can be separated into two components, one parallel and one perpendicular to the surface. Thus the incoming and outgoing wavevectors become : $\mathbf{k_i} = (\mathbf{K}, k_{iz})$ and $\mathbf{k_G} = (\mathbf{K_G}, k_{Gz})$. The Bragg condition for diffraction from a two-dimentional periodic array is given by:

$$\mathbf{K} + \mathbf{G} = \mathbf{K_G} \qquad (3)$$

where **G** is a reciprocal lattice vector. Since the particle energy remains unchanged during diffraction, $k_i = k_G$. Thus the number of reciprocal lattice vectors for which diffraction can occur is limited. This is well visualized by the Ewald construction, which is shown in fig.2 [2].

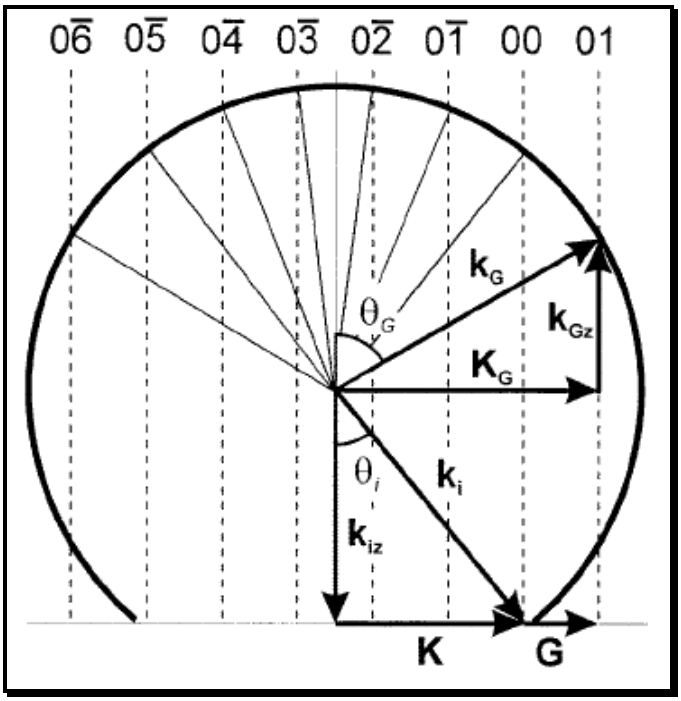

Fig.2 The Ewald construction for diffraction from surfaces. The notation used in this section is illustrated for the reciprocal vector ***G*** = (01).

It is possible to determine the dimension of the surface unit cell and its orientation relative to the incoming beam by measuring the angular location of the diffraction peaks. For a two-dimentional corrugation function $\zeta(x,y)$, it is necessary to measure two angles which indicate the scattering direction. Assuming that the incoming wavevector $\mathbf{k_i}$ is parallel to the unit cell vector $\mathbf{a_2}$, the following formula for the peak *jl* located at ϑ_{jl} and ϕ_{jl} can be derived :

$$\sin\phi_{jl} = -\lambda\frac{j}{a_1} \qquad (4)$$

$$\sin\vartheta_{jl} = \frac{1}{\cos\phi_{jl}}\left[\sin\vartheta_i + \lambda\frac{l}{a_2}\right] \qquad (5)$$

Here ϑ_{jl} is measured in the scattering plane and ϕ_{jl} is measured away from this plane and is called 'out-of-plane' angle.

2. Close couplings calculations

To calculate diffraction intensities for a given scattering geometry and corrugation function it is necessary to solve the time-independent Schrödinger equation :

$$-\frac{\hbar^2}{2m}\nabla^2\psi(\bar{r})+V(\bar{r})\psi(\bar{r})=E\,\psi(\bar{r}) \qquad (6)$$

with a given model potential $V(\bar{r})$. This problem can be solved exactly in the most general case using the close-coupling method developed by Wolken in 1973 [10,11]. However, this method is very time consuming and consequently it is not appropriate to determine the corrugation function $\zeta(\mathbf{R})$ from measured intensities. In 1990 Manolopoulos et al. [12] proposed a new method which is based on *the log derivative Kohn approach* and applied it to the diffractive scattering of He from LiF(100) [13]. The computer time required to achieve convergence was found to increase quite slowly with the number of channels *N*, compared to the one required for a standard close-coupling calculation, which scales as N^3 [14]. Moreover, a large variety of approximate methods have been developed to calculate diffraction intensities [5]. Among them the '*GR method'* and the '*eikonal approximation*' are the two most employed ones. In the so-called '*hard corrugated wall model*' (HCW), the particle-surface potential is represented by:

$$V(\mathbf{R},z) = \begin{cases} 0, \text{ for } z > \zeta(\mathbf{R}) \\ \infty, \text{ for } z \le \zeta(\mathbf{R}) \end{cases} \qquad (7)$$

where *z* denotes the direction of the surface normal. Neglegting the attractive part of the potential is a reasonable assumption as long as the particle energy is much higher than the potential well *D*. For He, *D* values are usually between 5 and 10 meV, so that with a 63 meV room temperature He beam this condition is well fulfilled. A very simple procedure to calculate diffraction intensities within the HCW approximation was developed by Garcia in 1976 [15,16] and is referred to as the *GR model*. The starting point is the so-called Rayleigh assumption [17], which considers the incoming and outgoing beams as plane waves up to the surface. The total particle wavefunction becomes :

$$\psi(\bar{R},z)=\exp\left[i\left(\bar{K}\cdot\bar{R}+k_{iz}z\right)\right]+\sum_G A_G\exp\left\{i\left[\left(\bar{K}+\bar{G}\right)\cdot\bar{R}+k_{Gz}z\right]\right\} \qquad (8)$$

The first term represents the incident beam of wavevector $\mathbf{k_i} = (\mathbf{K}, k_{iz})$ and the others the diffracted beams with wavevectors $\mathbf{k_G} = (\mathbf{K_G}, k_{Gz})$ and scattering amplitudes A_G, corresponding to each two-dimentional reciprocal vector lattice **G**. To determine the amplitudes A_G it is necessary to impose the boundary condition $\psi[\mathbf{R}, z = \zeta(\mathbf{R})] = 0$ to obtain :

$$\sum_G A_G\exp\left\{i\left[\bar{G}\cdot\bar{R}+k_{Gz}\zeta(\bar{R})\right]\right\}=-\exp\left[ik_{iz}\zeta(\bar{R})\right] \qquad (9)$$

From the last equation it is possible to obtain the matrix :

$$\sum_G A_G M_{GR} = -1 \tag{10}$$

with

$$M_{GR} = \exp\left\{i\left[\left(k_{Gz} - k_{iz}\right)\zeta\left(\overline{R}\right) + \overline{G}\cdot\overline{R}\right]\right\} \tag{11}$$

This equation must be satisfied for each point **R** in the unit cell. Choosing now a finite set of *n* vectors $\mathbf{R}_n$ uniformly distributed over the surface unit cell and relating them to the same number of reciprocal lattice vectors **G**, it is possible to consider eq.(11) as a set of *n* linear equations which can be solved by matrix inversion for the A_G's. This is the basis of the *GR method* developed by Garcia [16]. Finally the scattered intensities P_G are obtaining by :

$$P_G = \frac{\left|k_{Gz}\right|}{\left|k_{iz}\right|} A_G A_G^* \tag{12}$$

where the kinematic factor is due to the cross section ratio of impinging and emerging beams. Since all the scattering from the rigid wall is elastic, the diffracted intensities have to satisfy the unitarity condition :

$$\sum_G P_G = 1 \tag{13}$$

It was found that the hard-wall boundary condition can be satisfied to a good approximation with a finite number of terms in the expansion (9), even though the expansion can eventually diverge. In such cases, calculations can be performed beyond the Rayleigh limit but convergence is more difficult to achieve as λ increases [18].

Starting from eq.(9), multiplying both of its sides by $\exp\left\{-i\left[\overline{G'}\cdot\overline{R} + k_{G'z}\zeta\left(\overline{R}\right)\right]\right\}$ and integrating over the unit cell it is possible to obtain the matrix equation :

$$\sum_G M_{GG'} A_G = A_{G'}^0 \tag{14}$$

where

$$M_{GG'} = \frac{1}{S}\int_{u.c.} \exp\left\{i\left[\left(\overline{G} - \overline{G'}\right)\cdot\overline{R} + \left(k_{Gz} - k_{G'z}\right)\zeta\left(\overline{R}\right)\right]\right\} d\overline{R} \tag{15}$$

and

$$A_{G'}^0 = \frac{1}{S}\int_{u.c.} \exp\left\{-i\left[\overline{G'}\cdot\overline{R} + \left(k_{G'z} - k_{iz}\right)\zeta\left(\overline{R}\right)\right]\right\} d\overline{R} \tag{16}$$

where S is the unit cell area. The diagonal elements of the matrix $M_{GG'}$ are all equal to unity. Its off-diagonal elements are given by :

$$M_{mn} \approx \frac{\pi}{2}\frac{\zeta_m}{a}\tan\vartheta_i \qquad m \neq n \qquad (17)$$

where ζ_m indicates the maximum corrugation amplitude and a is the lattice constant. This means that in cases where $\zeta_m \leq 0.1a$ and the angle of incidence is small (less than 45°), they can be neglected and eq. (14) becomes :

$$A_G = A^0_{G'} \qquad (18)$$

This is the so-called *eikonal approximation* [19], from which the diffraction probabilities can be calculated by simply evaluating the Fourier transform of a phase factor. The *eikonal approximation* is not necessarily restricted to cases where the diffraction is weak, but its range of convergence is slightly smaller than for the *GR method*.

The methods discussed previously deal with the problem of obtaining diffraction intensities for a given corrugation function $\zeta(x,y)$, but usually one faces the inverse problem of determining $\zeta(x,y)$ from a set of measured spectra. Since a direct inversion of the experimental data is not possible (measured intensities do not contain information on the phases of the scattered waves), the *trial-and-error approach* must be adopted [2]. Assuming for the corrugation function the Fourier series :

$$\zeta\left(\overline{R}\right) = \frac{1}{4}\sum_G \zeta_G \exp\left(i\overline{G}\cdot\overline{R}\right) \qquad (19)$$

the best-fit coefficients can be determined by varying their amplitudes until optimum agreement between the measured $P_G^{\exp}$ and the calculated intensities P_G^{calc} is reached. The degree of agreement is judged by using reliability factors which can be defined as :

$$R = \frac{1}{N}\sqrt{\sum_G \left(P_G^{\exp} - P_G^{calc}\right)^2} \qquad (20)$$

where N indicates the number of beams G measured and the intensities are normalized to the specular beam.

3. The Debye-Waller factor

Finally it is important to underline that the theoretical methods for the calculation of diffraction intensities presented till now assume that the atoms of the lattice are at rest. However, both zero-

point motion and thermal vibrations of the surface atoms lead to inelastic scattering of the incoming atoms [2]. The basic effect of this is a thermal attenuation of the coherent diffraction intensities without a change of the peak shape. The Debye-Waller factor relates the intensity $I(T)$ of a diffraction peak with the intensity I_0 from a lattice at rest by :

$$I(T) = I_0 e^{-2W(T)} \tag{21}$$

where $exp[-2W(T)]$ is the Debye-Waller factor and

$$W(T) = \frac{1}{2}\left\langle \left(\vec{u} \cdot \overline{\nabla k_i}\right)^2 \right\rangle_T \tag{22}$$

Here u is the displacement of a lattice atom from its equilibrium position, $\overline{\nabla k_i}$ is the momentum tranfer in the scattering event and the outer brackets refer to a thermal average. The assumption underlying these expressions is that the interaction in the scattering event is both weak and short. This is actually not true in the case of scattering of thermal atoms from surfaces, since collision times are longer than phonon vibration periods. Recently Manson has derived an expression in the semiclassical limit for a quantum mechanical description of inelastic scattering [20]. For the specular beam the Debye-Waller factor can be written as:

$$W(T) = \frac{12m(E_i \cos^2 \vartheta_i + D)T}{Mk_B \Theta_D^2} \tag{23}$$

where m is the particle mass, M the mass of the surface atom, E_i the incident beam energy, ϑ_i the angle of incidence, D the well depth and Θ_D the surface Debye temperature. This equation indicates that the strength of the diffraction intensities is higher for grazing incidence, low incidence energy and low surface temperatures, in agreement with experiments.

References

[1] G. Scoles, Atomic and Molecular Beam Methods, vol.1, New York - Oxford University Press (1988); G. Scoles, Atomic and Molecular Beam Methods, vol.2, New York - Oxford University Press (1992).

[2] D. Farias and K.H. Rieder, Atomic beam diffraction from solid surfaces, Rep. Prog. Phys. 61, 1575 (1998).

[3] T. Engel and K.H. Rieder, Structural Studies of Surfaces with Atomic and Molecular Beam Diffraction, Berlin - Springer (1982).

[4] K.H. Rieder, Helium Atom Scattering from Surfaces, ed. E. Hulpke, Berlin – Springer (1992).

[5] J.R. Manson, Helium Atom Scattering from Surfaces, ed. E. Hulpke, Berlin – Springer (1992).

[6] N. Esbjerg and J.K. Norskov, Phys. Rev. Lett. 45, 807 (1980).

[7] K.H. Rieder, Surf. Sci. 117, 13 (1982).

[8] D. Haneman and R. Haydock, J. Vac. Sci. Technol. 21, 330 (1982).

[9] F. Herman and S. Skillman, Atomic Structure Calculations, (1963).

[10] G. Wolken, J. Chem. Phys. 58, 3047 (1973).

[11] G. Wolken, J. Chem. Phys. 59, 1159 (1973).

[12] D.E. Monolopoulos, R.E. Wyatt and D.C. Clary, J. Chem. Soc. Faraday Trans. 86, 1641 (1990).

[13] D.E. Monolopoulos and R.E. Wyatt, Chem. Phys. Lett. 152, 23 (1988).

[14] R.J. Blake, Comput. Phys. Commun. 33, 425 (1984).

[15] N. Garcia, Phys. Rev. Lett. 37, 912 (1976).

[16] N. Garcia, J. Chem. Phys. 67, 897 (1977).

[17] J.W. Strutt, The Theory of Sound, vol. 2, London – Macmillan (1896).

[18] E. Stoll, M. Baumberger and N. Garcia, J. Chem. Phys. 81, 1496 (1984).

[19] U. Garibaldi, A.C. Levi, R. Spadacini, and G.E. Tommei, Surf. Sci. 48, 649 (1975).

[20] J.R. Manson, Phys. Rev. B 43, 6924 (1991).

Chapter 6

A single graphene layer grown on Ru(0001)

1. About graphene

Graphene is the name given to a flat monolayer of carbon atoms tightly packed into a two-dimensional (2D) honeycomb lattice, and represents the basic building block for graphitic materials of all other dimensionalities, like 0D fullerenes, 1D nanotubes or 3D graphite (see Fig.1) [1]. Theoretically graphene has been studied for more than sixty years [2-4] to describe properties of carbon-based materials, but for most of this time it has been believed not to exist in the free state and to be unstable with respect to the formation of curved structures like fullerenes and nanotubes. Indeed the melting temperature of thin films rapidly decreases with decreasing thickness, and the films become unstable, i.e. segregate into islands or decompose, at a thickness of typically dozens of atomic layers [5,6]. For this reason, atomic monolayers have been known for long time only as parts of larger 3D structures, usually grown epitaxially on-top of monocrystals with matching crystal lattices [5,6]. So 2D materials were presumed not to exist without such a 3D base, until 2004, when an experimental method to prepare free-standing graphene with the same structure as the single layers in graphite has been published [7], giving rise to an enormous scientific activity. In

the case of graphene, it was shown that the electronic structure rapidly evolves with the number of layers, reaching the 3D limit of graphite at approximately 10 layers [8]. Moreover, only graphene and its bilayer has simple electronic spectra since they are both zero-gap semiconductors with one type of electron and one type of hole. For three or more layers, the spectra become much more complex with conduction and valence bands starting to overlap [7,8].

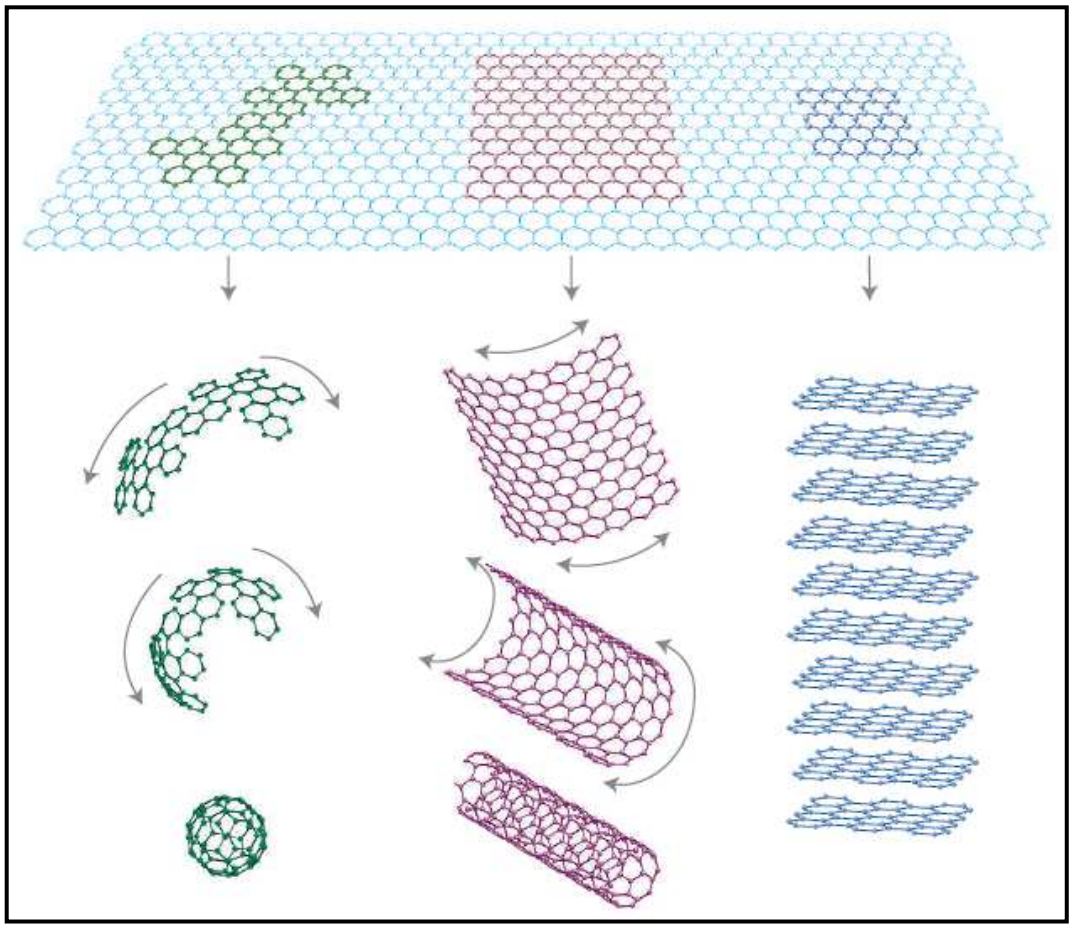

Fig.1 Basic of all graphitic forms. Graphene is a 2D building material for carbon materials of all other dimensionalities. It can be wrapped up into 0D buckyballs, rolled into 1D nanotubes or stacked into 3D graphite.

Experimentally the formation of graphene on metal surfaces was first observed during preparation of Pt and Ru single crystal surfaces, when during annealing to high temperatures carbon impurities segregated from the bulk to the surface [9-12]. Graphene on metal surfaces has also found a wide

application in industrial heterogeneous catalysis, where the deposition of graphitic carbon on the catalyst surface upon reactions involving hydrocarbons, is largely used for deactivation [13,14]. It is not surprising that the current increasing effort employed in producing free-standing graphene has somehow renewed the interest in growing graphene on metal substrates. These systems represent the third main field in graphene research together with investigations of free-standing graphene and epitaxial layers on SiC. Indeed the decomposition of SiC is the second mayor method for graphene preparation [15,16], except the mechanical exfoliation from graphite.

A very important issue is the determination of the interaction between the graphene overlayer and the metal substrate, since it can be very different from the case of free-standing or SiC supported graphene. Moreover, it is interesting to investigate the overlayer reactivity to adsorbed molecules, in view of possible changes in the conduction properties of graphene due to the interaction with them. Nanostructuring graphene (in stripes, dots or by periodic potentials), in turn, may reveal new physical phenomena and fascinating applications [17]. Most of these topics can be characterized in detail in what has become a benchmark system for epitaxial graphene: a self-organized, millimeter large, periodically 'rippled' epitaxial monolayer of graphene grown by soft chemical vapor deposition under ultra high vacuum (UHV) conditions on single crystal metal substrates with hexagonal symmetry, such as Ru(0001) [18-20], Ir(111) [21,22] or Pt(111) [23]. The superb control that allows the UHV environment facilitates a characterization of the system down to the atomic scale. The difference in lattice parameter between graphene (gr) and the different metal substrates originates the appearance of moiré patterns (i.e. a new lattice generated by superposition of two different lattices) with a range of apparent vertical corrugations and lateral periodicities with respect to the basic graphene structure [18,23]. In-situ STM imaging of graphene monolayers on Ru(0001) or Ir (111) reveals periodic corrugations with 12×12 [18-20] or 11×11 [21,22] periodicities, respectively. Fig.2 compares the observed STM images for monolayers of graphene grown on Ru(0001) and Ir(111), respectively. For gr/Ir(111), the darker areas correspond to regions where the C atoms are in the three-fold hollow sites and therefore the rings have their center above an Ir atom. For gr/Ru(0001), on the contrary, these locations show up as bright bumps.

The bonding between the graphene and the metallic substrates is also different as reflected in the X-Ray Photoelectron Spectroscopy C1s core levels, which show two peaks, i.e. two differently bonded C atoms for gr/Ru(0001), but only one for gr/Ir(111) [24].

The apparent corrugation of the respective moiré patterns is much larger for gr/Ru (1 Å) than for gr/Ir (0.2 Å) at these particular tunneling setpoints. For gr/Ru(0001), in contrast, the apparent corrugation changes dramatically with the bias voltage while, for gr/Ir(111), it is always of the order of 0.2 Å.

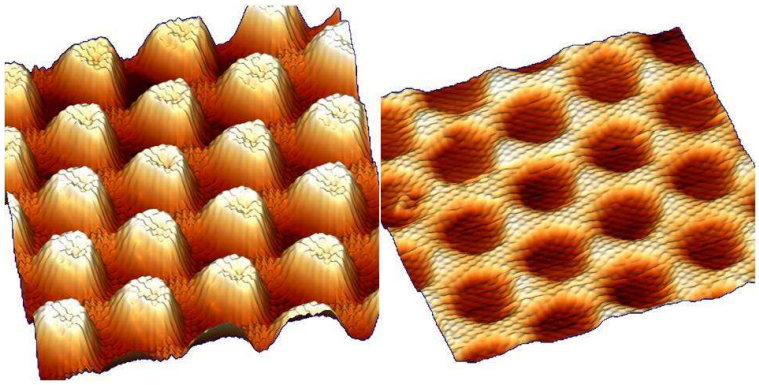

Fig.2 Representative STM images of the different kind of ripples associated to the incommensurate moiré superstructures observed when growing epitaxial graphene on metal surfaces such as Ru(0001) and Ir(111). The gr/Ru(0001) image (130×140 $Å^2$) at the left was recorded with a sample bias voltage of V_S=+1mV and a tunneling current of 1 nA. The gr/Ir(111) image (115×105 $Å^2$) at the right was measured with a sample bias voltage of +0.5 V and a tunneling current of 0.2 nA.

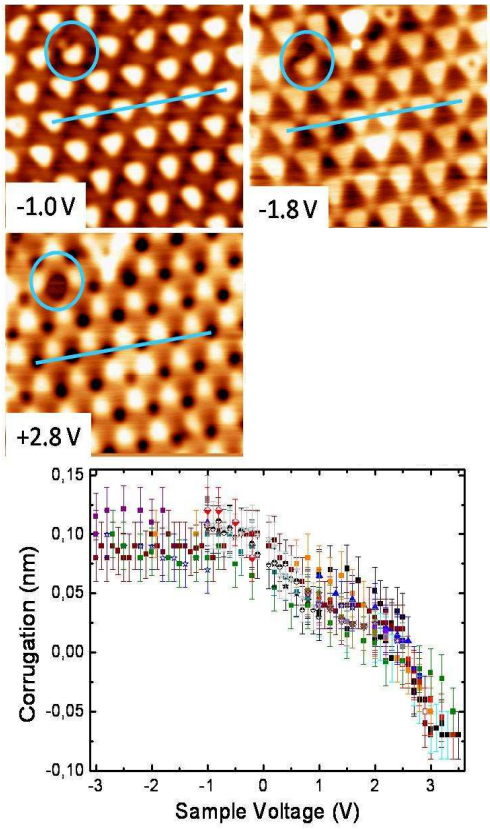

Fig.3 Inversion of the contrast in STM images of graphene/Ru(0001). The upper panels show topographic STM images at three selected sample bias voltages. The lower panel shows the apparent corrugation of the ripples as a function of the bias voltage.

The lateral periodicities are similar on both systems (29.7 vs 27.1 Å). The apparent amplitude in STM of the corrugation of the ripples for gr/Ru(0001) decreases from 1.1 Å to 0.5 Å when the tunneling bias goes from -0.8 to 0.8 V, as shown in Fig.3.

While STM studies ascribed most of the apparent corrugation to electronic effects in a weakly (<0.3 Å) structurally corrugated graphene overlayer, Density Functional Theory (DFT) calculations [25,26] have concluded that the bumps are mostly structural in origin, predicting a geometrical corrugation of 1.5 Å. X-Ray diffraction data [27] have not helped to solve the dilemma because of its reduced sensitivity to the position of the C surface atoms. Recently, a model calculation [28] has found, contrary to the previous DFT calculations, that the structural corrugation of the graphene overlayer is only of the order of 0.15 Å. Considering its paradigmatic nature as a prototype nanostructured graphene system, it is rather upsetting that there is still a lack of consensus regarding the structure of gr/Ru(0001).

2. Experimental results : HAS from graphene

In this work a study of the geometric and electronic structure of graphene epitaxially grown under UHV conditions on Ru(0001) by Helium Atom Scattering (HAS) is presented. The intensity of the He diffracted peaks, allows to quantify accurately the corrugation of the total charge at the external surface (at about the same distance explored by STM), i.e. the closest experimental measure of the geometric corrugation.

The He-diffraction experiments reported here were performed with an apparatus which consists of a three-stage differentially pumped beam system and a 18 inch diameter scattering chamber. The free jet expansion is produced through a nozzle of d=10 μm diameter. The nozzle temperature T_0 can be varied between 100 K and 700K, allowing a variation of the He incident energy between 30 and 160 meV. After expansion, the beam is collimated by a 0.5 mm diameter skimmer and traverses two differential pumping stages before entering the sample chamber. The beam was mechanically chopped with a magnetically coupled rotary motion feedthrough in the third stage to allow phase sensitive detection. The measurements reported here were performed with a source pressure P_0 = 70 bar behind the nozzle. The velocity spread of the He beam was estimated in 3% under these conditions. The base pressure in the chamber was typically $1x10^{-10}$ mbar, reaching $5x10^{-10}$ mbar with the He beam on. The crystal was mounted on a standard manipulator, modified to allow azimuthal rotation of the sample as well as heating to 1200 K and cooling to 90 K. The angular distribution of the scattered He atoms was analyzed with a quadrupole mass spectrometer mounted on a two-axis goniometer. This arrangement allows rotations of 200° in the scattering plane

(defined by the beam direction and the normal to the surface) as well as ±15° normal to the scattering plane for a fixed angle of incidence. In particular, this allows a recording of the incident beam intensity with high accuracy simply by removing the sample from the He-beam and putting the detector behind. The angular resolution of our data acquisition system is 1°, whereas the full width at half maximum (FWHM) of the specular He beam is 1.2°. A schematic view of the experimental apparatus is shown in Fig.4.

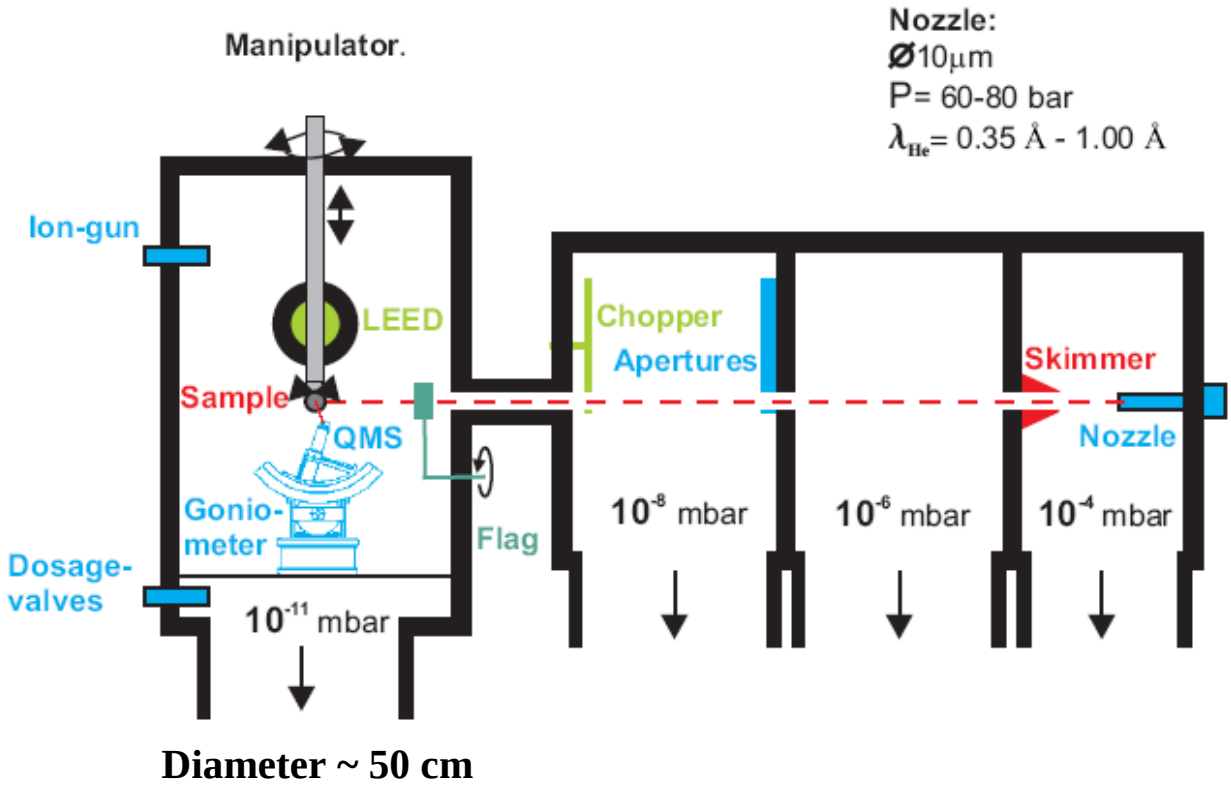

Fig.4 Schematic drawing of the atomic-beam diffraction apparatus.

Atomically clean, bulk C depleted, crystalline Ru(0001) surfaces were prepared by standard sputter/anneal procedures followed by oxygen exposure at 1150 K and a final flash to 1600 K in UHV, which resulted in large terraces (about 2000 Å wide), separated by monoatomic steps. It has been shown that ethylene decompose on Ru(0001) above 750 K in atomic C (that remains at the surface) and H that recombines and desorbs from the surface [29]. The graphene layer was formed in situ by cracking ethylene on the surface. Different partial pressures of ethylene were explored during the growth. The samples of graphene were prepared on multiple occasions on two different Ru(0001) single crystals following the procedure that yields more perfect overlayers and larger domains: the Ru crystals, kept at 1150 K in ultra high vacuum (UHV), were exposed to ethylene at

pressures of 2×10^{-7} mbar for 3 minutes (48 L, 1 L=1.33×10^{-6} mbar s) or 3×10^{-8} mbar for 10 minutes (24 L). These exposures were enough to saturate the surface. The temperature was held at 1150 K for further 2 minutes after removing the C_2H_4 gas from the chamber. The optimum conditions were determined from the combined STM and HAS analysis of the grown graphene films, which display almost atomically perfect domains larger than half square microns covering completely the surface. An example is shown in Fig.5.

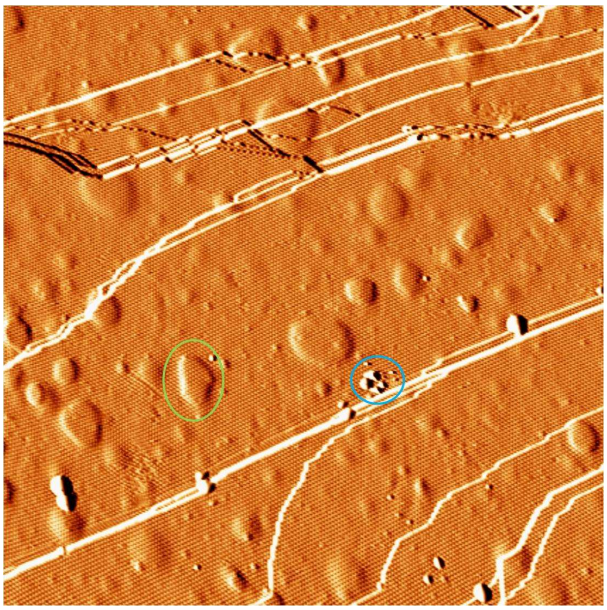

Fig.5 5200×5200 Å^2 STM image of the graphene overlayer. The blue circle encloses material from the tip deposited on the surface. The green circles enclose Argon bubbles buried underneath the Ru(0001) surface that induce a small curvature (2 Å over a lateral range of 500 Å) on it.

The structural corrugation of the graphene monolayer can be determined by HAS. The advantages of using a beam of He atoms of thermal energy (10-100 meV) as a probe of the surface structure are its combination of low energy with short wavelength, its inert and neutral character and its large cross-section for defects. As a consequence, HAS is uniquely non-destructive and surface sensitive, with high sensitivity to low mass atoms, such as C, or light adsorbates, such as H [30]. The actual diffraction grating is the periodic modulation of the repulsive part of the He-graphene potential at the energy of the incoming He atoms. These classical turning points define a corrugation function $\zeta(x,y)$, which is a replica of the total surface electron density profile at about 2-3 Å above the nuclei. The amplitude of the corrugation function dictates the intensity of the diffracted beams. Fig.6 shows the in-plane ($\Phi=0^o$) and out-of-plane ($\Phi=1.3^o$, 15.5^o) diffracted peaks detected when scattering a beam of He of 43 meV off a complete graphene overlayer grown on Ru(0001). The intensity of the specularly reflected (00) peak depends on the structural perfection of graphene, reaching 25% of the

incident beam for highly perfect layers. The in-plane He-diffraction spectrum shows both the (1/12, 1/12) first peaks of the Moiré superstructure of bumps and the (-1,-1) of the C lattice. The relative intensity of the different diffracted peaks with respect to the specular peak, however, determines univocally the corrugation function, $\zeta(x,y)$, i.e. the corrugation of the constant charge density contour where the He atoms are reflected.

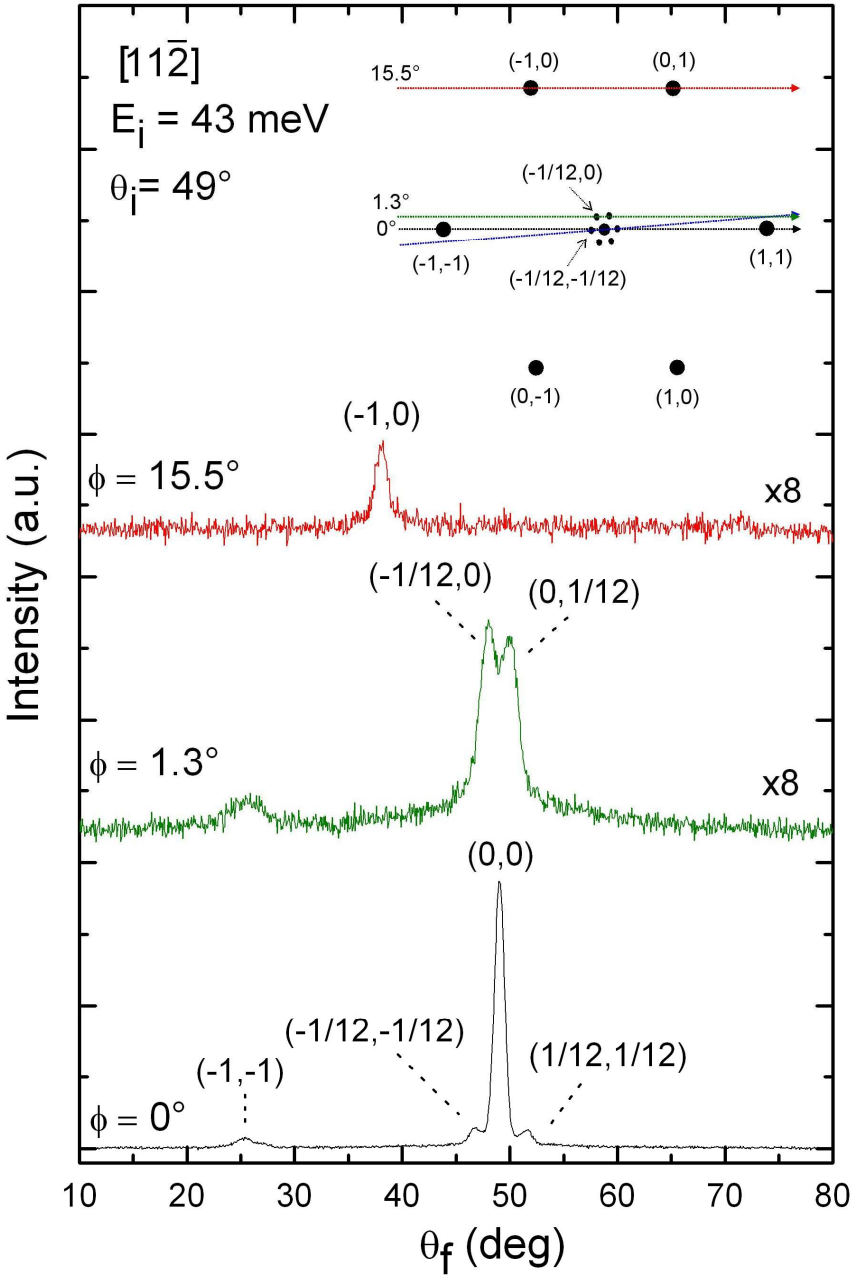

Fig.6 Angular distribution of the He atoms scattered off graphene/Ru(0001). The azimuthal angle, Φ, is defined with respect to the [11-20] direction. The energy of the incident He atoms is 43 meV and the surface is kept at 100 K during the scattering experiments. The inset indicates the reciprocal lattices of graphene and the moiré superstructure.

3. Close-couplings calculations

For the present system, close-coupling equations have been solved applying the procedure developed by Manolopoulos [31,32], which achieves convergence much faster than the method originally proposed by Wolken [33,34] and is therefore more appropriate for calculations of large unit cells like the (12×12) of graphene on Ru(0001). The interaction potential V(**r**) was modeled with a two-parameter Morse potential using for D (potential well depth) and α (range parameter) the values D = 14 meV and α= 1.15 $Å^{-1}$, which were derived from the selective adsorption resonances reported for the He-graphite(0001) interaction by Boato et al. [35]. The unit cell was modeled including both the (1×1) and the (12×12) periodicities, and the corrugation function was determined by fitting the measured in-plane and out-of-plane diffraction intensities by means of a trial and error procedure. The best-fit corrugation function (Fig.7a,b,c) obtained for the (12×12) structure has a maximum corrugation amplitude of 0.15 Å, i.e. one order of magnitude smaller than the value theoretically predicted for graphene overlayers. It is worth mentioning that this value is similar to the one reported for the graphite (0001) surface [35], as expected from the similar intensity observed in Fig. 6 for the C-associated (-1,-1) He diffraction peak and the ones coming from the moiré superstructure. The much larger apparent STM corrugation, which depends strongly on the bias voltage and can even be inverted above +2.6 V, reveals that, in addition to the geometric corrugation, a much stronger electronic corrugation exists.

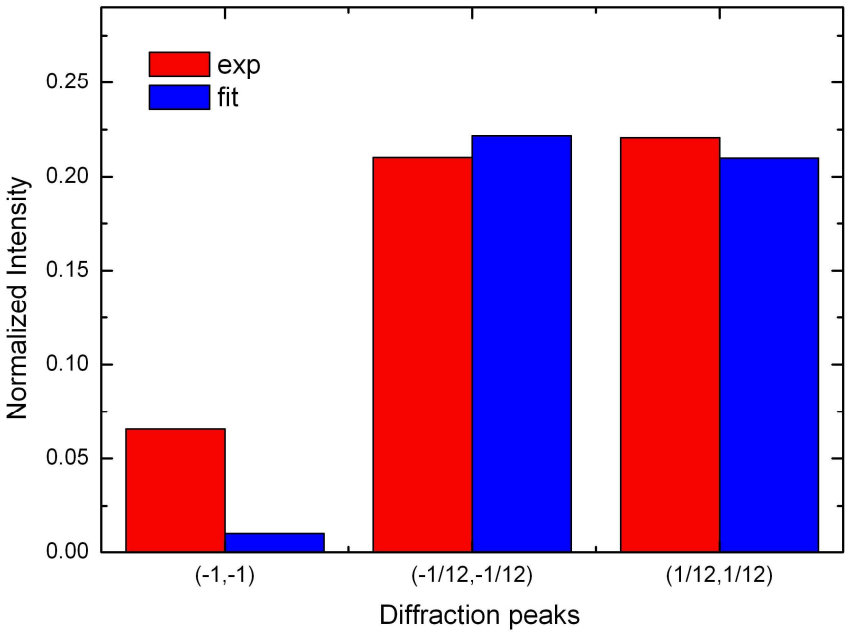

Fig.7a Comparison between measured in-plane diffraction intensities and calculated ones.

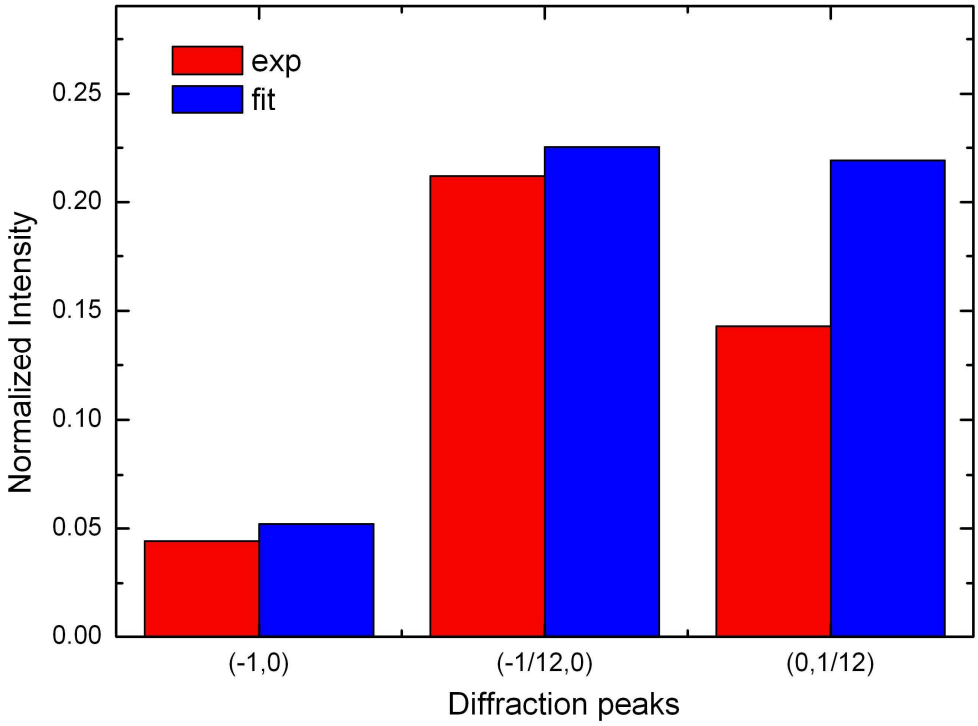

Fig.7b Comparison between measured out-of-plane diffraction intensities and calculated ones.

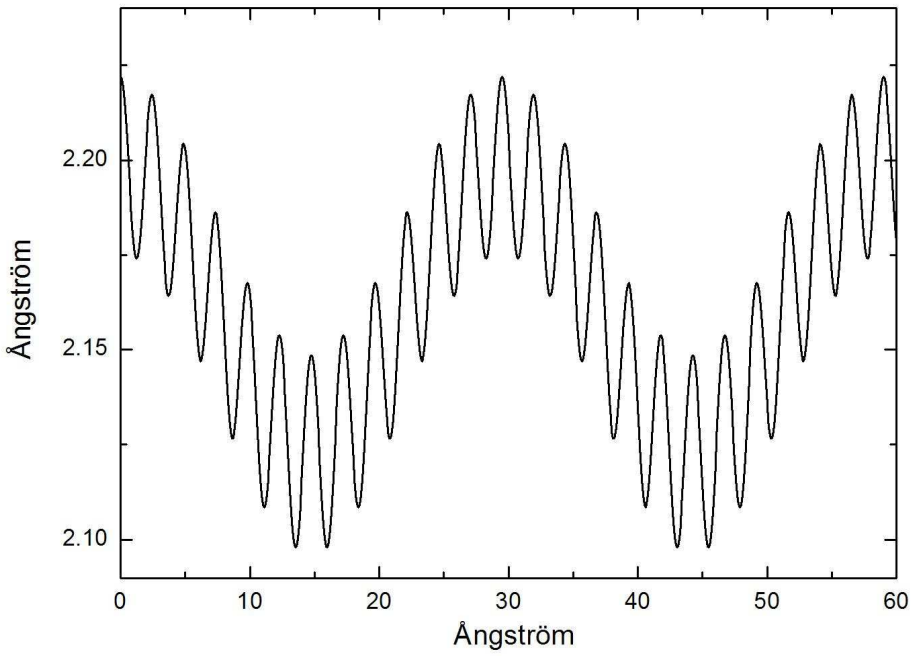

Fig.7c Corrugation function of the graphene overlayer estimated by close-couplings calculations.

4. Graphene as a mirror for the Scanning Helium Atom Microscope

Graphene grown on Ru(0001) exhibits a very promising property, namely its high reflectivity of the incident He beam. These foundings can give a great hint in systems under current investigations. Indeed, even if there is no doubt that the invention of imaging techniques such as scanning tunnelling microscopy (STM) brought a revolution in surface science, in several branches of nanotechnology there is still a need for a technique able to imaging insulating glass surfaces, delicate biological materials and fragile samples which are difficult to examine by STM due to sample charging or electron excitation effects. Perhaps the most important of these techniques, currently under development, is the Scanning Helium Atom Microscope [36,37], which uses a focused beam of neutral He atoms as imaging probe. Such a microscope would be a unique tool for reflection or transmission microscopy, since, as already mentioned, neutral He atoms probe the topmost surface layer of any material in a completely nondestructive manner [30]. The practical realization of such a microscope requires the development of a mirror able to focus a beam of low energy He atoms into a small spot on the sample to be examined. Holst and Allison [36] demonstrated that electrostatic bending of a thin, H-passivated Si(111)-(1x1) crystal was able to focus a 2 mm-He beam to a spot diameter of 210 microns. A serious limitation, however, to improve the resolution was the low intensity obtained in the focused peak, which is a consequence of the poor reflectivity of such surfaces, less than 1%. Whereas the potential lateral resolution of this microscope is ~50 nanometers, the best value reported using current prototypes is 1.5 μm [37,38]. The main limitation to go beyond this value is given by the low reflectivity of the mirrors used to focus the incoming He atoms into the specular beam, which lies near 1% for H-passivated Si(111)-(1x1) mirrors. Recently it has been showed that reflectivities of ca. 15% can be obtained using Pb thin films stabilized by Quantum Size Effects (QSE) on Si(111) surfaces [39]. Whereas this results is very promising, a shortcoming is that such surfaces are stable only up to 250 K, introducing a practical limitation to mirror holders which should be kept below room temperature even when the microscope is not operating. Graphene grown on Ru(0001) seems to be able to overcome these limitations.

In Fig.8 the dependence of the graphene specular reflectivity as a function of the surface temperature is shown. It can be seen that for a beam with incident energy of 65 meV the specular reflectivity can reach a value of ~18% for a surface temperature of 100K, and this value can be still increased. Moreover the graphene specular reflectivity can increase of ~50% by decreasing the incident beam energy from 65 to 10 meV, as shown in Fig.9.

These results are very promising especially considering that graphene is inert to exposure to oxygen even at 100K as shown in Fig.10, in which the reactivity of graphene is compared to the reactivity of a clean Ru(0001) surface.

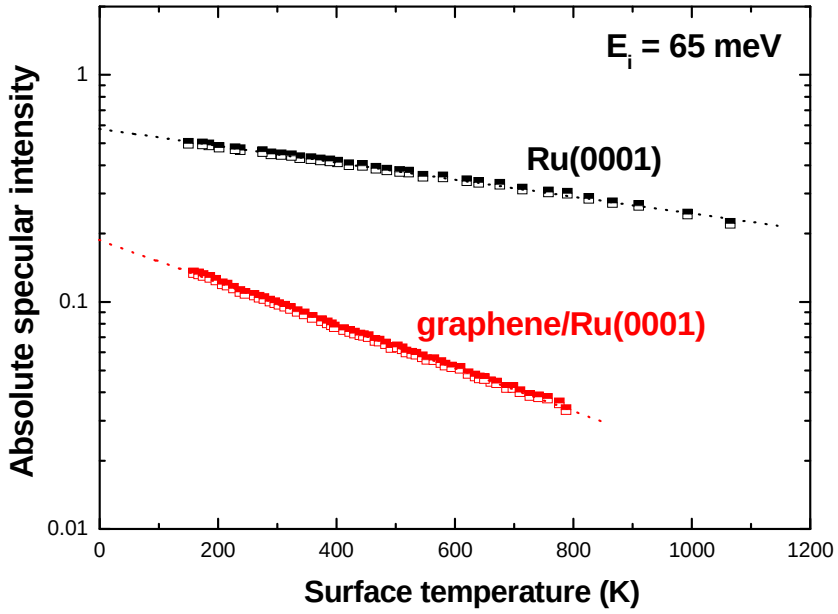

Fig.8 Dependence of the absolute specular intensity on the surface temperature for clean Ru(0001) and graphene grown on it.

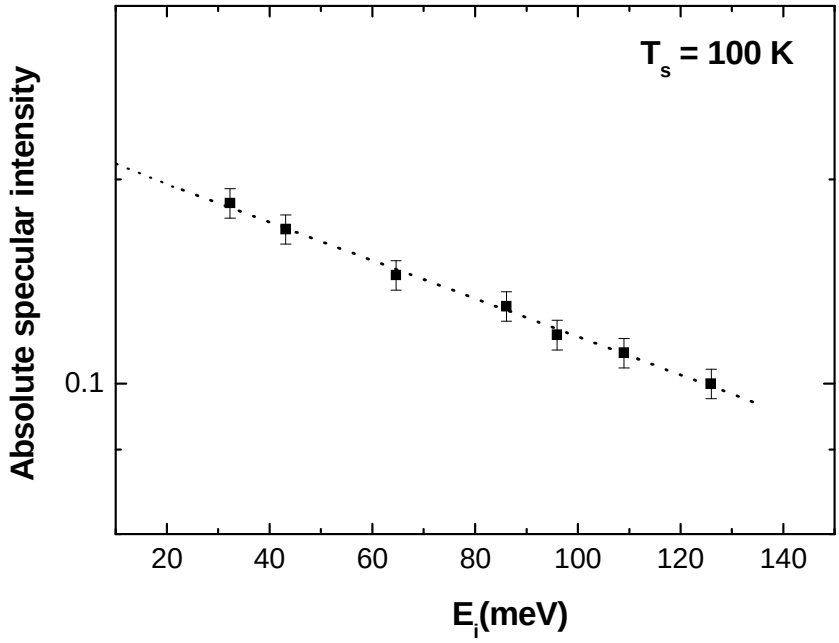

Fig.9 Dependence of the absolute specular relectivity of the graphene overlayer on the beam energy.

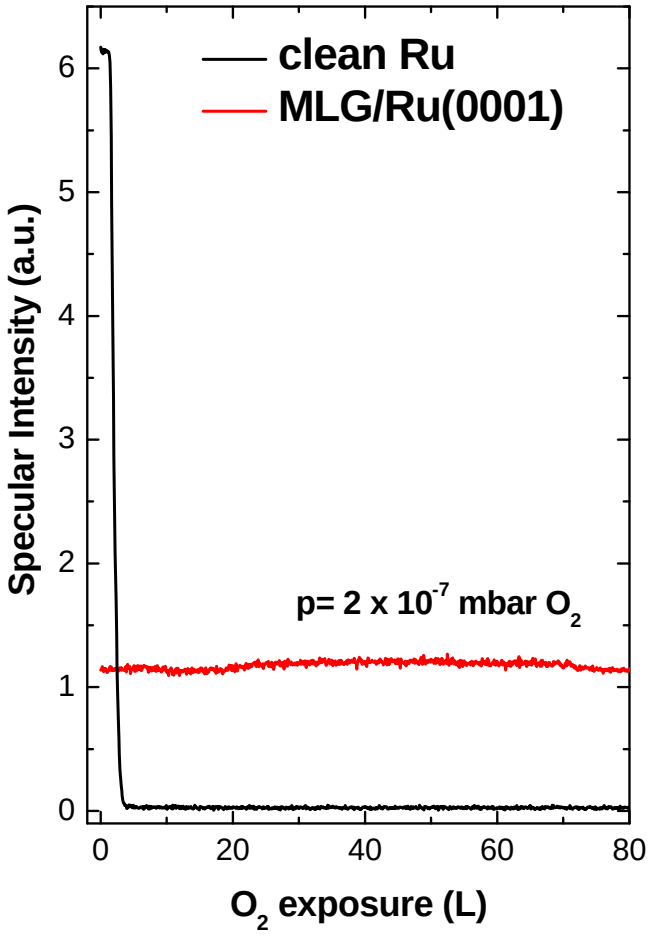

Fig.10 Graphene is inert to oxygen. In a similar experiment performed on Ru(0001) the surface specular reflectivity decreases of about 98%.

Indeed, a long-term stability in UHV is highly required for using such a surfaces as focusing mirrors for microscopy. Moreover, thermal stability of the graphene overlayer has been found to be very high. The sample can be heated up to ~1000 K before graphene starts evaporating.

Another very important property of graphene on Ru(0001) is its relatively high degree of inertness during exposure to air. This is shown in Fig.11. After preparation, the measured graphene reflectivity is ~15%, for a surface temperature of 100K and beam energy of 65 meV. Afterwards the sample has been exposed to air for few minutes and then replaced in UHV. The specular reflectivity has decreased to ~5%, but the initial value of 15% can be easily recovered by heating the sample at 450K for few minutes.

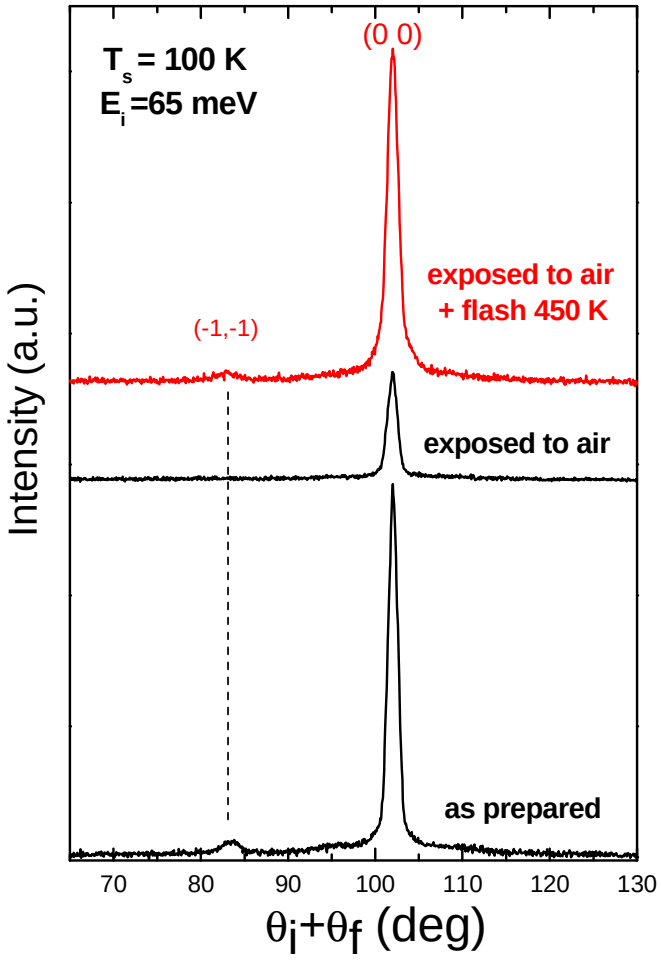

Fig.11 Graphene specular reflectivity can be completely recovered after exposure to air upon a flash at about 450 K.

To conclude, the very high He atom reflectivity observed, together with a very good degree of inertness even after exposure to air, make graphene grown on Ru(0001) an excellent candidate and possibly the ultimate choice as focusing mirror for neutral atoms to be used in the Scanning Helium Atom Microscope.

5. Preliminar results of He, Ne and Ar diffraction from clean Ru(0001)

Atom scattering from surfaces with the help of molecular beam techniques has been successfully applied to the study of the fundamentals of gas–surface interaction. Though a lot has been achieved over the last decades, simple systems with noble gases scattering from crystalline metallic surfaces are still nontrivial to analyse.

In this sense, the Ru(0001) surface has been proposed as an ideal system for studying quantum mechanical scattering of high-massive atomic beams, due to its high substrate-atom mass and large surface Debye-Waller factor [40]. In effect, calculations reported in a work by Hayes and Manson [40] for the scattering dynamics of Ar from Ru(0001) could only be explained upon using an effective surface mass of 2.3 Ru atomic masses, i.e. assuming collective effects of the Ru surface atoms, in which the projectile scatters off from an effective target of more than one substrate atom. This suggests that scattering experiments using projectiles with different masses could give important information on the surface electron density and the different classical turning points of the incident atoms.

In this work, He, Ne, and Ar diffraction experiments from clean Ru(0001) are presented. Fig.1 shows that in case of He scattering on Ru(0001), only the specular peak is observed.

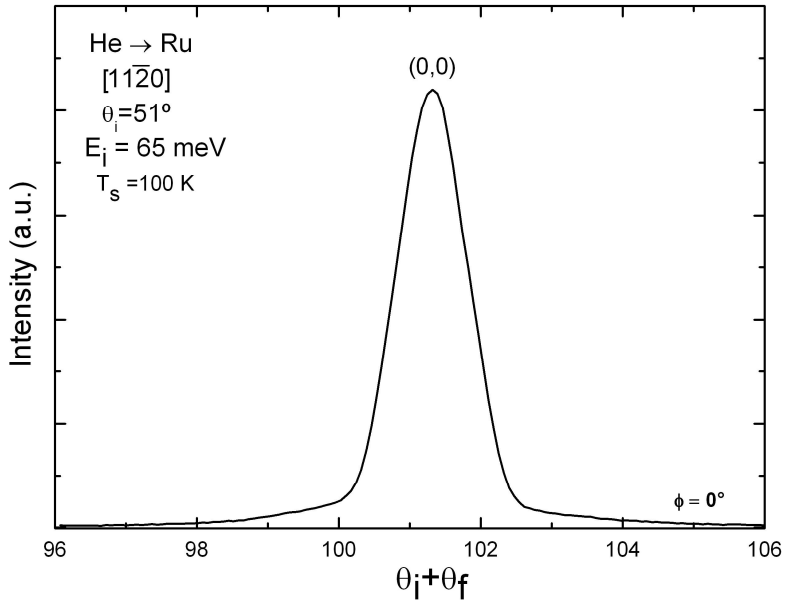

Fig.1 He diffraction from clean Ru(0001). Except the specular peak, no other diffraction peaks are detected.

Differently, pronounced in-plane and out-of-plane diffraction was measured using Ne beams, as shown in Fig.2.

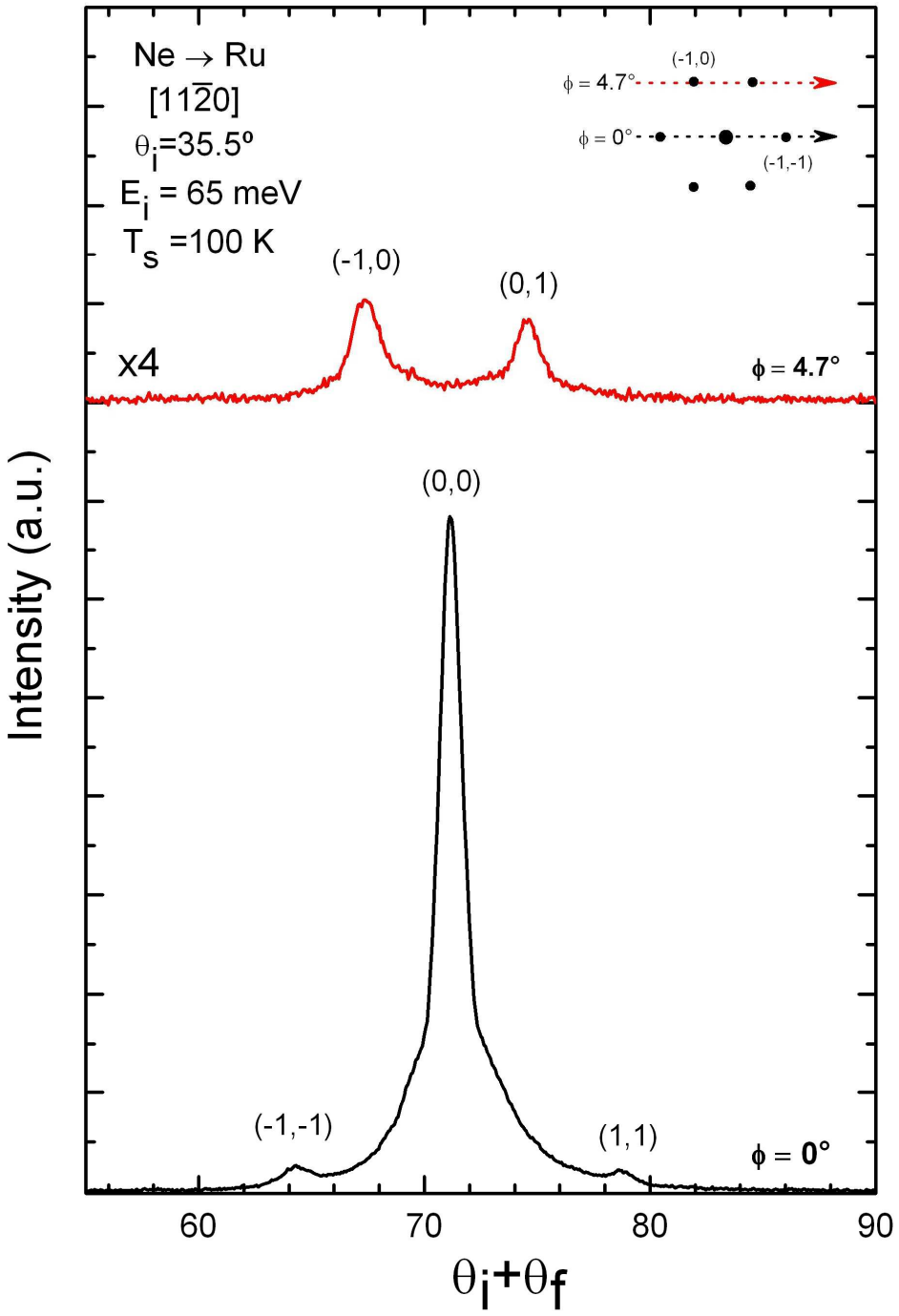

Fig.2 Ne diffraction from clean Ru(0001). Both in-plane and out-of-plane diffraction peaks are visible.

Experiments using low-energy Ar beams (~65 meV) (see Fig.3) provided a clear evidence of several well-distinct diffraction peaks in Ar scattering from clean metal surfaces, while in previous studies only the existence of the specular diffraction peak was reported [41].

These foundings suggests that a larger corrugation amplitude of the Ru(0001) surface can be detected with Ar and Ne compared to He.

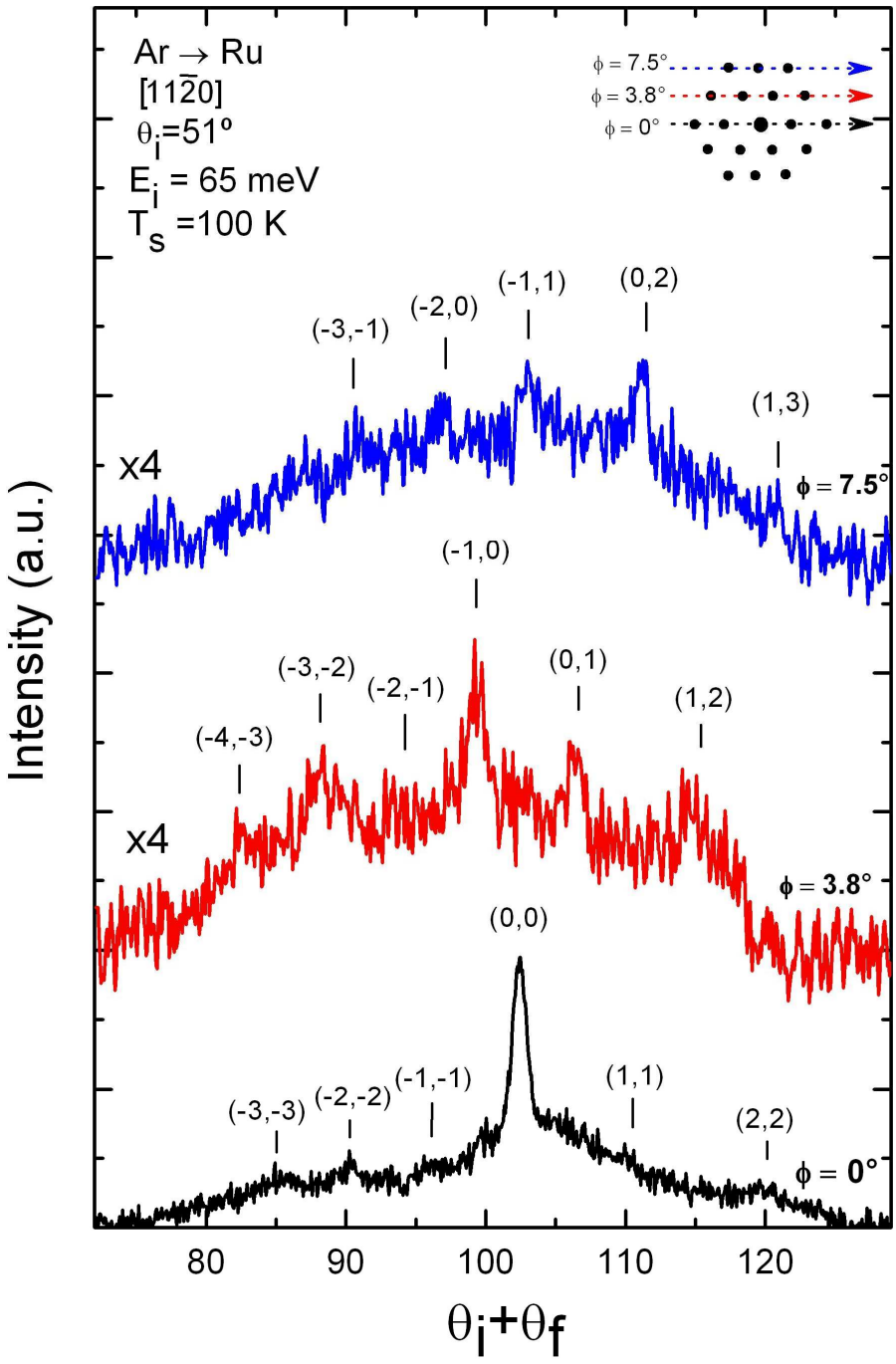

Fig.3 In-plane and out-of-plane spectra for the clean Ru(0001) surface obtained with a room temperature Ar beam.

In Fig.4 the specular intensity dependence on the surface temperature for He and Ne beams is shown. In case of He scattering a very high specular reflectivity was found, which can reach 50% by reducing the beam energy and the surface temperature. The observed increase in the slope by changing the beam from He to Ne has been fitted and is consistent with the Debye-Waller attenuation [30].

The estimated Debye temperature for Ru is ~750 K. These results support the prediction from theory of a unusual hardness of the Ru(0001) surface.

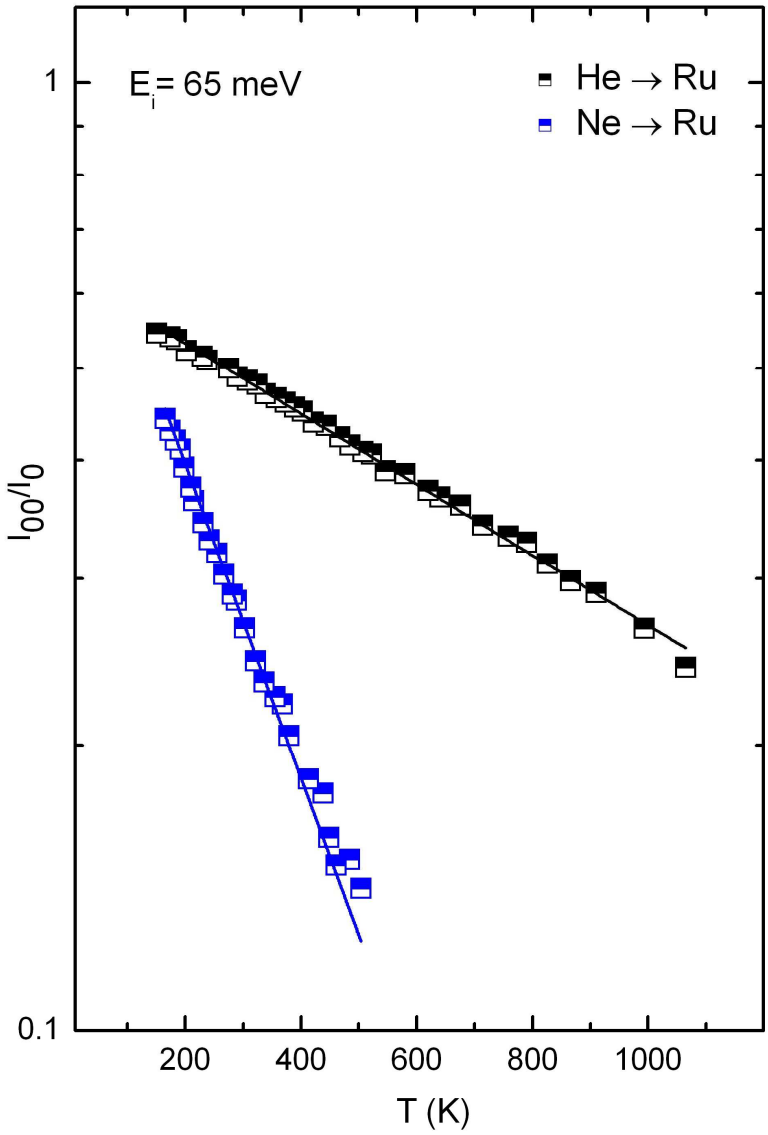

Fig.4 Dependence of the absolute specular intensity on the surface temperature for He and Ne diffraction on Ru(0001). Points have been fitted with the Debye-Waller attenuation.

A preliminary result of close-couplings calculations performed for Ne scattering is shown in Fig.5. The corrugation function was determined by fitting the measured in-plane and out-of-plane diffraction intensities by means of a trial and error procedure. The best-fit corrugation function obtained has a maximum corrugation amplitude of about 0.2 Å, compared to ~0.01 Å which is measured in case of He diffraction.

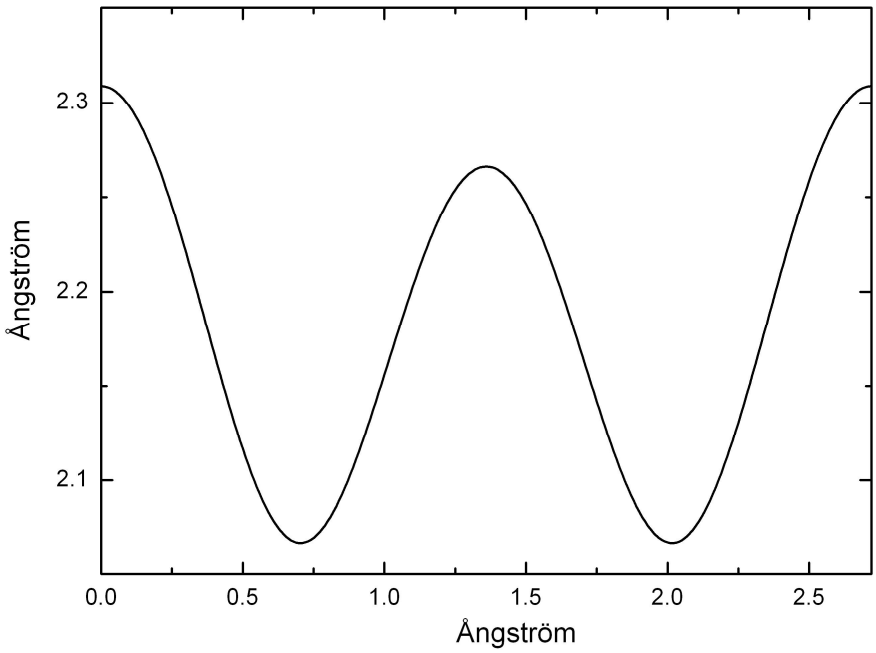

Fig.5 Best fit corrugation function for the Ru(0001) surface obtained with Ne diffraction..

This is similar to what has been already observed in the case of the NiAl (110) surface [42]. Fig.6 shows the results of such work. The authors conclude that the brightest spots in the gray scale top views of Fig.6 correspond to the Al atoms. It can be noticed that a significantly larger corrugation amplitude is seen with Ne (ζ_{Ne}=0.11 Å) compared to He (ζ_{He}=0.035 Å). A very remarkable result is that both Ni and Al atoms are visible in the Ne-derived corrugation, whereas only the topmost Al atoms appear in the corrugation determined from He-diffraction data.

Close couplings calculations for Ar diffraction from Ru(0001) have not been performed yet. They will surely provide new important information for a better understanding of high-massive atomic beam scattering.

In conclusions, the Ru(0001) surface seems to be an ideal system to investigate how different projectiles can probe different surface electron densities at different classical turning points.

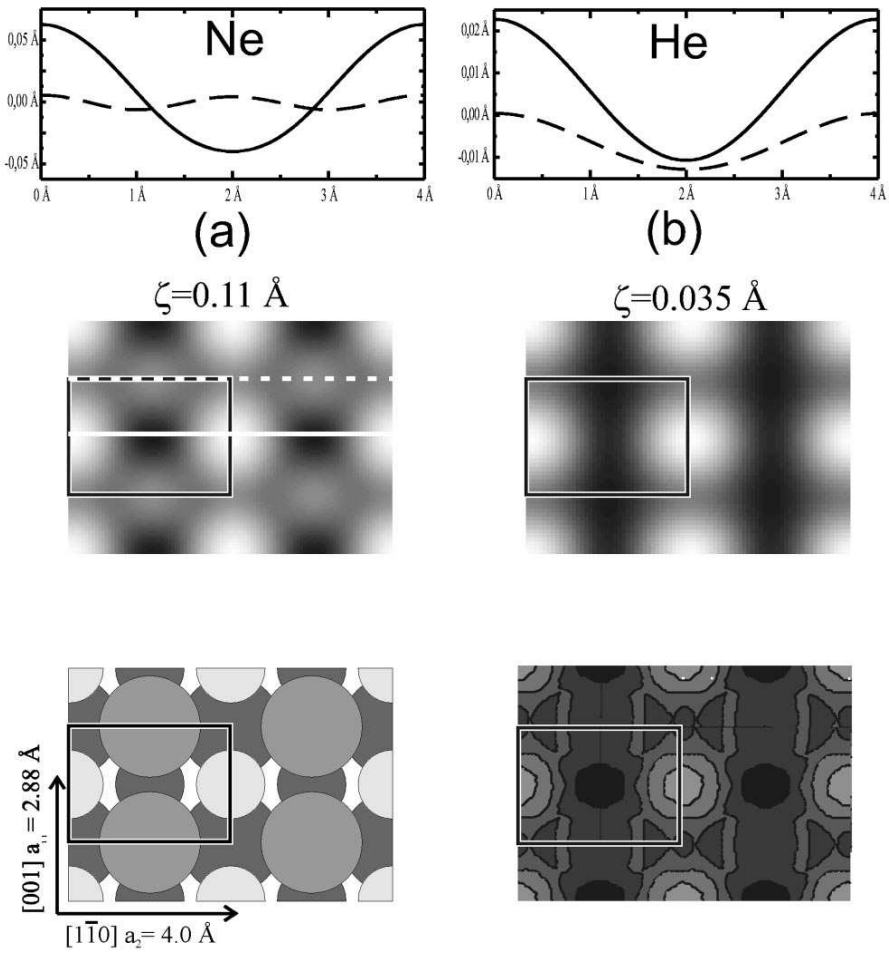

Fig.6 Gray scale representation of the best-fit corrugation functions obtained for the clean surface with Ne (a) and He (b) diffraction. Note the smaller corrugation amplitude seen with He (b) than with Ne (a). Maxima indicate the positions of the topmost Al atoms, as concluded from a comparison with a contour of constant surface electronic charge density (bottom right) determined from *ab initio* calculations.

References

[1] A.K. Geim, and K.S. Novoselov, Nature Mat. 6, 183 (2007).

[2] P.R. Wallace, Phys. Rev. 71, 622 (1947).

[3] J.W. McClure, Phys. Rev. 104, 666 (1956).

[4] J.C. Slonczewski and P.R. Weiss, Phys. Rev. 109, 272 (1958).

[5] J.A. Venables, G.D.T. Spiller, and M. Hanbucken, Nucleation and growth of thin films, Rep. Prog. Phys. 47, 399 (1984).

[6] J.W. Evans, P.A. Thiel, and M.C. Bartel, Surf. Sci. Rep. 61, 1 (2006).

[7] K.S. Novoselov et al., Science 306, 666 (2004).

[8] B. Partoens and F.M. Peeters, Phys. Rev. B 74, 075404 (2006).

[9] S. Hagstrom, H.B. Lyon, G.A. Somorjai, Phys. Rev. Lett. 15, 491 (1965).

[10] H.B. Lyon, G.A. Somorjai, J. Chem. Phys. 46, 2539 (1967).

[11] A.E. Morgan and G.A. Somorjai, Surf. Sci. 12, 405 (1968).

[12] J.W. May, Surf. Sci. 17, 267 (1969).

[13] R. Schoegl, in: G.Ertl, H. Knoezinger, F. Schueth, J. Weitkamp, Handbook of Heterogeneous Catalysis, vol.1, Weinheim (2008).

[14] J.A. Moulijn, A.E. van Diepen, and F. Kapteijn, in: G.Ertl, H. Knoezinger, F. Schueth, J. Weitkamp, Handbook of Heterogeneous Catalysis, vol.4, Weinheim (2008).

[15] I. Forbeaux, J.M. Themlin, J.M. Debever, Phys. Rev. B 58, 16396 (1998).

[16] T. Ohta, A. Bostwick, T. Seyller, K. Horn, and E. Rotenberg, Science 313, 951 (2006).

[17] C.H. Park, L.Yang, Y.W. Son, M.L. Cohen, and S.G. Louie, Nature Phys. 4, 213 (2008).

[18] S. Marchini, S. Gunther, and J. Wintterlin, Phys. Rev. B 76, 0754291 (2007).

[19] A. L. Vázquez de Parga, F. Calleja, B. Borca, M.C.G. Passeggi, J.J. Hinarejos, F. Guinea, and R. Miranda, Phys. Rev. Lett. 100, 0568071 (2008).

[20] P.W. Sutter, J.I. Flege, E.A. Sutter, Nature Mat. 7, 406 (2008).

[21] A.T. N´Diaye, S. Bleikamp, P.J. Feibelman, and T. Michely, Phys. Rev. Lett. 97, 2155011 (2006)

[22] J. Coraux, A.T. N'Diaye, C. Buss, and T. Michely, NanoLett 8, 565 (2008).

[23] T. Fujita et al., Surface Interface Anal. 37, 20 (2005).

[24] A.B. Preobajenski, M.L. Ng, A.S. Vinogradov, and N. Matersson, Phys. Rev. B 78, 0734011 (2008).

[25] B. Wang, M.L. Bocquet, S. Marchini, S. Günther, J. Wintterlin, Phys. Chem. Chem. Phys. 10, 3530 (2008).
[26] D. Jang, M.H. Du, S. Dai, J. Chem. Phys. 130, 0747051 (2009).
[27] D. Martoccia, P.R. Willmott, T. Brugger, M. Björck, S. Günther, C.M. Schlepütz, A. Cervellino, S.A. Pauli, B.D. Patterson, S. Marchini, J. Wintterlin, W. Moritz, T. Greber, Phys. Rev. Lett. 101, 1261021 (2009).
[28] P. Sutter, M.S. Hybertsen, J.T. Sadowski, E. Sutter, Nanoletters DOI: 10.1021/nl901040v. (2009).
[29] T. Livneh, M. Ascher, J. Phys. Chem. B104, 3355 (2000).
[30] D. Farias and K.H. Rieder, Atomic beam diffraction from solid surfaces, Rep. Prog. Phys. 61, 1575 (1998).
[31] D.E. Monolopoulos, R.E. Wyatt and D.C. Clary, J. Chem. Soc. Faraday Trans. 86, 1641 (1990)
[32] D.E. Monolopoulos and R.E. Wyatt, Chem. Phys. Lett. 152, 23 (1988).
[33] G. Wolken, J. Chem. Phys. 58, 3047 (1973).
[34] G. Wolken, J. Chem. Phys. 59, 1159 (1973).
[35] G. Boato, P. Cantini, and R. Tatarek, Phys. Rev. Lett. 40, 887 (1978).
[36] B. Holst, W. Allison, Nature 390, 244 (1997).
[37] M. Koch, S. Rehbein, G. Schmahl, T. Reisinger, G. Bracco, W. E. Ernst and B. Holst, Journal of Microscopy 229, 1 (2008).
[38] R.B.Doak, R.E. Grisenti, S. Rehbein, G. Schmahl, J.P. Toennies and Ch. Woell, Phys. Rev. Lett. 83, 4229 (1999).
[39] D. Barredo, F. Calleja, P. Nieto, J.J. Hinarejos, G. Laurent, A.L. Vázquez de Parga, D. Farías and R. Miranda, Adv. Mat. 9999, 1 (2008).
[40] W.W. Hayes and J.R. Manson, Phys. Rev. B 75, 113408 (2007).
[41] B. Berenbak, S. Zbiray, B. Riedmuller, D.C. Papageorgopoulos, S. Stolte, and A.W. Kleyn, Phys. Chem. Chem. Phys. 4, 68 (2002).
[42] D. Farias, M. Patting, and K.H. Rieder, J. Chem. Phys. 117, 1797 (2002).

Conclusions

The work of this Ph.D. thesis has been developed along three research lines: (1) a study on carbon nanotubes, (2) the ripple and nanodot pattern formation on Ge(100) surfaces and (3) the graphene grown on Ru(0001). The most significant results can be summarized as follows.

Nitrogen doping into single walled carbon nanotubes (SWNT) via 300 eV N_2^+ ion implantation has been studied with X-ray photoelectron spectroscopy. The nitrogen doping concentration was investigated in the range of 1.5-11.3 at.% and post irradiation annealing up to 1000°C. It was found that nitrogen atoms can be substitutionally inserted into the perfect sp^2 hexagonal network, or bind to two sp^2 carbon neighbours in a pyridine like configuration, or be connected to three or four sp^3 carbon atoms in a reconstructed double vacancy site. Also the substitutional doping is the most stable bonding against high temperature annealing.

The angular dependence of wavelength coarsening in ion sputtering induced ripple patterns on Ge (100) surfaces has been investigated in the range from 61° to 68°. For slight changes in the incidence angle, drastic changes in the coarsening behaviour of the ripple pattern were observed. By increasing the incidence angle, a transition from marginal coarsening to significant coarsening can be identified at about 65°. The results have been qualitatively discussed in the frame of the recently proposed hydrodynamic model for ion sputtering induced pattern formation.

Graphene epitaxially grown on Ru(0001) displays a remarkably ordered pattern of hills and valleys in Scanning Tunnelling Microscopy (STM) images. To which extent the observed “ripples” are structural or electronic in origin has been much disputed recently. Helium atom diffraction data analysis shows that the structural corrugation is substantially smaller (0.15 Å) than theoretically predicted (1.5 Å). The electronic corrugation, on the contrary, is strong enough to invert the contrast between hills and valleys when increasing the bias voltage in STM measurements. The large electronic corrugation results in a nanostructured periodic landscape of electron and holes pockets.

List of Publications

1. P. Barone, A. Bonanno, M. Commisso, **M. Minniti**, A. Oliva, P. Riccardi
"*Auger Electron Emission in the Interaction of Slow Na^+ Ions with Al Surfaces*"
Radiation Physics & Chemistry **76**, 499 (2007) - conference contribution

2. M. Commisso, **M. Minniti**, A. Sindona, A. Bonanno, A. Oliva, R.A. Baragiola, P. Riccardi
"*The Role of Atomic Collisions in Kinetic Electron Emission from Al surfaces by Slow Ions*"
Nuclear Instruments & Methods in Physics Research B **256**, 474 (2007) - conference contribution

3. M. Commisso, A. Bonanno, **M. Minniti**, P. Barone, P. Riccardi, A. Oliva, L. Papagno, F. Xu
"*Characterization of Carbon Nanotubes Exposed to Na or Bombarded with Na^+ at Room Temperature*"
Surface Science **601**, 2832 (2007) - conference contribution

4. F.Xu, **M. Minniti**, C. Giallombardo, A. Cupolillo, P. Barone, A. Oliva, L. Papagno
"*Nitrogen Ion Implantation in Single Wall Carbon Nanotubes*"
Surface Science **601**, 2819 (2007) - conference contribution

5. **M. Minniti**, M. Commisso, A. Sindona, P. Barone, A. Bonanno, A. Oliva, P. Riccardi
"*The Role of Al-Auger Electrons in Kinetic Electron Emission from Al Surfaces by Slow Ne^+ and Na^+ Ions "*
Nuclear Instruments & Methods in Physics Research B **257**, 618 (2007) - conference contribution

6. **M. Minniti**, M. Commisso, A. Sindona, A. Bonanno, A. Oliva, P. Riccardi
"*Electron Emission in the Interaction of 300 eV Na^+ Ions with Al Surfaces*"
Nuclear Instruments & Methods in Physics Research B **258**, 96 (2007) - conference contribution

7. **M. Minniti**, M.Commisso, A.Sindona, E.Sicilia, A.Bonanno, P.Barone, R.A.Baragiola, P.Riccardi
"*Kinetic Electron Emission from Al Surfaces by Slow Ions*"
Physical Review B **75**, 045424 (2007)

8. F. Xu, **M. Minniti**, P. Barone, A. Sindona, A. Bonanno, A. Oliva
"*Nitrogen Doping of Single Walled Carbon Nanotubes by Low Energy N_2^+ Ion Implantation*"
Carbon **46**, 1489 (2008)

9. **M. Minniti**, S. Facsko, A. Keller, W. Moeller
"*Angular Dependence of Ripple Coarsening on Ge Surfaces*"
Europhysics Letter – submitted

10. B. Borca, S. Barja, M. Garnica, **M. Minniti**, A. Politano, J.M. Rodriguez, J. J. Hinarejos, D.Farías, A.L.Vázquez de Parga, R. Miranda
"Electronic and geometric corrugation of periodically rippled, self-nanostructured graphene epitaxially grown on Ru(0001)"
Phys. Rev. Lett.- submitted